ENERGY SYSTEM MODELING TOWARDS A SUSTAINABLE FUTURE

A Dissertation

Submitted to the Faculty

of

Purdue University

by

Yiru Li

In Partial Fulfillment of the

Requirements for the Degree

of

Doctor of Philosophy

May 2020

Purdue University

West Lafayette, Indiana

THE PURDUE UNIVERSITY GRADUATE SCHOOL
STATEMENT OF DISSERTATION APPROVAL

Dr. Rakesh Agrawal, Chair

Charles D. Davidson School of Chemical Engineering

Dr. Mohit Tawarmalani

Krannert School of Management

Dr. Gintaras V. Reklaitis

Charles D. Davidson School of Chemical Engineering

Dr. Joseph F. Pekny

Charles D. Davidson School of Chemical Engineering

Approved by:

Dr. John A. Morgan

Head of the School Graduate Program

To my late and beloved grandfather, Yantian Liu

ACKNOWLEDGMENTS

First and foremost, I would like to express my deep gratitude to Prof. Rakesh Agrawal for his guidance, support and encouragement throughout my graduate journey. Always working extremely harder than I can ever imagine, never being satisfied with gains in the past, constantly feeling excitement from sparkling ideas, Prof. Agrawal has inspired, and will always inspire me on both academics and lives. His expertise in every specific field he involved, his broad knowledge in every area he could explore, together with his extraordinary creativity to combine them, truly opened up my mind on how much we can contribute to this world as chemical engineers. I truly appreciate all the discussions we had about my research over various topics, and I hope I got his philosophy of seeing the big picture and asking the right questions. I am also very honored to work with him on papers, posters, patents, presentations and reports, during which I learnt how to communicate with others professionally. All these will be my lifelong treasure and I will keep them to my future career.

I would also like to thank my committee, Prof. Mohit Tawarmalani, Prof. Gintaras Reklaitis and Prof. Joseph Pekny for their constructive insights and valuable input through the course of my PhD program. From the group meetings with Prof. Tawarmalani, I could always learn how to correctly structure a problem and how to think critically. I have benefited a lot from the comments and encouragement from Prof. Reklaitis and Prof. Pekny during my qualifier and prelim examinations.

I would like to thank Prof. Jeffrey Siirola for his guidance on process synthesis. I also thank Prof. Jeff Miller and Prof. Fabio Ribeiro for their input from the catalysis perspective on my research. In addition, I really enjoyed my teaching assistant experience with Prof. Zoltan Nagy and Prof. Jeff Greeley, through which I got great training in teaching others while getting new insights for my undergraduate knowledge.

Besides these professors, I would like to thank Melissa LaGuire for always caring for my needs and being patient, helpful and approachable. I could not complete my PhD study without her support. I would also like to thank the staff in the department, Bev Johnson, Corwin Green, Jill Clauson, Jason Davenport, Robin Waling, Cristina Farmus and Jenni Mamph for their continuous support through my graduate study.

My thesis was made possible by financial support as part of the Center for Direct Catalytic Conversion of Biomass to Biofuels, an Energy Frontier Research Center funded by the U.S. Department of Energy, Office of Science, Basic Energy Sciences, under award DE-SC SC0000997 and the Center for Innovative and Strategic Transformation of Alkane Resources (CISTAR), an Engineering Research Center funded by Nation Science Foundation, under award EEC-1647722.

My great colleagues are among the most important people during my PhD journey. I would like to thank Dr. Emre Gençer for helping me set up all my research and providing me support even after he graduated. My specialist thanks are for Dr. Taufik Ridha, for not only being my colleague whom I had the most research discussion with, but also being my closest friend who has shared my tears in all my tough times. To my CISTAR group members, Zewei Chen, Peter Oladipopu and Edwin Andres Rodriguez Gil, thank you for all your input. Without you I could not achieve anything in this project. To other past and current group members, Dr. Gautham Madenoor Ramapriya, Dr. Zheyu Jiang, Radhakrishna Tumbalam Gooty, Tony Mathew, and Jose Adrian Chavez Velasco, I enjoyed all the discussion and conversation we had, research or non-research. I also want to thank Dr. Caleb Miskin, Ryan Ellis, Allison Perna and Betsy Grubbs for our great collaboration in getting our paper published in a high-impact journal I had never dreamed of. In addition, I would like to thank other solar group members, Dr. Xin Zhao, Dr. Xianyi Hu, David Rokke, Swapnil Deshmukh, Kyle Weideman and Essam AlRuqobah, for all the great times we had. I would also like to give my special thanks to Qining Chen from UT Austin for being my best collaborator outside Purdue and an important friend.

Now I would like to thank my great friends who treated me so well and gave me unlimited love and encouragement: Dr. Lihui Wang, Dr. Xiaohui Liu, Dr. Yanran Cui, Dr. Yelin Ni, Dr. Zhe Li, Dr. Enzheng Shi, Dr. Xianyi Hu, Dr. Taufik Ridha, Yu-Hsuan Lee, Johnny ZhuChen, Zewei Chen, Yinan Xu, Ying Tan, Dr. Tongyang Shi, Dr. Xinye Zhang, Dr. Jie Gao and Ruijie Han. I would express my special thanks to my friends in the PSE community: Dr. Xiaonan Wang, Dr. Chuan Zhang, Dr. Yixin Ye, Wentao Tang and Yuhe Tian. Every time we have a reunion at a conference, I gained great happiness from you. I also appreciate the friendship from college and high school times that helped me though this PhD journey and I would like to thank Yirong Qi, Minhe Wang, Bo Shan and Mo Li by saying that.

I would like to thank my best friend, Liwei Cao, for always being with me, despite the long distance between Purdue and Cambridge. I cannot expect a better soulmate for my entire life and I cannot finish my PhD study without her being aside. I would like to thank Hao Sun for his love and support. He has held my hands through all ups and downs these years. Whatever difficulties I encountered, whenever I was stressed out or fought with myself, I knew he was always there and he always will.

Last but not least, I would like to thank my family for always encouraging me and supporting me. I thank my parents Chengyi Li and Jie Liu for guiding me towards the dream of being a chemical engineer. They gave me whatever they could, always listen to me, and always support my decision. I would like to thank my grandmother, Hengjing Fu, for her care and love. Lastly, I would like to thank my late grandpa, Yantian Liu, with my deepest grief. As a prestigious professor with high academic achievements, he always encouraged me to pursue my dream. The last time I visited him, he taught me the lesson that research should be targeted at the need of the society. My thesis is dedicated to him.

The COVID-19 gave me an unforgettable graduation season, and I will remember these dark days during this pandemic.

TABLE OF CONTENTS

Page

LIST OF TABLES xii

LIST OF FIGURES xiv

ABSTRACT xviii

1 INTRODUCTION 1

1.1 Motivation 1

1.2 Potential Strategic Role of Shale Gas towards a Sustainable Future . . 3

1.3 Multi-level Synergies in a Renewable Economy 4

1.3.1 Synergy at resource level 5

1.3.2 Synergy at building block level 5

1.3.3 Synergy at process level 6

1.4 Methodology: Systematic Energy Demand and Land Requirement Analysis 6

1.4.1 Systematic energy demand analysis 7

1.4.2 Systematic land requirement analysis 8

1.5 Methodology: Process Synthesis, Integration and Intensification 9

1.6 Thesis Overview 11

1.6.1 Process synthesis and intensification for upgrading natural gas liquids in shale gas 11

1.6.2 Systematic land requirement analysis for a solar economy 12

1.6.3 Sustainable co-production of food and solar power to relax land-use constraints 12

1.6.4 Efficient hydrogen production from solar thermal energy via high temperature water electrolysis 13

1.6.5 Co-production of solar thermal power and hydrogen 14

1.6.6 Conclusions and outlook 14

Page

2 PROCESS SYNTHESIS AND INTENSIFICATION FOR UPGRADING NATURAL GAS LIQUIDS IN SHALE GAS 15
2.1 Introduction 15
2.2 Process Synthesis and Intensification Overview 18
2.2.1 Process synthesis and intensification principles 18
2.2.2 Conventional shale gas processing (CSP) 18
2.2.3 Innovative process configurations 20
2.3 Example Processes Description 24
2.3.1 NGL co-processing (NCP) design 25
2.3.2 Integrated NGL recovery and activation (IRA) design 26
2.3.3 Switched NGL recovery and activation (SRA) design 27
2.3.4 Eliminated NGL recovery (ENR) design 29
2.4 Process Modeling 32
2.4.1 Assumptions and modeling details 32
2.4.2 Performance metrics 36
2.5 Results and Discussion 38
2.5.1 Benefits and limits of each process 39
2.5.2 Process intensification 43
2.6 Conclusion 44
3 SYSTEMATIC LAND REQUIREMENT ANALYSIS FOR A SOLAR ECONOMY 45
3.1 Introduction 45
3.2 Energy Demand in a Solar Economy 47
3.2.1 Method for predicting power demand 47
3.2.2 Intermittency of solar energy and storage efficiency 53
3.3 Land Requirement Analysis 54
3.3.1 Power recovered from current PV parks 54
3.3.2 Major land uses in the US 55
3.4 Case Study for the Contiguous US 56

Page

3.4.1 The contiguous US as a whole . . . 56
3.4.2 Land analysis at state level . . . 57
3.4.3 Case studies for other selected countries . . . 58
3.5 Conclusion . . . 60
4 SUSTAINABLE CO-PRODUCTION OF FOOD AND SOLAR POWER TO RELAX LAND USE CONSTRAINTS . . . 62
4.1 Introduction . . . 62
4.2 PV Systems for PV Aglectric Farms . . . 63
4.2.1 PV systems with current PV materials and technologies . . . 65
4.2.2 New PV materials and module designs . . . 66
4.2.3 Impact of depriving plant of infrared radiation . . . 66
4.3 Feasibility of PV Systems Based on Shadow Modelling . . . 67
4.4 Power Output of PV Aglectric Farms . . . 71
4.5 Land Requirement for PV Aglectric Farms . . . 73
4.6 Aglectric Farms with Wind Energy . . . 76
4.6.1 Power output from aglectric farms installed with wind turbines . 76
4.6.2 Availability of wind energy . . . 77
4.6.3 Necessity of developing PV aglectric farms . . . 78
4.7 Exploring Synergy between Wind and PV Aglectric Farms . . . 79
4.8 Aglectric Vision . . . 80
5 EFFICIENT HYDROGEN PRODUCTION FROM SOLAR THERMAL ENERGY VIA HIGH TEMPERATURE WATER ELECTROLYSIS . . . 82
5.1 Introduction . . . 82
5.2 High Temperature Electrolysis and Solid Oxide Electrolysis Cell . . . 84
5.2.1 SOEC basics . . . 84
5.2.2 Thermodynamics of high temperature water electrolysis . . . 85
5.2.3 Benefits of high temperature electrolysis . . . 86
5.3 Literature Review of Process Design, Modeling and Integration for Hydrogen Production Processes by High Temperature Electrolysis . . . 87

Page

5.4 Modeling Approach . . . 89
5.4.1 Overall process modeling approach . . . 89
5.4.2 Modeling for the SOEC module . . . 91
5.4.3 Performance metrics . . . 94
5.5 Process Description, Integration and Modeling Results . . . 95
5.5.1 Solar water power cycle . . . 95
5.5.2 Hydrogen production process . . . 96
5.6 Conclusions . . . 101
6 CO-PRODUCTION OF SOLAR THERMAL POWER AND HYDROGEN 103
6.1 Introduction . . . 103
6.2 Hydricity Concept and Processes . . . 104
6.2.1 Hydricity concept . . . 104
6.2.2 Hydricity processes . . . 104
6.3 Performance Metrics . . . 106
6.4 Hydricity Process with Hydrogen Produced by High Temperature Electrolysis . . . 106
6.5 Two-step thermochemical water splitting cycles for hydrogen production 107
6.5.1 Volatile stoichiometric chemistries . . . 109
6.5.2 Nonvolatile stoichiometric chemistries . . . 110
6.6 Modeling Approach . . . 111
6.7 Process Description, Modeling results and Discussion . . . 112
6.8 Conclusion . . . 114
7 CONCLUSIONS AND OUTLOOK . . . 117
7.1 Overview . . . 117
7.2 Process Intensification for Shale Gas Processing . . . 118
7.3 Synergistic Use of Land for Renewable Energy Harvesting and Food Production . . . 118
7.4 Integration of Solar Powered Hydrogen and Electricity Production . . . 119
7.5 Synergy and Process Intensification . . . 119

Page

7.5.1 Identification of synergy at multiple levels 119
7.5.2 Aspects of process intensification 120
7.6 Future Research Directions 120
REFERENCES 122
A SHADOW DEPTH AND POWER OUTPUT FOR VARIOUS LOCATIONS 134
B SHADOW SIMULATION 136
C POWER OUTPUT OF VERTICAL BIFACIAL PV AGLECTRIC FARMS 138
C.1 East-west Facing Vertical Bifacial PV Aglectric Farms 138
C.2 North-South Facing Vertical Bifacial PV Aglectric Farms 139
D SHALE GAS PROCESSES MODELING DATA 142
E MODELING APPROACH DETAILS FOR THE HYDROGEN PRODUCTION PROCESS VIA HIGH TEMPERATURE ELECTROLYSIS 155
VITA 159

LIST OF TABLES

Table		Page
2.1	Key performance results for various flowsheets modeled by Model I	38
2.2	Key performance results for various flowsheets modeled by Model II	39
3.1	Results summary for multiple land requirement analysis cases	59
4.1	Shadow depth and usable land for various PV aglectric configurations	69
4.2	Simulated and corrected power output for cases in Table 4.1	72
4.3	Summary of PV system characteristics and estimated PV aglectric farm power output	74
5.1	Electrochemical reactions within an SOEC for water splitting	85
5.2	System conditions and simulation results for the integrated H_2 production (Figure 5.7) and solar water power generation process	98
5.3	System conditions and simulation results for the integrated H_2 production (Figure 5.8 to 5.10) and solar water power generation processes	101
6.1	Parameters of the base case of hydricity with ZnO/Zn water splitting cycle	114
6.2	Summary of modeling results for a 100 MW constant power supply from hydricity process with Zn/ZnO cycle	115
A.1	Shadow depth and power output for Fresno, CA	134
A.2	Shadow depth and power output for South Plains region, Texas	135
A.3	Shadow depth and power output for West Lafayette, IN	135
C.1	Irradiance data for four locations representative of a variety of meteorological conditions [155]	138
C.2	Parameters used in modeling the power output of N-S facing vertical bifacial farms	140
C.3	Modeled power output for vertical bifacial PV aglectric farms	141
D.1	Stream information for process NCP-1 simulated by Model I	143
D.2	Stream information for process NCP-1 simulated by Model II	144
D.3	Stream information for process IRA-1 simulated by Model I	145

Table Page

D.4 Stream information for process IRA-1 simulated by Model II 146

D.5 Stream information for process SRA-2 simulated by Model I 147

D.6 Stream information for process SRA-2 simulated by Model II 148

D.7 Stream information for process ENR-1 simulated by Model I 149

D.8 Stream information for process ENR-1 simulated by Model II 150

D.9 Stream information for process ENR-2 simulated by Model I 151

D.10 Stream information for process ENR-2 simulated by Model II 152

D.11 Stream information for process ENR-3 simulated by Model I 153

D.12 Stream information for process ENR-3 simulated by Model II 154

LIST OF FIGURES

Figure Page

1.1 Vision of a renewable economy [7] 4

1.2 Flowchart for a systematic methodology of predicting energy demand in a renewable economy 7

1.3 Methodology for process synthesis, integration and intensification 10

2.1 Conventional shale gas processing (CSP), which follows the four-section design hierarchy 16

2.2 NGL co-processing (NCP) design, where the NGL fractionation section is eliminated and all NGL components are co-processes together 20

2.3 Integrated NGL recovery and activation (IRA) design, where the NGL recovery and activation section are integrated by recycling the unreacted components from the NGL activation section to the NGL recovery section 21

2.4 Switched NGL recovery and activation (SRA) design, where the order of the NGL recovery and the NGL activation section are switched 22

2.5 Eliminated NGL recovery (ENR) design, where there is no cryogenic distillation for the separation of methane and NGLs 24

2.6 An example of the NGL co-processing (NCP) design, referred as NCP-1 . . 25

2.7 An example of the integrated NGL recovery and activation (IRA) design, referred as IRA-1 27

2.8 An example of the switched NGL recovery and activation (SRA) design, referred as SRA-1, where the NGL recovery section is placed after the dehydrogenation reactor 28

2.9 An example of the switched NGL recovery and activation (SRA) design, referred as SRA-2, where the NGL recovery section is placed after the entire NGL activation section 28

2.10 An example of the Eliminated NGL recovery (ENR) design, referred as ENR-1, which is the simplest process 30

2.11 An example of the Eliminated NGL recovery (ENR) design, referred as ENR-2, where part of the liquid hydrocarbon stream is used as absorbent to absorb unreacted light hydrocarbons, especially ethane 30

Figure Page

2.12 An example of the Eliminated NGL recovery (ENR) design, referred as ENR-3, where absorption is employed and the process is operated at high pressure 31

2.13 (a) Turboexpander demethanizer for the NGL recovery section; (b) Well-mix binary membrane system for the hydrogen separation unit in NGL activation section 33

3.1 Detailed calculation model for a fossil fuel to solar energy transition. Diamonds indicate the splitting of energy use and ovals indicate efficiencies for the corresponding steps. 47

3.2 Solar parks' average power per unit land area versus the local insolation . 55

3.3 Power density requirement of each state when 50% of its miscellaneous land and 5% (a) and 15% of urban land (b) is used for PV installation . . 58

4.1 PV systems for co-production of food and energy with farmland. Fixed south-facing patterned panels (a), tracking patterned panels (b) and bificial vertical panels (c) can be used with existing PV materials, while short-pass tracking (d), short-pass non-tracking (e), long-pass tracking (f) and long-pass non-tracking (g) would have optimum performance with band-gap materials tailored to the incident spectrum. 64

4.2 Spatially mapped shadow depth for cases A, D and E from Table 4.1. Case A, representing an elevated south-facing fixed latitude-tilt PV park, shows regions of high shadow depth. Case D shows the advantage of using an east–west tracking system. Case E shows the advantages gained from implementing a chequered pattern on the panels. 70

4.3 Percentages of agricultural land required to meet states' energy needs. Cases shown are for a PV power output of 7 W/m^2 on regular PV parks (the current average PV park output) and 3.7 W/m^2 over agricultural land (a), and for a PV power output of 11 W/m^2 on regular PV parks (the upper end of current PV park output) and 5.5 W/m^2 over agricultural land (b). . 75

4.4 U.S. Average Annual Wind Speed at 80 Meters, from Ref. [103] 77

5.1 Schematic of an SOEC for water splitting 84

5.2 ΔH, ΔG and $T\Delta S$ of water splitting reaction versus temperature 86

5.3 Schematic for the integrated Aspen Plus and Matlab process design framework. All the models implemented in Aspen Plus and Matlab are communicated via a Matlab core script. 90

5.4 General modeling method framework for the hydrogen production via high temperature electrolysis powered by solar thermal electricity 91

Figure Page

5.5 Flowsheet model for the SOEC module in Aspen Plus 92

5.6 The solar water power cycle with one inter-stage reheating. The vapor coming out of the high pressure turbine (indicated by the orange line) is sent back to the solar heater for reheating before entering the medium pressure turbine [137]. HPT: high pressure turbine; MPT: medium pressure turbine; CT: condensing turbine. 95

5.7 Hydrogen production process via SOEC (thermoneutral mode). Before entering the SOEC, the water is pumped to high pressure and heated by solar thermal energy. T1: high pressure turbine; T2: medium pressure turbine; C1: H_2 compressor; C2: air compressor. 96

5.8 Hydrogen production process via SOEC. The gas coming out of the cathode is reheated for power generation. T1: high pressure turbine; T2 and T3: medium pressure turbines; C1: H_2 compressor; C2: air compressor. . . 99

5.9 Hydrogen production process via double SOEC modules. The fist SOEC is operated at higher pressure and the second SOEC is operated at low pressure. T1: high pressure turbine; T2 and T3: medium pressure turbines; C1: H_2 compressor; C2: air compressor. 99

5.10 Hydrogen production process via SOEC. The water collected from the water-hydrogen separator is reheated for power production. T1: high pressure turbine; T2 and T3: medium pressure turbines; T4: condensing turbine; C1: H_2 compressor; C2: air compressor. 100

6.1 Schematic for the concept of hydricity system based on solar thermal energy [20] 105

6.2 Hydrogen production by a two-step water splitting thermochemical cycle [20] 107

6.3 Hydrogen production by Zn/ZnO thermochemical cycle 109

6.4 Modeling approach for a hydricity process where H_2 is produced by thermochemical cycle 112

6.5 Hydricity system with hydrogen produced by ZnO/Zn water splitting cycle 113

C.1 Input parameters for modeling of power output of E-W facing vertical bifiacial PV aglectric farms using the Purdue University Bifacial Module Calculator (PUB) [90] 139

E.1 Details of the H_2 production process model, including all the input and output information 155

E.2 Details of the model for the SOEC module, including all the input and output information 156

E.3 Details of the model for the solar water power cycle, including all the input and output information 157

ABSTRACT

Li, Yiru Ph.D., Purdue University, May 2020. Energy System Modeling towards a Sustainable Future. Major Professor: Rakesh Agrawal.

As the global population approaches 10 billion by the mid-century, supplying all the needs of the human race from the Earth's limited land area and resources with minimized greenhouse gas emission will be the essential challenge of sustainability. In a sustainable economy, all renewable energy, in combination with carbon sources and other elements from the nature, such as water, air and land, will be used synergistically to produce building blocks for human beings. These building blocks, including electricity, heat, fuels, hydrogen, etc., will enable the production of all the end uses for human beings. The challenge for chemical engineers is to come up with processes and synergistic strategies to enable such a sustainable future.

Shale gas can serve as both energy resource and chemical feedstock for the transition period towards a sustainable economy, and has the potential to be a carbon source for the long term. Natural gas liquids contained in shale gas provide abundant feedstock for chemical and fuel production and could bring extra value for remote shale gas basins. Unlike current shale gas processing where large scales are preferred, simple and intensified processes with least processing steps and least pieces of equipment are favored for remote shale plays. While conventional shale gas processing usually follows a four-section hierarchy of "gas treatment - NGL recovery - NGL fractionation - NGL activation", four innovative configurations are proposed for simpler and intensified process design, including NGL co-processing, integrated NGL recovery and activation, switched NGL recovery and activation, and eliminated NGL recovery. A two-step conversion of NGLs to liquid hydrocarbons via dehydrogenation followed by oligomerization is used as an example to show how these innovative process de-

signs evolve. Simulation results show that the loss of ethane, the NGL component with the highest concentration, could be largely reduced by the innovative process configurations. At the same time, higher yield of liquid products, fewer processing steps, reduced pieces of equipment and elimination of energy and capital-intensive units can be achieved. The intensification of process here would benefit the modularization of shale gas plants, and make it possible for distributed production of liquid hydrocarbons onsite for remote shale locations.

While shale gas being the carbon source for a sustainable future, renewable energy, especially solar and wind energy, will become the dominant energy resources for a sustainable economy. However, both solar and wind energy are dilute resources and harvesting them requires vast tracts of land, which could potentially compete with agricultural production for food. As a bookend case study, we investigate the land requirement for a 100% solar economy. The contiguous United States is used as an example and our analysis takes into account several issues that are usually ignored, such as the intermittent solar availability, estimation of future energy demand, actual power production from solar farms and available land types. Results show that it will be difficult for currently available land to meet the energy needs using current solar park designs for the entire contiguous United States and for nearly half of the individual states, which include well over half of the total US population. Barring radical improvements in agricultural output that could greatly reduce the land devoted to agriculture, the competition for land between energy and food seems inevitable, posing a major challenge to a future solar economy. If we extend the study to Germany, the United Kingdom and China, we could see that the challenge exists for both developed and developing countries.

To resolve the issue, a concept of "Aglectric" farming is proposed, where agricultural land produces electricity without diminishing existing agricultural output. Both wind turbines and photovoltaic (PV) panels can be used to generate electricity on agricultural land. While the use of the current PV panels is known to have a negative impact on crop growth, we propose several innovative PV systems using existing and

new materials, innovative installation paradigms and module designs. Through extensive modeling of PV shadows throughout a day, we show that some of our designed PV systems could mitigate the loss of solar radiation while still maintaining substantial power output. Thus, it should be possible to design and install these PV systems on agricultural land to have significant power output without potentially diminishing agricultural production. We also show that PV aglectric farms alone will have the potential of realizing a 100% solar economy without land constraint. Together with regular PV parks and wind aglectric farms, PV aglectric farms will serve as an important option for a renewable future.

With its high energy density and zero greenhouse gas emission, hydrogen is the key energy carrier in a sustainable future. We introduce a process design strategy for the production of hydrogen by high temperature water electrolysis using concentrated solar thermal energy. At the same time, co-production of hydrogen and electricity is investigated where hydrogen can be produced by both thermochemical cycles and high temperature electrolysis. The process design features the process integration between hydrogen production and power generation. Process simulation is performed in an integrated Matlab and Aspen Plus platform. Efficiencies are analyzed for various processes.

Synergy is the key feature of all the studies in the dissertation. Process intensification for shale gas conversion and process integration for solar hydrogen production are examples of synergy at the process level. Coproduction of hydrogen and electricity and coproduction of electricity and food are examples of synergy at the building block level. Potential synergistic use of solar, wind and shale resources is an example of synergy at the resource level. Synergy is the keyword of the sustainable future we are pursuing.

1. INTRODUCTION

To enable a sustainable future that can support the large population on the earth, chemical engineers need to contribute by providing systematic analysis of energy and resource usage, creating innovative processes for chemical and fuel production, and looking for efficient energy storage methods.

1.1 Motivation

The world population is expected to reach 8.5 billion by 2030 and even over 10 billion by the end of this century [1]. Together with the rapid growth in population, every aspect of human needs, including residential and commercial needs, power production, industrial production and transportation, exerts much stress on our global energy resources. The global energy demand will have a 20% growth from 2017 to 2040 [2], which indicates the immense energy supply pressure we human beings are facing.

Nowadays, even with the fast progress in renewable energy application, the world energy consumption still largely depends on fossil fuels. In 2018, oil, natural gas and coal constitute ∼85% of total energy consumption of the world [3]. However, at current production rate, both natural gas and oil reserves are only sufficient for about 50 years [3]. Furthermore, the greenhouse gases (GHG) emission caused by excessive use of fossil fuels has brought about global environmental concerns towards pollution and climate change.

In the light of all these factor, the grand challenge before us is to insure human beings' living quality by meeting all the energy needs from limited resources on the earth. Obviously, renewable energy will replace fossil fuels to become the major primary energy resources [4]. However, there is still a long way to go. In 2018, the

renewable energy share in both the US' and the world's primary energy consumption portfolio is about 4% [3]. Obstacles exist for widespread implementations of renewable energy [5]:

- Land restriction. Renewable energy often has much lower power density, or rate of supplied energy per unit land area, than fossil fuels [6]. It indicates that large tracts of land must be dedicated to renewable energy harnessing, which might result in land competition with agricultural production.

- Intermittent availability. Renewable resources such as solar and wind energy are not available at a steady rate round the clock; instead, the accessibility of these energy resources are subject to season, weather, time, etc., which results in difficulty in transmission and demand of large-scale energy storage.

- Uneven distribution. Similar to fossil fuels, the distribution of renewable energy resources is uneven across the world and varies from location to location. However, different from fossil fuels, long-distance transportation of renewable energy resources and the transmission of secondary energy generated from renewable energy (electricity) are both difficult.

- Carbon resources are still needed. As a energy resource, fossil fuels can be replaced by renewable energy. However, production of commodity chemicals and some fuels, such as aviation kerosene, still requires resources containing carbon. Sustainable biomass could be a solution, but the total availability and associated land usage remain issues of concern.

Therefore, to realize a sustainable future, systematic analysis is imperative to identify the challenges. To resolve the identified challenges, efficient processes for power, fuel and chemical production are needed. Process system engineering methodology is the key of synthesizing, designing, modeling and optimizing such processes [7].

1.2 Potential Strategic Role of Shale Gas towards a Sustainable Future

Apart from the challenges discussed in section 1.1, the transition towards a renewable energy powered future is likely to be gradual because of the technology barriers and extensive infrastructure and policy changes [8]. During this transition period, fossil fuels will still share significant percentages in the world's energy consumption portfolio. It is imperative that fossil resources be properly and efficiently utilized both as energy resources and chemical feedstocks. Among all the available fossil resources, natural gas has the potential to play a strategic role in both the transition period and the renewable future.

Firstly, natural gas, together with the related combined-cycle technology, is seen as a more efficient alternative to coal for electric power generation [9]. Meanwhile, the carbon footprint is lower, which could mitigate the GHG emission [10]. Therefore, natural gas could serve as a relatively "cleaner" energy resource.

Secondly, recent development of shale gas has brought natural gas condensates to the fuel and chemical feedstock market [11]. In addition, methane as the major component in natural gas, can also be an important chemical feedstock through various conversion technologies such as steam methane reforming [9].

Therefore, triggered by the shale gas boom in the recent decade, natural gas, especially shale gas has the potential to be a strategic resource:

- During the transition period from a fossil fuel powered era to a renewable future, natural gas can be the energy resource, or the "bridge fuel", considering its high energy conversion efficiency and low carbon footprint [12].

- In a sustainable future, if available, methane and natural gas condensates can serve as feedstocks for the production commodity chemicals and fuels that are difficult to be replaced by renewable resources.

1.3 Multi-level Synergies in a Renewable Economy

In a sustainable future where all the need of the human race will be supplied from the earth's limited resources, all the available resources must be used synergistically [7]. Figure 1.1 shows a viable pathway towards a renewable economy. In such a vision, renewable energy resources, such as solar and wind energy, together with other elements of nature such as soil, CO_2, air, and water will be able to provide most of the human needs that are currently provided through the use of fossil resources. For energy uses, renewable energy can be first harnessed as electricity, heat and hydrogen that can then be directly for end-uses or used for creating other products. As carbon resources, sustainable biomass which ultimately comes from solar energy and shale gas can complement each other to mitigate possible environmental footprint or land restriction. With these energy and carbon sources available as building blocks, every aspect of human needs can be satisfied, including fertilizer production for food growth, chemical/fuel production for everyday and industrial uses, transportation powered by either fuels or electricity, as well as water, electricity and heat demands [5].

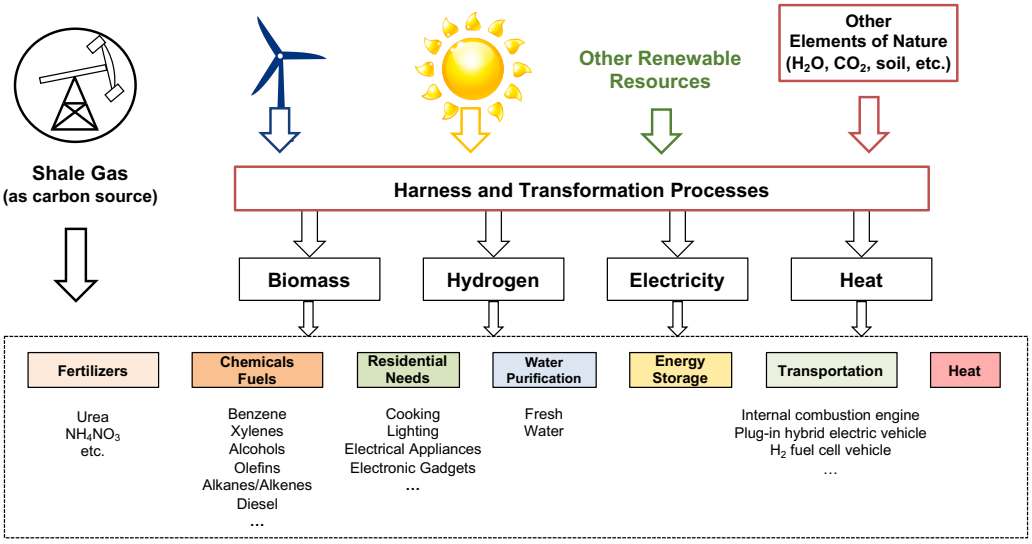

Fig. 1.1. Vision of a renewable economy [7]

Considering all the challenges discussed in Section 1.1, efficient employment of all the resources require highly synergistic systems. In Figure 1.1, there are three levels of synergy that worth our attention.

1.3.1 Synergy at resource level

Among all the renewable resources, solar energy is the most promising because of its abundance and vast accessibility in most of the populated regions in the world [13]. Wind energy is one of the most fastest growing energy resources today [14]. Sustainable biomass is a promising carbon resource for chemical and fuel production [15]. The recent shale gas boom has brought opportunities for converting shale gas components to liquid products [16].

With all these energy and carbon resources available, usage of multiple resources needs to be synchronized. For energy resources, solar, wind and other renewable energy resources show drastically different availability around the world depending on locations, seasons, times, weathers, etc. If properly synchronized, the utilization of these renewable energy resources can complement one another to reduce the energy storage demand and grid instability resulted from their intermittent availability [17]. For carbon resources, sustainable biomass growth requires large land area dedicated [18] and shale gas exploitation will cause GHG emission [19]. Integrated utilization of sustainable biomass and shale gas can relax the land constraint and mitigate the GHG emission. In addition, carbon resource exploitation is also connected to energy resource availability; likely competition in land might exist between biomass cultivation and renewable energy harvesting.

1.3.2 Synergy at building block level

Water, food, carbon sources, hydrogen, electricity and heat are building blocks to meet daily human needs [20]. These demand driven building blocks are inherently interconnected [4]. Examples are: power production could be accompanied by heat;

hydrogen production requires electricity and/or heat; sustainable biomass is a co-product of agricultural cultivation aiming at food. And more importantly, all these building blocks are often needed simultaneously for end-use production. Therefore, looking for synergy at the building block level will help identify the most efficient method for resource utilization.

1.3.3 Synergy at process level

Because of the synergy of building blocks discussed in the previous section, the processes for various end-use production all share common elements, such as equipment and mass/energy streams. In existing research, these processes are often studied alone. If these common elements can be identified at early design stage, the synergistic process design and integration would help maximize the inherent complementary aspects of energy conversion [20]. Meanwhile, for a single process, it is crucial to find internal synergy within the process, which will potentially lead to more efficient, more intensified or simpler processes.

1.4 Methodology: Systematic Energy Demand and Land Requirement Analysis

In order to construct a roadmap towards a sustainable future as a chemical engineer, two fundamental questions need to be answered:

- How much energy is needed in a sustainable future?
- Is currently available land sufficient to supply the energy needed?

Systematic energy demand and land requirement analysis is imperative to answered these questions.

1.4.1 Systematic energy demand analysis

To predict the primary energy demand in a sustainable future dominantly powered by renewable energy, factors taken into consideration include energy harvesting, generation, transmission, conversion and storage [21]. A systematic method that counting all these factors is shown in Figure 1.2. Primary energy consumption data

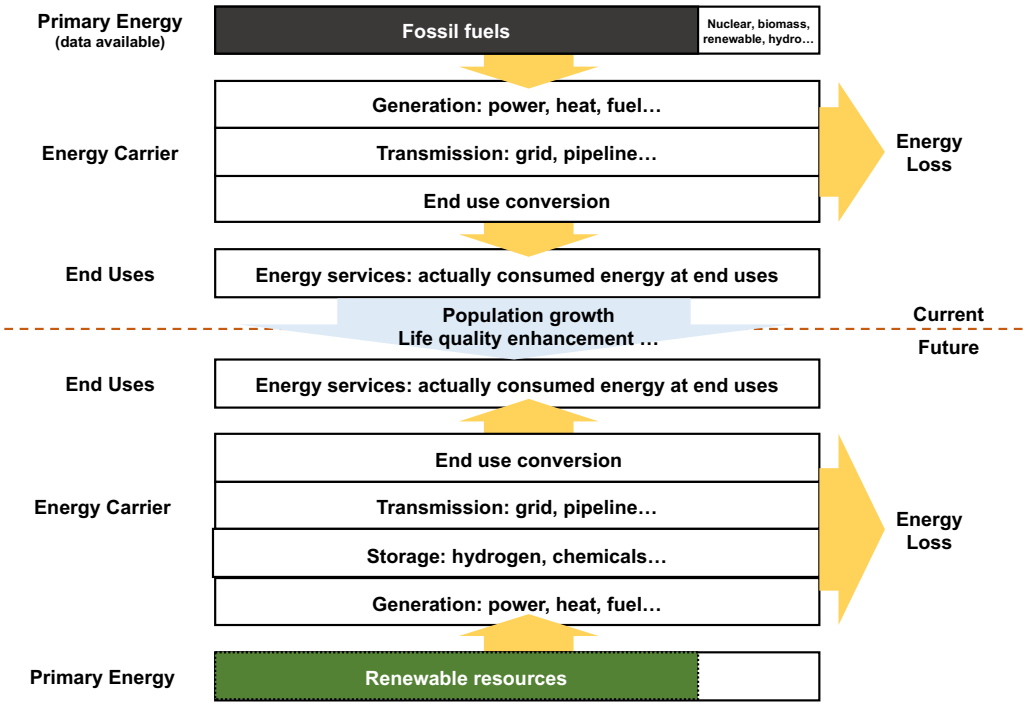

Fig. 1.2. Flowchart for a systematic methodology of predicting energy demand in a renewable economy

can be acquired from multiple sources, such as the US Energy Information Administration (EIA) [22], the International Energy Agency (IEA) [23], and many company reports. Currently, since fossil fuels still dominants the primary energy consumption share, there are three major steps from primary energy to end uses:

- Generation of secondary energy, or conversion to energy carriers. This include power generation, heat production, fuel production, etc.

- Energy transmission. This include electricity transmission through grid, pipeline transportation for fuels, etc.

- End use conversion. It is the final step of energy conversion that produces the energy actually consumed at end uses. For example, the inner combustion engine provides the power for vehicles; electronic supplies consumes electricity for their operation.

Though these steps can be interconnected and not all energy flows through every step, it provides the basic flowchart for us to track the energy flow via each step. If we know the efficiency of each step, we can calculate the energy loss of every step as well as the energy flowing into the next step. By this method, we could know how much energy is actually consumed by the end uses.

To predict the energy demand in the future, the basis for the prediction is the demand from the end uses. Because of population growth, economic advances and increased living quality of human beings, the end use demand will drastically increase [2]. From the predicted end use demand, we can back-calculate the primary energy requirement in the future. However, since renewable energy will be the major primary energy, energy storage efficiency should be taken into consideration due to its intermittent availability. Meanwhile, due to the changed means of energy generation, transmission and utilization, the efficiency of each step will be different from that in current times. Correctly identifying the efficiencies and energy flow is the key to systematically estimate the energy demand in a sustainable future [21].

1.4.2 Systematic land requirement analysis

Since renewable energy is usually quite dilute with power density several orders of magnitude lower than fossil fuels [6], correctly calculate the land requirement is crucial for determining the synergy needed for a sustainable economy. Two aspects must be correctly identified for a systematic land requirement analysis.

First, true power density must be used. Power density is defined as the rate of energy supply per unit land area. On one hand, given the intermittent availability of most renewable energy resources, the rate of energy supply (or power generation) should not be defined only based on the period when the energy is available. Instead, the rate of energy supply should be calculated as the energy available average through 24-hour. On the other hand, the land area needed for energy harvesting and conversion should be carefully defined. Taking wind energy for example, the land area a wind plant needed is classified into two categories: direct impact area and total area [24]. Similar circumstance applied to solar energy. For the overall land requirement analysis, total land area should be used to calculate the power density; while when looking for possible synergy between energy harvesting and other activities such as agricultural production, direct impact area is important. In summary, to calculate the power density of renewable energy resources, total area needed for energy harvesting must be used with averaging through 24-hour.

Second, available land area that could be used for energy harvesting must be correctly identified. Land uses are categorized into six types: cropland, grassland pasture and range, forest-use land, special use area, urban use area and other or miscellaneous land [25]. For example, currently available land for solar photovoltaic (PV) installation only includes urban land and miscellaneous land; for wind plants, cropland and grassland are also available. Furthermore, the percentage of each land type's availability must be taken into account. Only when we correctly identify the land area that is available can we have a reasonable estimation on if the currently available land is sufficient for each region or country.

1.5 Methodology: Process Synthesis, Integration and Intensification

Although processes targeted for fossil fuels and renewable energy can be quit different in desired products and energy supply methods, they share the same basic philosophy in process synthesis, design, integration and intensification. The similarity

lies in the common units inevitable in processes, such as reactors, heat exchangers, pumps, and turbines. What is more, the synergy at process level, as discussed in section 1.3.3, could help enhance the performance of processes for either fossil fuels or renewable energy.

The methodology in process synthesis, integration and intensification is summarized in Figure 1.3 [20]. The method starts with the determination of process synthesis

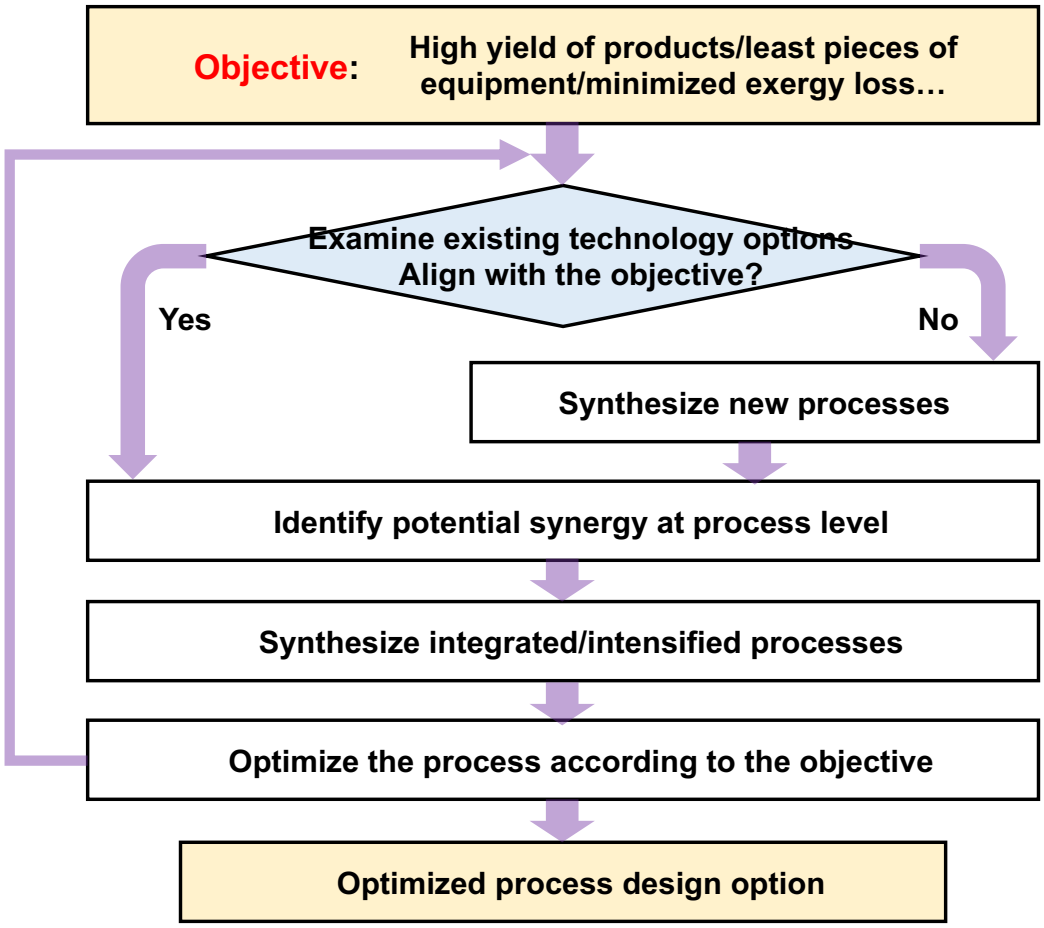

Fig. 1.3. Methodology for process synthesis, integration and intensification

objective. The objective can be versatile: if targeting at efficient utilization of feedstocks, the objective could be high yield of products; if targeting at simple process amendable to process modularization and distributed manufacturing, the objective can be least pieces of equipment; the objective can also be minimized exergy loss,

high thermal efficiency, etc. After the objective is determined, existing technology options should be examined to check if existing processes align with the objective. If not, new processes need to be synthesized. Here, process synthesis could follow the heuristic design, take new methods such as switching the order of unit operations in conventional processes, or use computer-aided methods. Then the existing processes or newly synthesized processes should be analysed to identify potential synergy with the processes. The synergy could lie in multiple units within a single process across multiple processes. The observed synergy is the start point of process integration or intensification. The next step is to further optimize the integrated/intensified process or screen the integrated/intensified processes with regard to the determined objective. The acquired optimized process should be re-examined and finally put into the database as a process option.

1.6 Thesis Overview

This thesis first focuses on the shale gas, as a bridge energy resource towards a sustainable future and a potential carbon source for all the time. Innovative process synthesis and intensification for converting shale gas to liquid products are discussed. Then we look at the overall energy supply and land availability of a renewable economy and a promising solution is proposed for possible land constraint. The last part of the thesis discusses the electricity and hydrogen co-production processes in a solar economy.

1.6.1 Process synthesis and intensification for upgrading natural gas liquids in shale gas

Upgrading the natural gas liquids (NGLs) contained in shale gas can bring extra value for remote shale gas basins. Current shale gas processing usually separates each individual alkane component and delivers them for further processing. Moreover, existing processes in industrial practice and research all strictly follow a four-section

hierarchy including gas treatment, NGL recovery, NGL fractionation and NGL activation. At remote shale plays lack in transportation infrastructure, it is important to have intensified processes to produce value-added products from shale gas on site. In Chapter 2, we propose innovative processes by using a design strategy where possible synergistic interaction within sections is investigated and the four-section design hierarchy is abandoned. Meanwhile, process intensification is employed to simplify the process and make it amendable for process modularization. This chapter works with the synergy at process level.

1.6.2 Systematic land requirement analysis for a solar economy

Solar energy, though promising as the energy source for a fossil fuel-deprived future, is a dilute resource and harvesting it requires vast tracts of land. In Chapter 3, we demonstrate the methodology discussed in section 1.4 in a case study where the land requirement is analysed in each of the 48 contiguous states of the United States for a 100% solar powered economy to address the likely land competition. In addition, cases for the United Kingdom, Germany and China are also studied. UK and Germany are used as representatives for densely populated developed countries while China represents developing countries. In this chapter, we prefer local photons for local use for consideration of minimizing transmission loss and energy security. Under this preferred scenario, our land requirement analysis shows that land is constrained for a 100% solar economy and that the land competition for energy and food will be intense. Thus, in a solar economy, land use intensification will be required to avoid conflict between our competing land use needs.

1.6.3 Sustainable co-production of food and solar power to relax land-use constraints

Renewable energy could often be land constrained by the diffuse nature of renewable resources. To relax land constraints, Chapter 4 proposes the concept of

'aglectric' farming, where agricultural land will be sustainably shared for food and energy co-production. While wind turbines on agricultural land are already put into practice, solar power production on agricultural land is still under research. Here, we propose photovoltaic systems that are suitable for installation on agricultural land. Adjusting the intensity, spectral distribution and duration of shading allows innovative photovoltaic systems to achieve significant power generation without potentially diminishing agricultural output. The feasibility of solar aglectric farms has been proven through shadow modelling. The proposed solar aglectric farms—used alone or in combination with regular solar parks or wind plants—could be a solution for a sustainable renewable economy that supports the 'full Earth' of over 10 billion people. This chapter works with the synergy at resource level.

1.6.4 Efficient hydrogen production from solar thermal energy via high temperature water electrolysis

With its high energy density and zero greenhouse gas emission, hydrogen is the key energy carrier in a sustainable future. Hydrogen production from solar energy has been studied by many researchers by either thermochemical or electrolysis method. Chapter 5 introduces a process design strategy for the production of hydrogen by high temperature water electrolysis using concentrated solar thermal energy. High temperature water electrolysis is realized by using solid oxide electrolysis cell (SOEC). SOEC requires both electricity and heat input to enable the energy balance of the water splitting process. We utilize solar thermal power production cycle to supply the electricity the SOEC requires. Meanwhile, water is heated by concentrated solar energy to reach the SOEC operation temperature before electrolysis. The power generating and hydrogen production processes are integrated, allowing electricity flow and heat transfer between the two cycles. Process simulations for the proposed integration are performed in an integrated Matlab and Aspen Plus platform. Considering the electricity and power input as well as the overpotential of the SOEC, different

operation modes of SOEC, including thermoneutral, endothermic and exothermic operations, could largely affect the efficiency of hydrogen production. Therefore, different operation modes of SOEC are investigated and various process designs are examined accordingly to figure out the most efficient process under various circumstances. In this way the most promising solar thermal hydrogen production process could be designed and flexibility of operation conditions could also be identified. This chapter involves synergy at both building block and process level.

1.6.5 Co-production of solar thermal power and hydrogen

The concept of "hydricity" is proposed by Gençer et al, which involves the coproduction of hydrogen and electricity from solar thermal energy and their judicious use to enable a sustainable economy [5]. However, the system has not screened all the potential hydrogen production technologies to reach the optimum within the technology limitations. In previous work, hydrogen production in hydricity adopts two methods: direct thermal water splitting and two-step thermochemical cycle based on FeO/Fe_3O_4. However, with advanced research on solar hydrogen production, there are many possible methods such as thermochemical cycles based on other metals/metal oxides and water electrolysis yet to investigate. Chapter 6 discusses hydricity processes with hydrogen production by various thermochemical cycles and high temperature eletrolysis. The efficiencies of all the hydricity processes are analyzed and compared. This chapter involves synergy at both building block and process level.

1.6.6 Conclusions and outlook

Chapter 7 presents key findings from this dissertation along with directions and visions for future research advances.

2. PROCESS SYNTHESIS AND INTENSIFICATION FOR UPGRADING NATURAL GAS LIQUIDS IN SHALE GAS

2.1 Introduction

Triggered by the technology advances in hydraulic fracturing and horizontal drilling in recent years, shale gas has become an increasingly important source of natural gas in the United States (US). As predicted by the US government's Energy Information Administration (EIA), nearly 90% of natural gas production in the US will come from tight and shale resources by 2050 [26]. The expanding shale gas production has significantly prompted the availability of natural gas liquids (NGLs) in the US, since most of the shale gas resources in the US are reported to contain substantial NGLs [9]. NGL is a mixture of hydrocarbons constituting primarily ethane, propane, butane, and pentane. From 2013 to 2018, the NGL production in the US has increased by 68%, from 951 million barrels to 1595 million barrels [27], and another 32% increase is predicted towards 2050 [26]. Since most of NGLs are currently serving as feedstocks to the bulk chemical industry, the elevated level of NGL production has significantly impacted the entire petrochemical landscape in the US [26] [28].

Development in shale resources has brought challenges in processing shale gas produced in several major shale plays, such as Marcellus and Bakken, which are located far away from historically gas producing and processing region. Construction of pipelines to transport pipeline gas and NGLs from these regions to large existing processing plant complexes, such as the Gulf Coast, can be capital intensive. As a result, shale gas and associated NGLs at remote shale plays are often flared, which would increase the environmental burden of shale exploitation and lead to a resource loss. The issue creates an opportunity to develop small-scale, intensified onsite facil-

ities to further process NGLs for value-added products. Upgrading NGLs to liquids is one of the promising technologies to monetize stranded shale associates [29] [30].

However, these existing process intensification or modularization efforts all sticks to the conventional shale gas processing scheme; the structure of the processes have not been adapted to meet the goal of smaller scale onsite production. Therefore, innovative process synthesis is needed to better intensify the processes.

Currently, most existing research and industrial practices stick to the conventional process design hierarchy for gas processing and upgrading. By this hierarchy, shale gas processing followed by NGL upgrading employs a four-section process design of "gas treatment - NGL recovery - NGL fractionation - NGL activation" [31] [32] [33] [34], as shown in Figure 2.1. It involves rather complicated systems and requires centralized large-scale operation. At remote shale plays, the distributed nature of production sites, the shortage of transportation infrastructure and the temporal variation in shale well production impede the development of such processing facilities. Instead, NGL upgrading at remote shale plays requires process simplification and intensification.

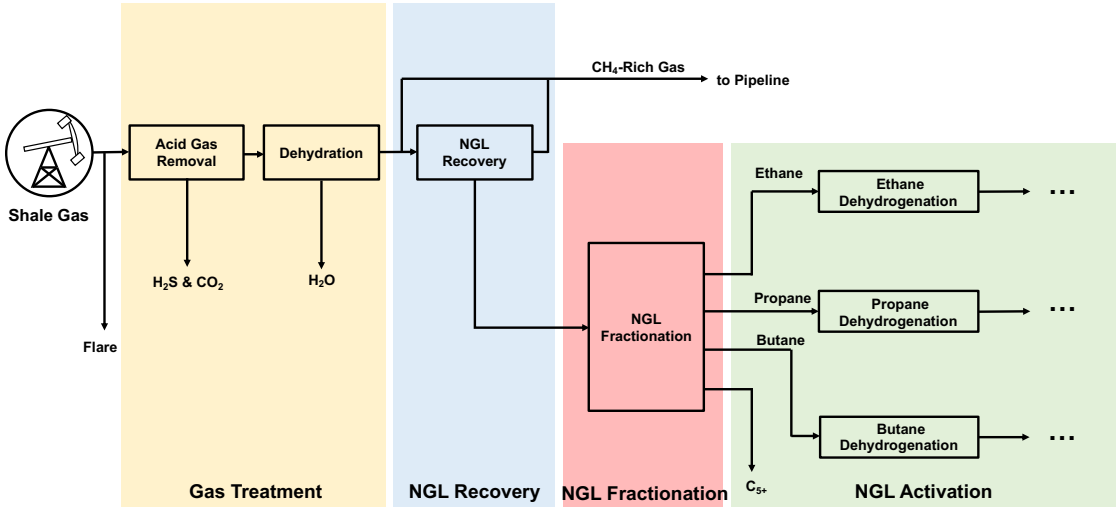

Fig. 2.1. Conventional shale gas processing (CSP), which follows the four-section design hierarchy

Only limited research or industrial advances are investigating processing intensification in shale gas processing. Gong et al proposed a systematic simulation-based process intensification method hedged against uncertain feedstock composition [35]. Yang and You compared conventional large-scale shale gas processing, large-scale methanol production from shale gas and modular methanol manufacturing with shale gas and found that modular methanol manufacturing is more economically competitive [36]. Gao and You illustrated that modular manufacturing could improve the economic performance of shale gas supply chain by formulating detailed optimization model to consider design and operational decisions [37]. However, these existing process intensification or modularization efforts all follow the conventional shale gas processing hierarchy; the structure of the processes have not been adapted to meet the goal of smaller scale onsite production. Therefore, innovative process synthesis is needed to better intensify the processes. In this chapter, we introduce four types of innovatively synthesized process configurations, which simplify and intensify the shale gas processing with the hierarchy broken. These process configurations are: NGL co-processing (NCP), integrated NGL recovery and activation (IRA), switched NGL recovery and activation (SRA) and eliminated NGL recovery (ENR). These process design strategies include co-processing multiple streams, eliminating or integrating certain aforementioned sections, shifting the order of the conventional processing steps and employing less complicated separation methods. The four configurations are not proposed independently, but one is evolved from another for higher product yield and better intensified processes. Pieces of equipment will be reduced through the process synthesis and intensification, which will ultimately make our proposed processes potentially feasible for remote shale plays. Then a process upgrading NGLs to liquid hydrocarbon products via dehydrogenation and oligomerization is used as an example to show how the process design evolves and how the aforementioned process configurations benefit the product yield and process intensification.

2.2 Process Synthesis and Intensification Overview

2.2.1 Process synthesis and intensification principles

Here we list principles that provide guidelines for our process synthesis and intensification, and for each process configuration mentioned in section 2.2.3 and each example process in section 2.3, we explain how these principles are utilized in our NGLs upgrading processes.

- Principle 1: Break the heuristic process design hierarchy wherever needed. Paradigm shift should be considered for improvement of the process.
- Principle 2: Minimize the number of unit operations. In other words, try to create process flowsheets with least number of equipment.
- Principle 3: Keep unit operations in the flowsheet simple and easy to operate. A corollary would be avoiding complex heat and mass integrations unless they are low-cost and easy to operate.

2.2.2 Conventional shale gas processing (CSP)

As mentioned in the previous section, conventional shale gas processing followed by NGL upgrading employs a four-section process design of "gas treatment - NGL recovery - NGL fractionation - NGL activation", as shown in Figure 2.1.

- Gas treatment. Raw shale gas pipelined from reservoir or wellheads first passes through acid gas removal units where the acid components in the shale gas, such as CO_2 and H_2S are removed [38]. The gas coming out of acid gas removal is sent to a dehydration unit to get rid of water vapor contained in the shale gas [39]. These two steps constitute the "gas treatment" section in the four-section design hierarchy. The purpose of gas treatment is to prevent corrosion in equipment and pipeline and potential freezing problems in downstream cryogenic units.

- NGL recovery. In this section, NGLs are separated from sweetened and dried shale gas, usually by cryogenic separation [40]. If the separated methane contains too much nitrogen that exceeds the pipeline standard, a nitrogen rejection unit is needed to acquire the sales gas that meets the specification.

- NGL fractionation. To further obtain each component in the NGL stream from the NGL recovery, a series of distillation columns sequentially separates ethane, propane, butanes and higher hydrocarbons. Each of the separated alkane component can be sent to corresponding downstream facilities for further processing.

- NGL activation. Any further conversion of the NGL components from NGL fractionation is included in this section. Ethane is almost exclusively sent to ethane crackers for ethylene production, which ultimately turns into plastics. Propane and butanes are partially served as chemical feedstocks and converted to propylene, butadiene, etc. As NGL components are usually converted to corresponding olefins before further processing, ethane/propane/butane dehydrogenation is shown in Figure 2.1 as the first step of NGL activation. Dehydrogenation can be implemented by various pathways, such as steam cracking, partial oxidation, direct catalytic conversion, etc.

The conventional shale gas processing typically treats NGLs as chemical feedstocks. However, at remote shale plays where complicated chemical production does not show economic potential, the goal of NGL processing would be adjusted to maximizing the use of shale resources and mitigating light alkane losses by flaring [41]. For example, liquid hydrocarbons that are easier to transport than NGLs, such as gasoline blends or transportation fuel, could be legitimate target products of onsite processing at remote shale plays. With the new target of NGL processing and the demand of intensified processes, we propose four new configurations [42].

2.2.3 Innovative process configurations

NGL co-processing (NCP)

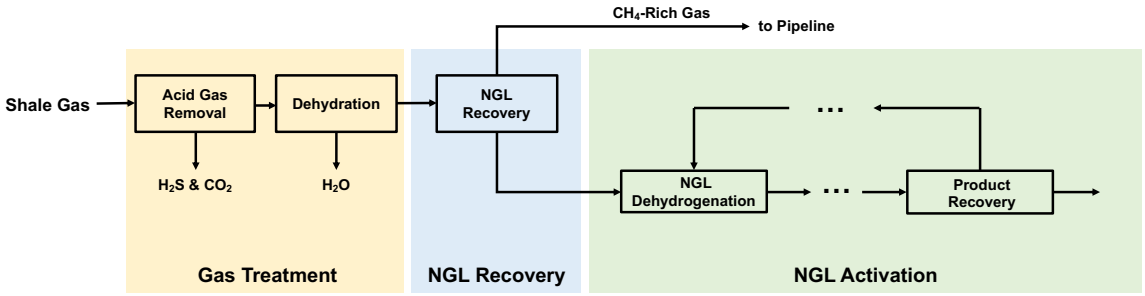

Fig. 2.2. NGL co-processing (NCP) design, where the NGL fractionation section is eliminated and all NGL components are co-processes together

Since the target products are no longer specialized chemicals from individual NGL components, ethane, propane, butane and heavier alkanes might not be necessarily separated before conversion. Therefore, the four-section CSP could be simplified, thus intensified by eliminating the NGL fraction section. By this design (NGL co-processing, referred as NCP), the recovered NGL stream is directly sent to the NGL activation section as a mixture, as shown in Figure 2.2. By this way, the NGL fractionation section is eliminated. In CSP design, an NGL fractionation train typically constitutes of three distillation columns, a deethanizer, a depropanizer and a debutanizer, and accompanied heat exchangers (condensers and reboilers) and pressure changers (valves). The elimination of the NGL fractionation section largely simplifies the process, reduces the number of pieces of equipment and saves the energy cost for the distillation columns.

As for the NGL activation section, the activation of each NGL component is integrated into one single intensified step of co-processing. The parallel reactors of ethane, propane, butanes dehydrogenation now become one dehydrogenation reactor

which processes the NGL mixture. Further conversion and processing steps for each NGL component are also integrated into one set of equipment. In this way, the complexity of the system is largely reduced, and less equipment is needed, which complying with principle 1 and 2 in section 2.2.1.

Integrated NGL recovery and activation (IRA)

In both CSP and NCP design, sections are independent of each other. Apart from getting the feed stream from the immediate upstream section and delivering the product stream to the immediate downstream section, there is no other mass interaction between sections. For example, Figure 2.2 shows a recycle stream from the product recovery back to the NGL dehydrogenation, which is within the boundary of the NGL activation section. However, if synergy between sections could be identified, integration between sections might be able to improve the process.

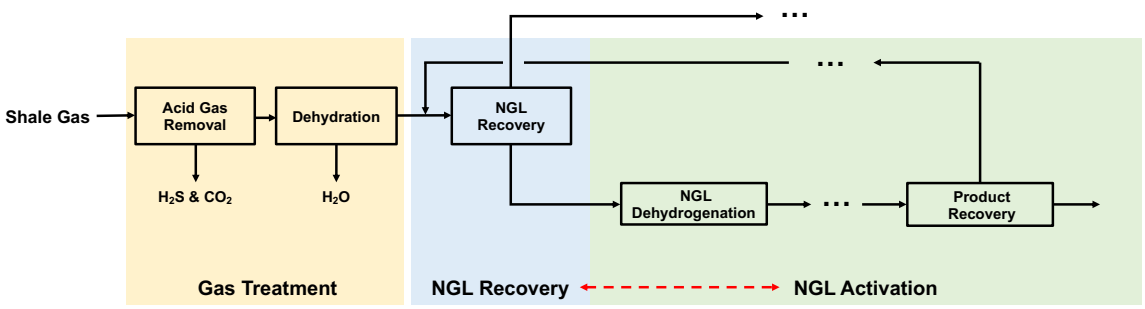

Fig. 2.3. Integrated NGL recovery and activation (IRA) design, where the NGL recovery and activation section are integrated by recycling the unreacted components from the NGL activation section to the NGL recovery section

One example of the integration is shown in Figure 2.3, which integrates the NGL recovery and activation section by recycling the unreacted components in the NGL activation section back to the NGL recovery section. By this integrated NGL recovery

and activation (IRA) design, the two sections are not independent as in the CSP or NCP design.

One of the benefits of this integration is that it could lead to process intensification by eliminating methane build-up and reducing the size of the equipment in the NGL activation section. In NCP design, considering that the NGL recovery cannot recover 100% of the methane in the shale gas, the NGL stream entering the NGL activation section contains certain amount of methane. Thus, some processing steps would be required within the NGL activation section to prevent methane build-up in the recycle loop, such as methane separation or simply taking a purge. In the IRA design, the NGL recovery section, which separates methane out, is contained in the recycle loop and the issue of methane build-up is resolved. The required methane-removing step is now integrated with the NGL recovery section. No methane separation steps are needed in the NGL activation section and potential flowrate increase due to methane accumulation is also eliminated. Therefore, the IRA design is an effective step towards process intensification.

Switched NGL recovery and activation (SRA)

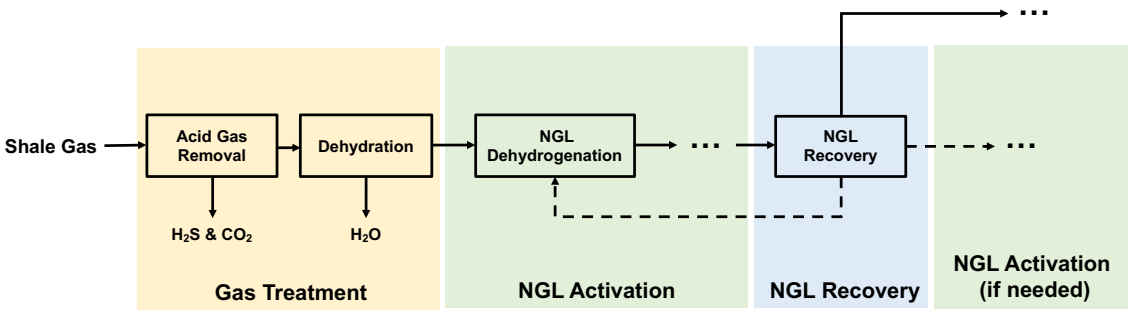

Fig. 2.4. Switched NGL recovery and activation (SRA) design, where the order of the NGL recovery and the NGL activation section are switched

Dehydrogenation reactions of NGLs are equilibrium controlled endothermic reactions with added molecules. Increasing the single-pass conversion of NGL dehydrogenation is critical to increasing the overall yield of the process and reducing the recycle. One of the possible solutions to increasing the single-pass conversion of dehydrogenation is to lower the partial pressure of the reactants by adding diluents. To maximize the utilization of the shale resources and not to add complexity or external stream to the NGL processing, we look for synergy within the process and observe that methane, as an inert at the dehydrogenation temperature, can serve as the diluent. Here we propose a design by switching the NGL recovery and activation sections (SRA) as shown in Figure 2.4. In this SRA design, sweet and dry shale gas coming out of the gas treatment section is directly sent to the NGL activation section, without passing through the NGL recovery section. After NGL components are partially or fully converted, methane is then separated in the NGL recovery section. If the NGL activation is not completed, reactors could follow the NGL recovery.

Apart from favoring the equilibrium in the dehydrogenation by adding methane as a diluent, one additional benefit is that catalytic dehydrogenation might not be needed. Instead, a thermal cracker for producing olefins could be employed. Similar to a steam cracker, methane can be used to substitute steam in the cracker and serve as a thermal mass. In this way, not only the equipment for steam generation is eliminated, catalyst regeneration is eliminated. The complexity of the process is reduced and pieces of equipment can be minimized.

Eliminated NGL recovery (ENR)

The NGL recovery section, which separates methane and NGLs usually by cryogenic distillation, requires high pressure and low temperature. The capital and energy-intensive unit could be eliminated to enable a further simplified process. Here we propose a design strategy with eliminated NGL recovery (ENR). As shown in Figure 2.5, there is only gas treatment and NGL activation section within this process. After

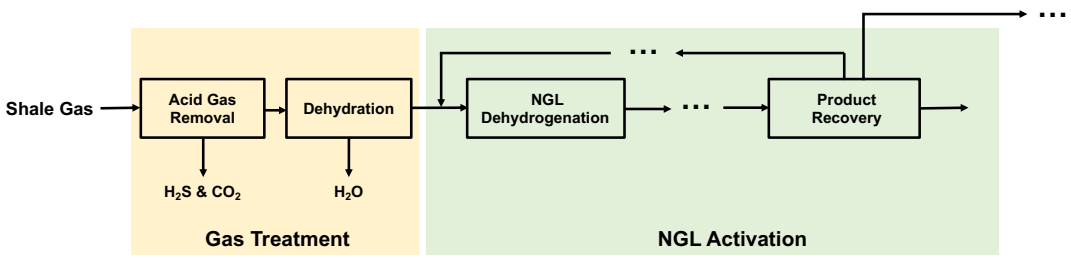

Fig. 2.5. Eliminated NGL recovery (ENR) design, where there is no cryogenic distillation for the separation of methane and NGLs

directly co-processing NGLs in the NGL activation section subsequent to gas treatment, various product recovery methods could be used to separate liquid product, unreacted NGLs and methane, including multi-stage condensation/flash, absorption, etc. By removing the complicated and energy intensive cryogenic NGL recovery, the ENR design further simplifies the process compared with IRA or SRA design.

2.3 Example Processes Description

Since gas treatment is the common section of all configurations discussed in this study, all our process described and/or modeled below will start with a treated gas with acid gases and water removed. The selection of acid gas removal and dehydration technology depends on the concentration of acid gases and water in the shale gas stream, and we assume that no acid gases or water are left within the dry and sweet gas entering subsequent sections.

In this work, we use a two-step conversion of NGL, dehydrogenation and oligomerization, as an example of NGL activation and propose conceptual process designs for each of the four configurations described in the previous section.

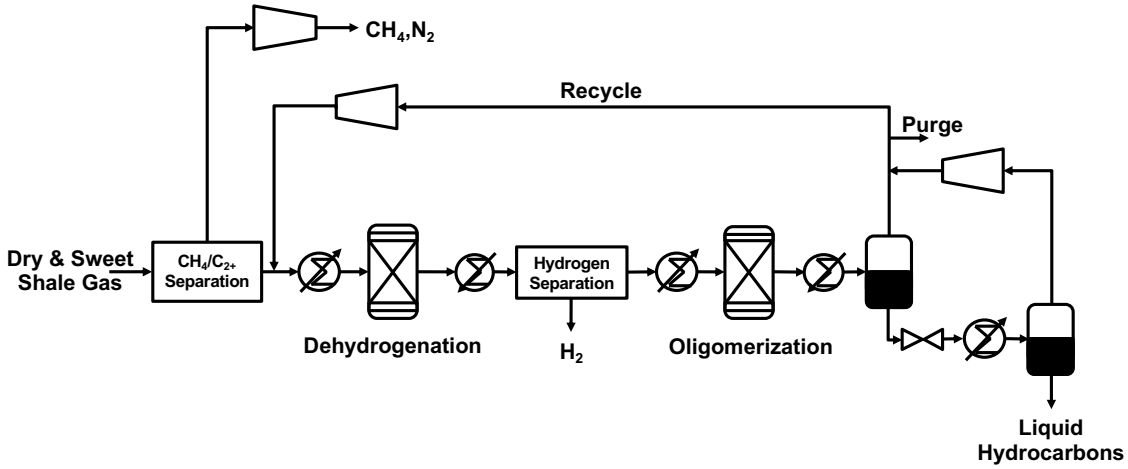

Fig. 2.6. An example of the NGL co-processing (NCP) design, referred as NCP-1

2.3.1 NGL co-processing (NCP) design

Ridha et al [43] proposed a process where NGLs can be converted to liquid products via catalytic dehydrogenation of NGLs followed by catalytic oligomerization. As shown in Figure 2.6, this process (NCP-1) can serve as an example of the NCP design where NGLs are co-processed in a single dehydrogenation reactor followed by further processing steps. In the NGL recovery section, a turboexpander is employed to provide the refrigeration of -96 °C, which is the temperature at the top of the demethanizer. The NGL recovery sections for all the processes described in this work, if there is one, employ the same demethanizer to which the refrigeration is provided by a turboexpander. The methane stream separated from the NGL recovery section can be pipelined as sales gas. Nitrogen contained in the shale gas is separated together with methane, and a further nitrogen rejection unit might be needed depending on the nitrogen concentration in the shale gas [38]. If pipeline is not available at the processing site, the methane can be used as fuel gas to supply heat for other units such as the dehydrogenation reactor.

From the NGL recovery section, the recovered NGL stream is expanded to 7 bar and then enters the NGL activation section without NGL fractionation. The NGL activation section in this work includes dehydrogenation of NGL components to olefins followed by catalytic oligomerization of olefins to liquid hydrocarbons. In the dehydrogenation reactor, ethane, propane and butane undergo dehydrogenation with or without catalyst to corresponding olefins. As dehydrogenation of ethane, which is the major component within NGL, is an endothermic reaction, the reactor must be operated at moderately high temperature (750 - 900 °C) to achieve reasonably high conversion. Hydrogen generated during dehydrogenation is then removed prior to the oligomerization reactor by a membrane, and a 15% hydrogen concentration is remained in the stream entering the oligomerization reactor to prevent catalyst coking. The olefins produced in the dehydrogenation reactor are sent to an oligomerization reactor to be catalytically converted to higher molecular weight hydrocarbons [44]. The product from the oligomerization reactor is a mixture of high molecular weight liquid hydrocarbons and unconverted light alkanes/alkenes. Due to a large difference in their boiling points, high molecular weight hydrocarbons can be recovered through a two-step condensation. The stream is cooled to 2 °C before the first condenser, and the liquid phase from the first condenser is adjusted to ambient pressure and temperature to release the dissolved light hydrocarbons. The vapor from the two condensers which contains unconverted light alkenes, is recycled to the inlet of the dehydrogenation reactor. To reduce the accumulation of methane and hydrogen in the recycle loop, a purge stream is taken.

2.3.2 Integrated NGL recovery and activation (IRA) design

An example of the IRA design (IRA-1) is shown in Figure 2.7. Compared with the NCP design, the vapor stream coming out of liquid hydrocarbon recovery units is not recycled to the dehydrogenation reactor; instead, it is recycled to the NGL recovery section to take advantage of the methane separation section. By this recycle

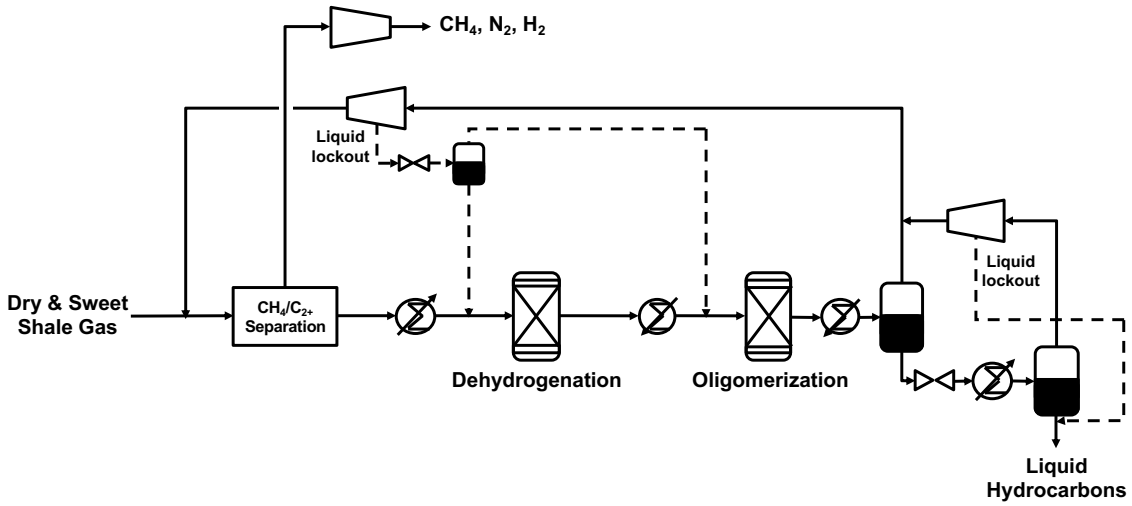

Fig. 2.7. An example of the integrated NGL recovery and activation (IRA) design, referred as IRA-1

strategy, the methane build-up issue in the NCP design is resolved and no purge stream is needed in the recycle loop. Furthermore, according to oligomerization catalyst research, there are certain zeolite catalysts that can tolerant hydrogen within oligomerization reaction. Since the demethanizer can separate hydrogen out together with methane, the hydrogen separation unit subsequent to the dehydrogenation reactor can also be eliminated without causing H2 build-up within the recycle loop.

2.3.3 Switched NGL recovery and activation (SRA) design

Two examples of SRA design are shown in Figure 2.8 and 2.9 and are label as SRA-1 and SRA-2, respectively. In SRA-1, shale gas coming out of the gas treatment section, including methane and NGLs, are delivered to the dehydrogenation reactor. Since methane is the major component in the stream, NGLs shares lower partial pressure, compared to process flowsheets of design NCP and IRA, and thus convert to olefins in a higher conversion. After the dehydrogenation, produced olefins, hydrogen and unconverted alkanes enters the NGL recovery section. Here methane and hydro-

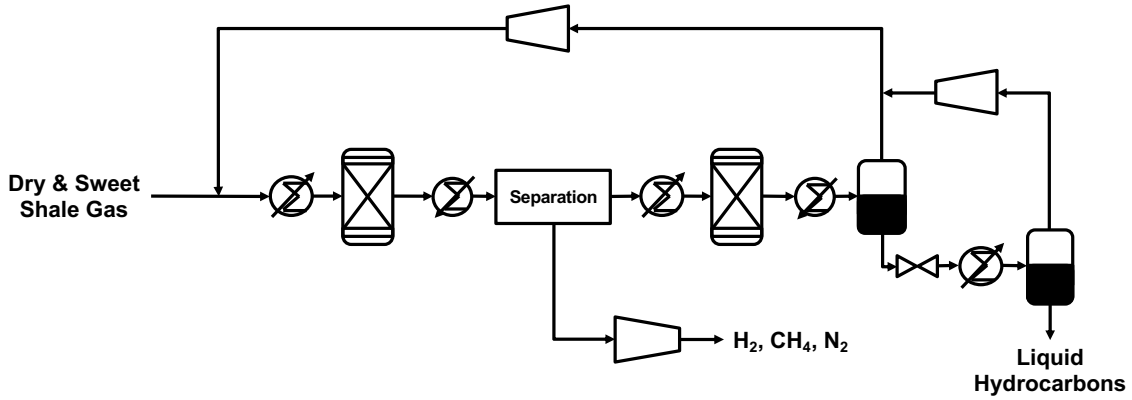

Fig. 2.8. An example of the switched NGL recovery and activation (SRA) design, referred as SRA-1, where the NGL recovery section is placed after the dehydrogenation reactor

gen are separated by a demethanizer and the remaining C_{2+}, including olefins and unreacted C_{2+} alkanes are sent to the oligomerization reactor for further conversion to liquid hydrocarbons.

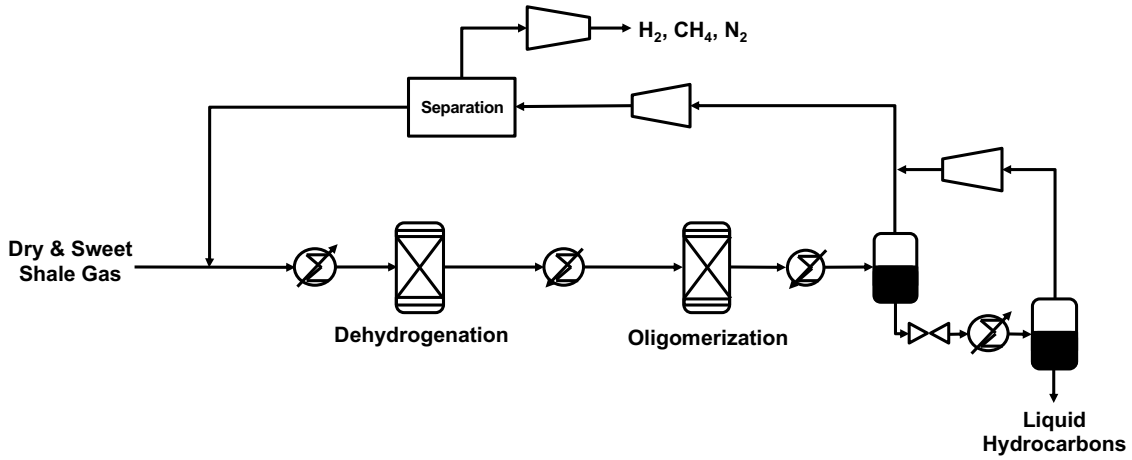

Fig. 2.9. An example of the switched NGL recovery and activation (SRA) design, referred as SRA-2, where the NGL recovery section is placed after the entire NGL activation section

However, the NGL recovery section needs to be operated at high pressure (with original compressor at 60 bar and demethanizer at 14 bar) and low temperature (−96 °C at the top of the demethanizer column), which is not preferred especially when between the two reactors. Therefore, flowsheet SRA-2, as shown in Figure 2.9 is proposed. Here, the sweet and dry shale gas acquired from the gas treatment section is directly sent to the NGL activation section and converted to higher molecular liquid hydrocarbons through dehydrogenation and oligomerization. Note that for the simplicity of the process, these is no H_2 separation after the dehydrogenation. After the liquid product is recovered by a two-step condensation, the remaining gas stream, containing unconverted light alkanes and alkenes, is sent to the NGL recovery section to separate methane and hydrogen before recycled to the dehydrogenation reactor.

2.3.4 Eliminated NGL recovery (ENR) design

As shown in Figure 2.5, there are only gas treatment and NGL activation section within this process. A simple flowsheet (ENR-1) is shown in Figure 2.10 to present the simplest process design and two improved flowsheets (ENR-2 and ENR-3) are shown in Figure 2.11 and 2.12.

In process ENR-1, similar as in flowsheet SRA-2 (Figure 2.9), sweet and dry shale gas directly enters the NGL activation section after gas treatment, and the NGL components are converted into liquid hydrocarbons via dehydrogenation and oligomerization. The product from oligomerization reactor is then sent to two condensers for liquid hydrocarbon recovery. Here, in the first condenser, the temperature is at −20 °C and at this temperature, the separated gas stream mainly contains methane, hydrogen produced from the dehydrogenation reactor, and a small part of the unconverted ethane. This gas stream can be post-processed to produce pipeline gas or used as fuel gas for heat or electricity production. The second condenser is operated at ambient pressure and temperature. The liquid phase is collected as liquid hydrocarbon products and the gas phase is recycled to the dehydrogenation reactor.

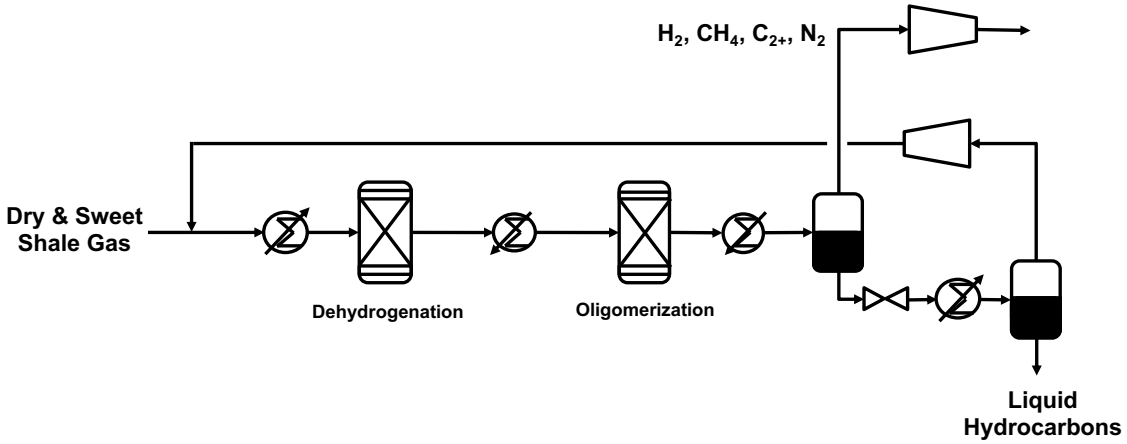

Fig. 2.10. An example of the Eliminated NGL recovery (ENR) design, referred as ENR-1, which is the simplest process

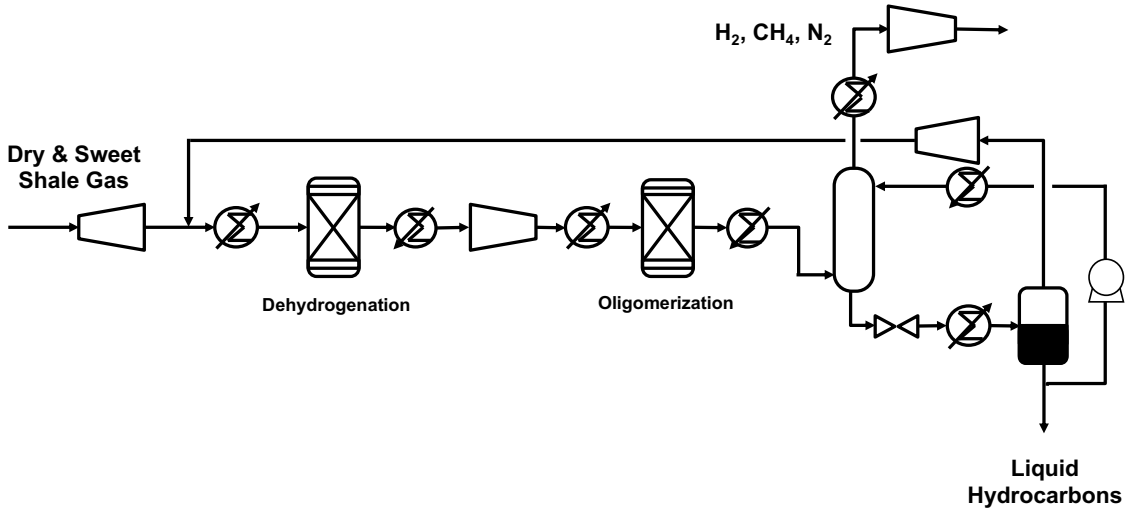

Fig. 2.11. An example of the Eliminated NGL recovery (ENR) design, referred as ENR-2, where part of the liquid hydrocarbon stream is used as absorbent to absorb unreacted light hydrocarbons, especially ethane

One of the drawbacks of this process is that significant amount of ethane is lost at the first-stage condenser. In processes shown ENR-2 and ENR-3, absorption is

used improve the separation and reduce the loss of ethane. A part of the recovered liquid hydrocarbon is used as absorbent to absorb C_{2+} components in the products coming out of the oligomerization reactor. The remaining gas phase only contains methane and hydrogen produced from dehydrogenation. It is then directed for further processing to get hydrogen and sales gas or used as fuel gas for heat and electricity. The liquid, including the liquid hydrocarbon products and absorbed light alkanes and olefins, is expanded and heated to ambient temperature before the subsequent condenser. Liquid products are collected, and unreacted light hydrocarbons are recycled from there. The absorption unit is operated at high pressure. Therefore, in the process in ENR-2, the stream is compresses before the oligomerization reactor since the oligomerization reaction also favors high pressure. In the process in ENR-3, the entire process is operated at high pressure. No expander is used before the dehydrogenation and thus no compressor is needed before oligomerization or absorption. By this way, the process is further intensified and simplified by eliminating an expander and a compressor.

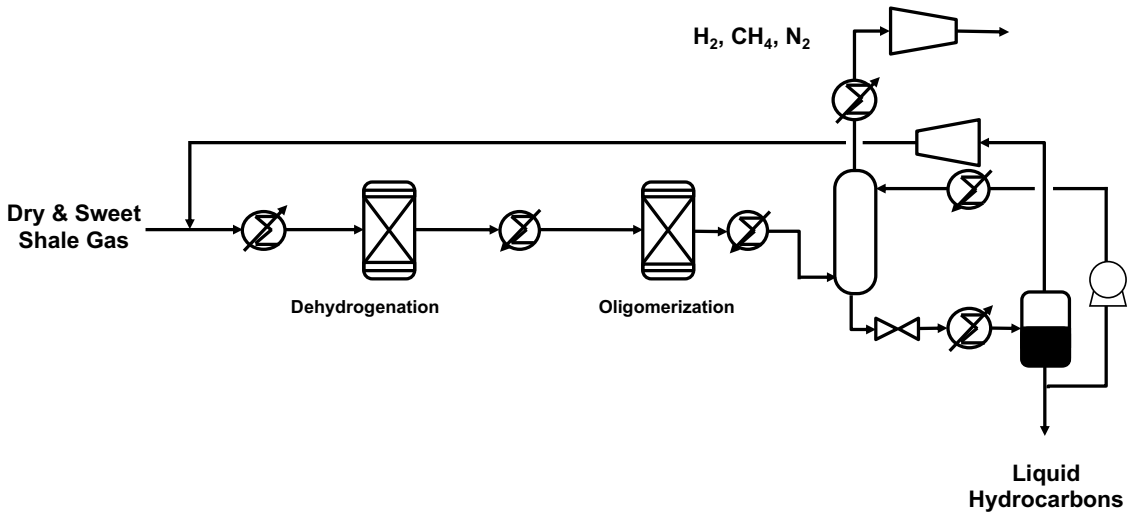

Fig. 2.12. An example of the Eliminated NGL recovery (ENR) design, referred as ENR-3, where absorption is employed and the process is operated at high pressure

2.4 Process Modeling

All the processes described in the previous section, except process SRA-1 in Figure 2.8, are simulated to evaluate their performance regarding product yields, loss of NGLs in the feed and intensification potential. We do not model the SRA-1 process because the structure that NGL recovery operated at high pressure and low temperature is between the two reactors at much lower pressure and higher temperature is not favored in process design.

2.4.1 Assumptions and modeling details

General simulation settings and assumptions

Process simulation is performed in Aspne Plus, and Peng-Robinson method is selected as the property method. The simulation is based on the shale composition from Bakken field [43], which contains 57.6% methane, 19.9% ethane, 11.3% propane, 3.8% butanes, 1.3% C_{5+} and 5.2% nitrogen (molar fraction). Usually, gas treatment is implemented at gas gather station, which usually contains shale gas from ∼10 to ∼100 wells and at the scale of 10 MMSCFD (million standard cubic feet per day) flowrate. Treated gas from gas gathering stations is delivered to centralized large-scale processing plants, usually at the scale of 100 MMSCFD, for further processing. As we focus on small-scale plants which facilitate onsite gas processing, 10 MMSCFD raw shale gas flowrate is set for our simulation, which is roughly the scale of gas gathering stations. The feedstream (raw shale gas) is assumed to be at 30 °C and 30 bar.

NGL recovery: demethanizer

In the NGL recovery, a industrial standard turbo expander scheme followed by a distillation collumn is used, as shown in Figure 2.13(a). The feed is first compressed to ∼65 bar, and then enters a cold box after pre-cooling. After exiting the cold

box, the stream enters flash vessel and generates two streams. The overhead gas stream is expanded through a turboexpander to generate refrigeration at -96° and enters the demethanizer operated at 14 bar. The liquid phase from the falsh vessel passes through a J-T valve and goes to the distillation column. Multiple streams are extracted from the column to provide cold streams to the cold box. For the processes in IRA and SRA design, the so-called NGL recovery section does not only recover NLGs, but all the C_2+ components, including alkanes and olefins, come out of the bottom of the demethanizer. For the top product, N_2 and H_2 come out together with methane if the inlet stream contains them.

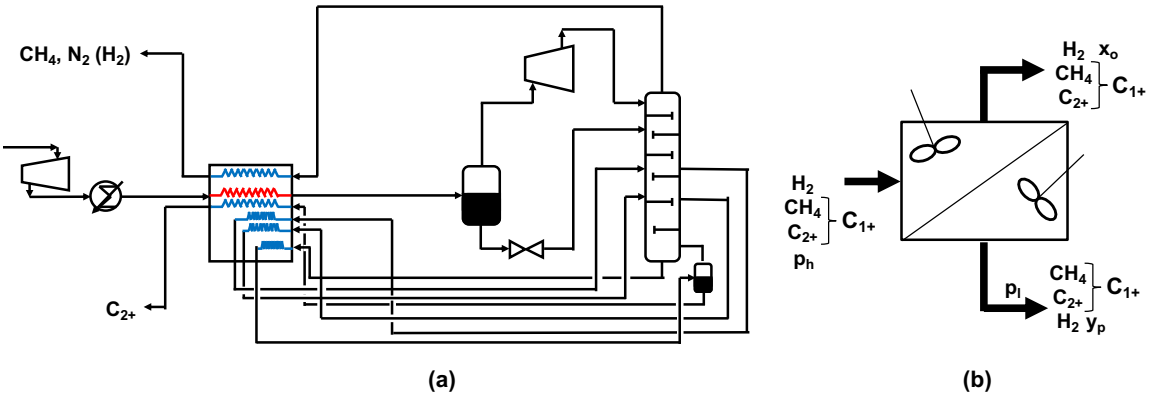

Fig. 2.13. (a) Turboexpander demethanizer for the NGL recovery section; (b) Well-mix binary membrane system for the hydrogen separation unit in NGL activation section

Dehydrogenation reactor

Dehydrogenation is the first step of NGL activation and the dehydrogenation reactor is the key reactor of the process. Although catalytic propane and butane dehydrogenation has been put into industrial practice [45] and steam cracking is widely used for ethane dehydrogenation to ethylene [46], the co-processing of NGLs to olefin is still under investigation [34]. Considering that dehydrogenation reaction

is equilibrium controlled, we assume two equilibrium model for the reactor. For both models, the reactor is assumed to be operated at 7 bar and 850 °C. REquil model in Aspen Plus is selected.

In Model I, only dehydrogenation of ethane, propane and butanes are considered, and 95% of the equilibrium conversion is assumed. The reactions considered are as following:

$$C_nH_{2n+2} \Rightarrow C_nH_{2n} + H_2 \quad n = 2, 3, 4 \tag{2.1}$$

The 95% equilibrium conversion is assumed considering the fact that the reactions are endothermic and heat transfer might be the rate-limiting step. Only mono-olefins are considered and no side reactions are accounted. All the assumptions are based on the expectation that catalysis development can make these reactions highly selective towards olefin products.

In Model II, apart from the reactions accounted in Model I, cracking of the C_{4+} hydrocarbons, including butenes and C_{5+} alkanes, are also considered. Besides reactions 2.1, following reactions are also included:

$$C_4H_8 \Rightarrow 2C_2H_4 \tag{2.2}$$

$$C_{2n+1}H_{4n+4} \Rightarrow C_nH_{2n+2} + C_{n+1}H_{2n+2} \quad n = 1, 2, 3 \tag{2.3}$$

$$C_{2n}H_{4n+2} \Rightarrow C_nH_{2n} + C_nH_{2n+2} \quad n = 3, 4 \tag{2.4}$$

Hydrogen separation

In process NCP-1 (Figure 2.6), a hydrogen separation unit is employed to partially remove the hydrogen generated in the dehydrogenation reactor. In our process model, a well-mixed binary model, as shown in Figure 2.13(b) is used to simulate the hydrogen separation unit. The feed is treated as a binary component feed: hydrogen and pseudo C_{1+} component. The permeability of the pseudo C_{1+} component is calculated by the following equation:

$$P_{C_{1+}} = \frac{\sum_i x_i^{feed} P_i}{\sum_i x_i^{feed}} \tag{2.5}$$

where i represents each component and P stands for permeability. And the equation to calculate the hydrogen concentration in the permeate is as following:

$$\frac{y_p}{1-y_p} = \frac{\alpha[x_0 - (p_l/p_h)y_p]}{(1-x_0) - (p_l/p_h)(1-y_p)} \tag{2.6}$$

where y_p is the hydrogen concentration on the permeate side, x_0 is the hydrogen concentration on the retenate side, α is the relative permeability, and p_l and p_h are the pressure of the permeate and the feed, respectively. The permeate side pressure is set to be 1 bar. The binary model is inserted in Aspen Plus with a built-in calculator. 15% hydrogen is specified on the retenate stream in order to prevent coking of the oligomerization catalyst.

Oligomerization

The oligomerization reactor is modeled by the RGibbs model in Aspen Plus. C_4 through C_{12} mono-olefins are considered as oligomerization products and only α-olefins are considered. All alkanes and hydrogen are set as inert in the reactor. The reactor is operated at 300 °C and the operating pressure depends on the inlet stream pressure.

Product recovery and recycle

The product recovery unit for all the processes, except the ENR designs, employs a two-stage condensation. In NCP, IRA and SRA designs, the first condenser is at 2 °C and the pressure of the inlet stream. The liquid stream from the first-stage condenser is expanded to ambient pressure and heated to ambient temperature. The gas from the two condensers are combined and the overhead gas stream from the second-stage condenser needs to be compressed to the same pressure as the gas from the first-stage condenser. If there is a liquid knockout from the compressor, it is directly delivered to the product stream. In ENR-1, temperature of the first-stage

condenser is at -20 °C. Although this also requires refrigeration, it would be much simpler than the refrigeration needed for a cryogenic demethanizer.

In process NCP-1, since the recovery of methane in the NGL recovery section is ∼96%, there is methane entering the NGL activation section; at the same time, hydrogen is only partially recovered in the hydrogen separation unit in the NGL activation section. Methane and hydrogen will build up in the recycle loop. Therefore, a 3% purge is taken to prevent the methane and hydrogen accumulation.

In process IRA-1, the recycled stream needs to be compressed to high pressure (30 bar) in order to be sent to the NGL recovery section. Condensation from the compressor requires liquid lockout (Figure 2.7). The lockout liquid stream mainly contains C_2 through C_4 and in IRA-1, the stream is first expanded to 7 bar, the operating pressure of the reactors, and then enters a flash vessel. The overhead gas stream, in which the highest concentration component is ethane, is recycled to the dehydrogenation reactor after heated to corresponding temperature, and the liquid stream is recycled to the oligomerization reactor after heated to 300 °C.

2.4.2 Performance metrics

The ultimate goal of our process design is to come up with simple and intensified processes that can be built onsite for conversion of NGLs. Therefore, regular process performance metrics, such as energy conversion efficiencies and exergy efficiency, are not suitable for these processes. The idea is that, as long as these processes are simple, intensified and easy to build, energy efficiencies can be sacrificed. The most important performance metrics are the ability to maximize the utilization of resources and the potential for process intensification.

Maximize the utilization of resources

Our goal is to maximize the conversion of NGLs to liquid hydrocarbon product. Two metrics are used to evaluate the ability of the process to maximize the uti-

lization of the alkane resources in the shale gas: overall product yield and loss of ethane/propane. For the overall product yield, two different calculation methods are employed for two different models of dehydrogenation calculation. For Model I, as discussed in the previous section, the only reactants from the shale gas are ethane, propane, and butanes, and final products are C_4+ olefins. For process simulated using Model I, the overall yield of product is calculated as the carbon conversion from C_2 to C_4 alkanes to C_4+ olefins:

$$\text{Product Yield} = \frac{\sum_{n=4}^{12} nF^{\text{product}}_{\text{C}_\text{n}\text{H}_{2\text{n}}}}{\sum_{n=2}^{4} nF^{\text{feed}}_{\text{C}_\text{n}\text{H}_{2\text{n}+2}}} \tag{2.7}$$

where F stands for the molar flowrate. For Model II, as all the NGL components in the feed are considered in the dehydrogenation, the overall yield of product is calculated as the carbon conversion from C_2 to C_8 alkanes to C_4+ olefins:

$$\text{Product yield} = \frac{\sum_{n=4}^{12} nF^{\text{product}}_{\text{C}_\text{n}\text{H}_{2\text{n}}}}{\sum_{n=2}^{8} nF^{\text{feed}}_{\text{C}_\text{n}\text{H}_{2\text{n}+2}}} \tag{2.8}$$

In addition, for Model I, we also calculate the single pass conversion within the dehydrogenation reactor for ethane and propane. The loss of ethane/propane is calculated as total unconverted ethane/propane that presents in all the outlet streams of the process over the total ethane/propane in the feed stream:

$$\text{Loss of ethane} = \frac{\sum F^{\text{outlet streams}}_{\text{C}_2\text{H}_6}}{F^{\text{feed}}_{\text{C}_2\text{H}_6}} \tag{2.9}$$

$$\text{Loss of propane} = \frac{\sum F^{\text{outlet streams}}_{\text{C}_3\text{H}_8}}{F^{\text{feed}}_{\text{C}_3\text{H}_8}} \tag{2.10}$$

By calculate the loss of ethane and propane, which are the major components in NGL, we can have an idea of the ability of the process to maximize the utilization of the NGL resources.

The potential for process intensification

The potential for process intensification of each configuration or process has been partly discussed in the previous sections. Here the major metrics for process intensification include:

- Number of pieces of equipment. As stated in Principle 2 in section 2.2.1, least pieces of equipment are favored for intensified processes. We could see how equipment is eliminated during the course of process development.

- Flowrate entering each section/equipment. The flowrate entering each equipment is one of the most important factors that decides the size of the equipment. Here we use relative flowrate entering the dehydrogenation reactor to get an idea of the size of the reactor for various processes. The basis for the relative flowrate is the NGL flowrate in the feedstock:

$$\text{Relative flowrate } F^{\text{Dehydro-in}*} = \frac{F^{\text{Dehydro-in}}}{F^{\text{Feed}}_{\text{NGLs}}} \tag{2.11}$$

- Potentials for simple operation.

2.5 Results and Discussion

Detailed stream information of each process can be found in Appendix D. The results regarding the performance metrics modeled by Model I and II are listed in Table 2.1 and Table 2.2, respectively.

Table 2.1.
Key performance results for various flowsheets modeled by Model I

	C_2H_6 loss (%)	C_3H_8 loss (%)	Product yield (%)	Relative flowrate entering dehydro
NCP-1	26.6	3.5	74.0	2.9
IRA-1	4.9	2.1	89.2	2.2
SRA-2	1.5	1.2	91.5	3.9
ENR-1	37.0	8.6	39.1	2.9
ENR-2	1.6	0.4	92.4	4.3
ENR-3	5.4	1.6	90.1	5.6

Table 2.2.
Key performance results for various flowsheets modeled by Model II

	C_2H_6 loss (%)	C_3H_8 loss (%)	Product yield (%)	Relative flowrate entering dehydro
NCP-1	63.1	2.3	15.7	1.4
IRA-1	7.3	0.1	75.1	2.0
SRA-2	2.6	0.1	76.0	3.8
ENR-1	50.4	0.6	31.2	2.8
ENR-2	3.7	0.0	80.0	3.9
ENR-3	30.2	0	68.2	4.5

2.5.1 Benefits and limits of each process

From Table 2.1 and Table 2.2 we could see that, overall, Model II gives lower product yields than Model I, this is because Model II considers the cracking of C_{3+} NGLs in the feedstocks and methane is formed. However, note that both these models are equilibrium models and do not take all the actual reactions within dehydrogenation reactor into account. For a more accurate simulation, kinetics [47] and heat transfer [48] should all be considered in modeling the dehydrogenation reactor, which is beyond the scope of this study. Since we only focus on the process design and intensification, employment of a simple equilibrium model is sufficient to analysis these processes. For the following analysis, we use the results from Table 2.1 as both models show the same trend within differenct processes.

To begin with, we focus on process NCP-1, which is proposed by Ridha et al [43], to see the limitations of this heuristic design after we eliminate the NGL fractionation section and co-process all the NGL components. First, the 31.6% ethane is one of the reasons for the low overall yield of liquid products. For all the ethane loss, 64% of the loss is due to the NGL recovery section. The demethanizer cannot clearly separate all the methane and NGLs clearly, and 20% of the ethane in the feed is not recovered

in the NGL stream. This causes a loss of the ethane resource and accounts for the low product yield of the process. 23% of the ethane loss is attribute to the hydrogen separation. Since a membrane is used for separation, ethane, together with 5.5% of the ethylene coming out of the dehydrogenation reactor, is lost with the hydrogen stream from the hydrogen separation unit due to the limit of selectivity. What is more, 12% of the ethane loss comes from the purge stream. As the purge is necessary to prevent the build-up of methane and hydrogen in the recycle loop, ethane, together with ethylene loss due to the purge is inevitable. Another drawback of the NCP-1 flowsheet is that due to the existence of hydrogen in the recycle loop, there is 14% of hydrogen in the inlet stream of the dehydrogenation reactor, which will resist the equilibrium conversion of NGLs to olefins. Therefore, though the NCP-1 process eliminate the NGL fractionation section which largely reduce the equipment needed for the process, multiple drawbacks of the flowsheet still exists, and the product yield is not high.

To deal with the ethane loss and thus the low overall product yield, the IRA process eliminate the need for a purge stream by including the demethanizer into the recycle loop and getting rid of the membrane for separating hydroge. In this way, the loss of ethane due to the hydrogen separation and the purge is avoided. Furthermore, due to the existence of hydrogen within the stream entering the demethanizer, the separation is easier to operate and better separation can be achieved. Here only 5% of the ethane in the feed comes out of the demethanizer together with separated methane and hydrogen. Higher methane recovery is also achieved and therefore reduces the methane entering the NGL activation section. In addition, as H_2 is separated together with methane from the demethanizer, hydrogen does not present in the stream entering the dehydrogenation reactor, which is favored by the dehydrogenation reactions. All these factors add up to the modeling result that the loss of ethane, the critical component in the NGLs, has been reduced by $\sim$70% and the loss is only 6.1% in process IRA-1. The single pass conversion of ethane within the dehydrogenation reactor has also increased, from 34.4% in NCP-1 to 41.8% in IRA-1. The reduction in ethane

(same for ethylene and C_3) loss and increase in dehydrogenation conversion, together lead to the increase yield of liquid products. From Table 2.1 we can see that the overall product yield has increase from 72.0% to 87.9%, comparing IRA-1 to NCP-1. From the perspective of process intensification, on one hand, the hydrogen separation is eliminated, which reduces the equipment of the process; on the other hand, the integration of the two sections is a means of intensification, where the demethanizer takes up multiple roles: separation of methane and NGLs, and purge. In addition, the flowrate entering the dehydrogenation reactor is reduced by ∼32%. Under the same operation conditions, both reactors will take up smaller flowrate and requires smaller size, which also benefits the process intensification.

As we discussed before, if we would like to further improve the single pass conversion within the dehydrogenation reactor, a diluent stream could be introduced. Using methane from the shale gas feed will not introduce additional equipment and streams, and by this means the SRA configuration is proposed and SRA-2 is a promising example process. In process SRA-2, we can see from Table 2.1 that the loss is ethane and propane is further reduced and product yield is further improved to 90.5%. Furthermore, as stated in section 2.2.3, a cracker can be used for dehydrogenation instead of a catalyst bed, which will be much simpler to control and operate. No catalyst regeneration is needed and the heat of the cracker can be provided by burning methane separated from the NGL recovery section. In this way, pieces of equipment is furthered reduced. However, as the entire sweet and dry shale gas stream is processed to the dehydrogenation reactor, the flowrate of the dehydrogenation reactor will be huge. As we can see from our simulation result, the flowrate is ∼16% higher than the NCP-1 process. Here it would be a trade-off between higher yield/utilization of resources/simple operation and high flowrate. Or the reactor could be operated at higher pressure to reduce the size, but sacrifice the high single-pass conversion of 50.2%. In general, SRA-2 is a process with high liquid product yield with little loss of NGL resources, and is amendable to a simple design of the dehydrogenation reactor. The process does not stick to the four-section design-hierarchy and compared to pro-

cess IRA-1, the process intensification lies in the utilization of methane as a diluent as well as a thermal mass.

Since the demethanizer requires high pressure and low temperature, the ENR designs are proposed to eliminate the energy and capital-intensive unit. However, when process ENR-1 only uses a condenser at -20 °C, ∼50% of the ethane in the feed comes out of the top of the condenser, which leads to the low product yield of 16.6%. Though the flowrate entering the dehydrogenation reactor seems low compare to that in NCP-1 and SRA-2, it is also due to the large ethane loss in the first-stage condenser. Therefore, although a complex demethanizer is no longer preferred under the target of simple process, an effective separation method is still needed for the methane (and hydrogen) separation. Absorption is a good choice, and according to our principle to keep the process simple, no additional introduced stream is favored. Therefore, taking part of the liquid hydrocarbon as absorbent can be a good synergy within the process. From Table 2.1, we can see that by employing absorption into the ENR design, the loss of ethane is reduced from 50.1% in ENR-1 to 1.5% in ENR-2. The loss is the least among all the processes we proposed and simulated. A high product yield up to 92.5% is achieved. Although the flowrate entering the dehydrogenation reactor is ∼13% higher than that in the NCP-1 process, ENR-2 has eliminated most of the complicated units, such as distillation columns and membranes. This is still a promising process intensification in terms of the process simplicity and high yield of production. As for the ENR-3 process, the entire process is operated at high pressure so that expanders before the dehydrogenation and on the recycle stream are eliminated, as well as the compressor before the oligomerization reactor. From the modeling results shown in Table 2.1, we can see that the loss of ethane and propane is slightly higher than that in ENR-2, but still a very low level. The overall product yield is slightly lower than that in ENR-2, but still higher than 90%. The flowrate entering the dehydrogenation reactor is the highest among all the processes, but as it is operated at high pressure, the size of the reactor can still be kept small. With the least number of pieces of equipment, ENR-3 is the simplest processes we proposed.

2.5.2 Process intensification

The scope of process intensification has been evolved to adapt to various circumstances and goals. In the early times, process intensification focuses only on the smaller-sized equipment. However, the definition of process intensification has been extended to process development methods that offer substantial improvements in manufacturing and processing [49]. Here we extend the definition of process intensification to process development that generates simple and easy to operate processes, which could potentially lead to distributed manufacturing. Considering the distributed processing demand from remote shale locations, as well as the spacial and temporal variation of shale gas production, onsite processing of NGLs is a perfect example of process intensification application. As we discussed in section 2.2.1, breaking the design hierarchy, minimizing the number of unit operations and keeping the unit operations simple are important principles for process intensification that can be applied for onsite production. During the course of our progress coming up with processes discussed in this study, those principles have been put into practive.

Starting the traditional four-section shale gas processing, we break the design hierarchy when each new configuration is proposed, either by eliminating a certain section or shifting the order of the sections. By adjusting these sections, improvement in processes, such as higher product yields and easier operation, is realized, which complies with the process intensification goal of improvement in processing.

Each of the configuration shows how to minimize the number of unit operations and number of equipment: from CSP configuration to NCP configuration, NGL fractionation train is deleted from the processing scheme; from NCP-1 to IRA-1, hydrogen separation is no longer needed; from SRA designs to ENR designs, the entire NGL recovery section is eliminated and a much simpler separation method takes the place; from ENR-2 to ENR-3, even pressure changing equipment is reduced. All these practive in our process design comply with the principle of minimizing the number of

unit operations. These also align with the definition of intensification by generating simple processes.

Attention is also given to the unit operations. From catalytic conversion to a cracker in the dehydrogenation unit, from cryogenic distillation to absorption, these changes in unit operations lead to potential of simpler operation and control, which will also benefit the varying feed at the same time. In addition, when a new stream needs to be introduced, synergy within the process, or internal stream is considered first. Examples are methane used as diluent and liquid hydrocarbon used as absorbent.

2.6 Conclusion

In this chapter, we propose four new configurations for NGL processing, and several example processes are provided to show how these designs evolved. Instead of being flared or shifting to a centralized plant, NGLs from remote shale plays can be processed onsite by these processes to liquid hydrocarbons for extra values. Simple processes with easy to operate unit operations and reduced pieces of equipment improve the performance of processing, with higher product yield and less loss of NGLs. Among all the processes proposed, the higher yield of product can achieve 92.5%. The process intensification strategies in this study include eliminating unnecessary unit operations, employing simpler separation methods, using existing streams but not introducing new streams, shifting the order of traditional process units. The process intensification will benefit the modularization of the plant, and is suitable for the application of distributed manufacturing at remote shale plays where there is no transportation infrastructure.

3. SYSTEMATIC LAND REQUIREMENT ANALYSIS FOR A SOLAR ECONOMY

3.1 Introduction

Solar energy is our most ubiquitous and promising renewable energy resource that has the potential to meet our future energy demands due to its sustainable availability and abundance [13]. Replacing fossil resources with solar power provides an opportunity to eliminate much of the world's pollution, greenhouse gas emissions, and energy security challenges. However, solar energy is a dilute source with power density several orders of magnitude lower than fossil fuels [6]. Harnessing solar energy therefore requires vast tracts of land. A number of studies have envisioned a fossil fuel-deprived future powered by solar energy. In most of these previous studies, land availability is not a constraint to the feasibility of a solar powered future. For example, Turner has estimated that no more than 1% of the land in the United States (US), if used for photovoltaics (PV), could provide all the energy needed for the entire country [50]. Fthenakis et al. has reported that it is "clearly feasible" to replace the current fossil fuel infrastructure in the US with solar energy and other renewable; moreover, 90% of the solar production can be located in the US southwest [51]. Jacobson et al. has also envisioned the scenario where no more than 2% of the land in the US could supply the energy demand [52]. While these researchers are optimistic about the total solar economy, several recent land requirement analyses have raised the concern in land availability in some densely populated countries. MacKay has suggested that transition to a total solar economy in Britain would require land area similar to the area of the entire country and that several other high-density, high-consuming countries, such as Japan and Germany, are facing the same challenge [53]. A recent land requirement analysis by Capellán-Pérez et al. over 40 countries around

the world has also pointed out that it could be physically infeasible for many densely populated countries to domestically harness renewable energy to maintain the current energy consumption [54]. According to these recent land requirement estimations, for countries with an overall relatively low population density, such as the US, there seems to be sufficient land available for PV park construction and land limitation for the country as a whole has never been a concern.

However, if we examine the distribution of energy consumption and solar radiation in the US, we would anticipate that substantial energy demand of the populated states in coastal and great lake regions will have to be supplied from less populated areas in the southwest. Dispatching electricity from a remote state such as Nevada to states such as New Jersey thousands of miles away will require construction of expensive and risky super grids operating at extremely high voltages to minimize transmission losses [55]. Therefore, local sustainability is greatly preferred for the solar economy. We would like to see if solar photons could locally fulfil the energy demand. In this chapter, an extensive systems model for detailed land requirement analysis is developed for each of contiguous 48 states of the US for a full solar economy. We find that it will be difficult, even in a large and relatively sparsely populated country such as the US, to meet the energy needs using current solar park designs for the contiguous 48 states as a whole and for nearly half of the individual states, which include well over half of the total US population.

In addition, the land requirement analysis methodology is applied to highly populated countries such as the United Kingdom (UK) and Germany as well as developing countries such as China. From these analysis, we find out that the solar economy could be potentially land constrained around the world and unlikely to be realized in the absence of innovative land intensification strategies.

3.2 Energy Demand in a Solar Economy

3.2.1 Method for predicting power demand

To examine the land requirement for a solar economy, the energy demand will need to be estimated first. This section introduces the estimation method employed for the case study of the US, and the method is summarized in Figure 3.1. Two scenarios,

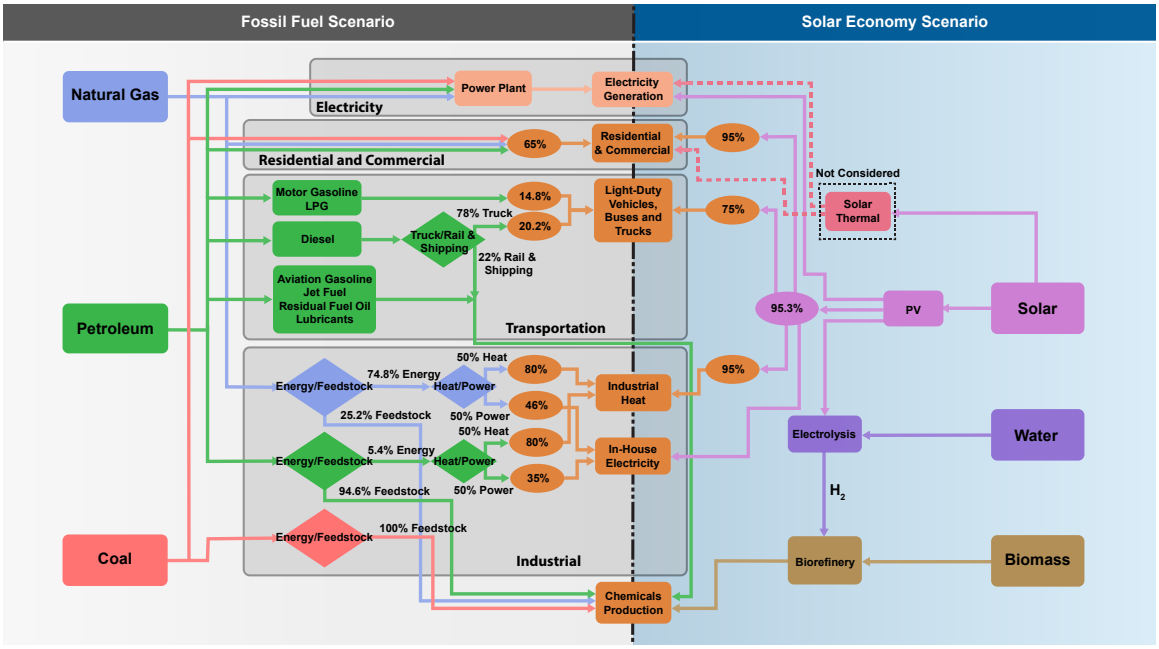

Fig. 3.1. Detailed calculation model for a fossil fuel to solar energy transition. Diamonds indicate the splitting of energy use and ovals indicate efficiencies for the corresponding steps.

the current fossil fuel scenario (FFS) and the projected solar economy scenario (SES), are considered in our energy demand estimation. Energy consumption data of 2014 from the Energy Information Administration (EIA) [22] are adopted for the FFS and the energy demand for SES is estimated based on these data. In the SES, only photovoltaic panels (PV) are deployed for solar energy conversion for the purpose of this study. Concentrating solar thermal power (CSP) facilities and small scale solar

thermal heating (for residential heating, for example) are not used in our analysis. As PV electricity will become the dominant form of energy supplied to end-use sectors, the energy demand analysis becomes power requirement estimation. For the transition from the FFS to the SES, fossil fuels will be completely replaced by PV, while other energy resources used in the FFS, such as wind and hydro power, are assumed to remain at the same utilization in the SES. To maintain the current lifestyle and life quality, the end use demands are kept the same for the FFS and the SES.

The transition to a solar economy will reshape the current energy supply and consumption infrastructure. In the FFS, fossil fuels as energy resources are either used for power generation or directly supplied to end use sectors. Now that we have assumed PV as the only method for solar harnessing and conversion, electricity will become the form of energy ultimately supplied to end uses and nearly all the end use facilities will be electrified in the SES [18]. Systems that might not be feasibly electrified, such as air-transportation, are taken to be powered by synthetic fuels synthesized from biomass [56] [15]. In addition, a small part of fossil resources is consumed as chemical feedstocks in the FFS and these fossil resources will be replaced with biomass in the SES. To look at the future solar electricity demand, a detailed examination into each end use sector is performed. In our model, we treat power generation as a separate sector and only direct primary energy consumption is considered for the residential, commercial, industrial and transportation sectors. Chemical and fuel production from biomass is also treated as a standalone sector. Electricity demand in the SES to replace fossil fuels in the FFS is examined for each sector and the total electricity demand is the sum of electricity demand in each sector calculated by the following equation:

$$E^{SES} = \sum_{k} E_k^{SES} \tag{3.1}$$

where k represents electricity, residential, commercial, transportation, industrial, chemical and fuel demands, and where E^{SES} represents the total electricity demand

from PV in the SES and E_k^{SES} represents the electricity demand for sector k in the SES.

Electricity sector

For the electricity sector ($k = electricity$), power generation data in the FFS are from EIA (Net Generation by State by Type of Producer by Energy Source, 2014) [57]. We assume the electricity flow to be the same after generation, whether this is from a fossil fuel powered plant (FFS) or PV parks (SES), including the same transmission and distribution loss and the same end use electricity conversion efficiency. As a result, the electric power generated from fossil fuels can be simply replaced with the same amount of electricity generated from PV. Therefore, the total electricity from PV needed to replace the electricity from fossil fuels in the FFS is calculated by the following equation:

$$E_{electricity}^{SES} = E_{electricity}^{FFS} \tag{3.2}$$

where $E_{electricity}^{FFS}$ represents the electricity generated from fossil fuels in the year of 2014.

Residential and commercial sector

For the residential ($k = residential$) and commercial ($k = commercial$) sector, the SES electricity requirement is estimated by ensuring that the end-use energy consumptions are the same for the FFS and SES under different energy conversion efficiencies. The estimation paradigm is expressed by the following equation:

$$E_k^{SES}\eta_k^{SES}\eta_{transmission}^{SES} = \sum_i E_{i,k}^{FFS}\eta_{i,k}^{FFS} \tag{3.3}$$

where the subscript i refers to the fossil fuel (i = coal, petroleum, natural gas). In Equation 3.3, $E_{i,k}^{FFS}$ refers to the energy consumption by fossil fuel i in the FFS in sector k, $\eta_{i,k}^{FFS}$ refers to the energy conversion efficiency from fossil fuel i to the end use in the FFS in sector k, η_k^{SES} refers to the energy conversion efficiency from electricity

to the end use in the SES in sector k and $\eta^{SES}_{transmission}$ refers to the transmission and distribution efficiency for the electrical grid in the SES. Fossil fuels supplied directly to residential and commercial sectors are generally used as heat. End use efficiency for fossil fuels is estimated as 65% for these sectors in FFS ($\eta^{FFS}_{i,residential} = \eta^{FFS}_{i,commercial} =$ 65%) [58]. After switching to SES, electrical heating is much more efficient and a 95% efficiency is assumed ($\eta^{SES}_{residential} = \eta^{SES}_{commercial} = 95\%$). The transmission and distribution loss of electrical grid is taken to be 4.7% [59] and therefore the value of $\eta^{SES}_{transmission}$ is 95.3%.

Transportation sector

For the transportation sector, only natural gas and petroleum are consumed according to EIA's energy consumption data. Moreover, as most natural gas consumption is attributed to the operation of pipelines, primarily in compressors, natural gas consumption in transportation sector is negligible in a SES [22]. Therefore, only petroleum is considered here in the transportation sector. The estimation of electricity demand for the transportation sector is also achieved by equating end-use consumption for the FFS and the SES. However, in the transportation sector, only part of the petroleum consumption can be directly replaced by electricity from PV. The electricity demand is calculated by the following equations:

$$E^{SES}_{j,transportation}\eta^{SES}_{transportation}\eta^{SES}_{transmission} = E^{FFS}_{j,transportation}f_j\eta^{FFS}_{transportation} \tag{3.4}$$

$$E^{SES}_{transportation} = \sum_j E^{SES}_{j,transportation} \tag{3.5}$$

where the subscript j refers to a specific category of petroleum (motor gasoline, liquefied petroleum gas (LPG) or diesel). For the transportation sector, only light-duty vehicles, buses and trucks are projected to be replaced by electrical vehicles (EV) and these means of transportation are powered by motor gasoline, LPG and diesel in the FFS. Other means of transportation, such as air and marine vessels, will not be easily electrified and the fuels for them are to be produced from biomass,

which will be discussed in the chemical and fuel production sector. In Equation 3.4 and 3.5, $E^{SES}_{j,transportation}$ is the electricity demand to replace fuel j in the SES for the transportation sector, $\eta^{SES}_{transportation}$ is the efficiency of EV, $E^{FFS}_{j,transportation}$ is the energy consumption by fuel j in the FFS for the transportation sector, f_j is the fraction of fuel j that are consumed by the means of transportation that could be electrified (for example, 78% of the diesel are consumed by trucks [60], which can be replaced by EV and the rest of diesel consumption by ships will not be replaced by electricity; therefore $f_{diesel} = 78\%$) and $\eta^{FFS}_{j,transportation}$ is the efficiency of internal combustion engine powered by fuel j. Here in our estimation, all the motor gasoline and LPG for transportation can be replaced by electricity, and diesel consumed by trucks can also be replaced ($f_{motorgasoline} = f_{LPG} = 100\%$; $f_{diesel} = 78\%$ [60]); the grid-to-wheel efficiency of EV is assumed to be 75% ($\eta^{SES}_{transportation} = 75\%$) [61]; internal combustion engine efficiencies average 14.8% for gasoline (LPG) engines and 20.2% for diesel engines, respectively (that is, $\eta^{FFS}_{motorgasoline,transportation} = \eta^{FFS}_{LPG,transportation} = 14.8\%$; and $\eta^{FFS}_{diesel,transportation} = 20.2\%$) [62].

Industrial sector

For the industrial sector, fossil fuels are used as either energy sources or feedstock in the FFS. Fossil fuels used as energy resources are to be replaced by electricity, while those used as chemical feedstocks will be discussed later in the chemical and fuel production sector. The ratio of energy to feedstock in each state is assumed to be identical to the national ratio in our calculation. For the fossil fuels supplied as energy, they can be consumed for both heat and in-house generated power. The electricity demand in the SES for the industrial sector is estimated using the following equations:

$$E^{SES}_{heat,industrial}\eta^{SES}_{heat,industrial}\eta^{SES}_{transmission} = \sum_i E^{FFS}_{i,industrial} g_{i,energy} h_{i,heat} \eta^{FFS}_{i,heat,industrial} \tag{3.6}$$

$$E^{SES}_{power,industrial}\eta^{SES}_{transmission} = \sum_i E^{FFS}_{i,industrial} g_{i,energy} h_{i,power} \eta^{FFS}_{i,power,industrial} \tag{3.7}$$

$$E^{SES}_{industrial} = E^{SES}_{heat,industrial} + E^{SES}_{power,industrial} \tag{3.8}$$

where the subscript i refers to the fossil fuel (i = coal, petroleum or natural gas). $E^{SES}_{heat,industrial}$ and $E^{SES}_{power,industrial}$ refers to the electricity requirement in the SES to replace fossil fuels for industrial heat and in-house power generation, respectively. $\eta^{SES}_{heat,industrial}$ is the electrical heating efficiency in the industrial sector in the SES, which is assumed to be 95%. $E^{FFS}_{i,industrial}$ is the energy consumption of fuel i for the industrial sector in the FFS; $g_{i,energy}$ is the fraction of fuel i consumed as energy (in our study, $g_{naturalgas,energy} = 74.8\%$, $g_{petroleum,energy} = 5.4\%$ and $g_{coal,energy} = 0$ for every state [60]). $h_{i,heat)}$ and $h_{i,power}$ are the fraction of fuel i consumed by industrial heat and in-house power generation, respectively. We assume $h_{i,heat} = h_{i,power} = 50\%$. $\eta^{FFS}_{i,heat,industrial}$ and $\eta^{FFS}_{i,power,industrial}$ are the energy conversion efficiencies of fuel i to industrial heat and power, respectively ($\eta^{FFS}_{i,heat,industrial} = 80\%$, $\eta^{FFS}_{naturalgas,power,industrial} = 46\%$ and $\eta^{FFS}_{petroleum,power,industrial} = 35\%$ [22].

Chemical and fuel production

For chemical and fuel production, chemical feedstocks from fossil fuels and fuels for transportation that cannot easily by electrified is produced from biomass in the SES [63]. The biomass required for the chemical and fuel production in the SES is estimated to be ∼857 million tonnes. According to the US Department of Energy, the sustainably available biomass production will have the potential of over 1 billion tonnes by 2040 [64] [65]. Therefore, there will be sufficient biomass for chemical and fuel production for the SES. Since biomass is easy to transport, we do not consider the local availability of biomass here. Also, as sustainably available biomass is used, its production will not compete with normal food and forestry production.

Since these chemicals and fuels in the FFS are mainly hydrocarbons, we assume that these fossil fuels are purely composed of CH_2 units. Typical biomass is composed of CH_2O units; thus, the oxygen needs to be removed by biorefining. In biorefining, H_2 is obtained from water electrolysis and used to remove oxygen in biomass [66]. We

can estimate the energy requirement of biorefining to replace fossil fuel feedstocks by determining the amount of H_2 required according to the amount of biomass to be upgraded, then calculating the electricity needed for water electrolysis. This estimation can be expressed by the following equation:

$$E^{SES}_{chemical\ and\ fuel} = \frac{W^{FFS}_{chemical\ and\ fuel}}{M_{CH_2}} \times \Delta H_{water\ electrolysis} \tag{3.9}$$

where $W^{FFS}_{chemical\ and\ fuel}$ is the total mass of fossil fuels used as chemical and fuels in the FFS, M_{CH_2} is the molar mass of the CH_2 unit and $\Delta H_{water\ electrolysis}$ is the energy demand for producing 1 mol of hydrogen by water electrolysis.

By examining each sector, we can estimate the total electricity demand for the SES and since our land requirement estimation is based on the power output of PV parks, we would like to know the power demand for the SES. The total power demand for the SES can be obtained by averaging the total electricity demand over the entire year:

$$P^{SES} = \frac{E^{SES}}{T} \tag{3.10}$$

where P^{SES} is the total power demand in the SES and T is the total time of a year.

3.2.2 Intermittency of solar energy and storage efficiency

One of the essential challenges of a solar economy is the intermittency of solar energy availability. In the US as a whole, solar energy is available for only $\tilde{2}0\%$ of a 24-hour day on average, necessitating storage [13]. We assume that the end-use electricity during the time when solar energy is not available (80% of the day) must be stored in our calculation. Various energy storage methods could be used to store the generated solar power from PV and recover the energy when solar energy is not available. For large-scale energy storage, thermal energy storage, chemical energy storage (e.g., carbon storage cycle), pumped hydroelectric storage, compressed air energy storage, and batteries (electrochemical) are among the alternative methods [67] [68] [66]. The energy storage efficiencies range from 55% to 95%. Assume that

mixed storage methods will be adopted in a solar economy and a storage efficiency of 65%, which is in the midst of various storage efficiencies, is adopted for this study. As a result, 43% more electricity must be generated than our estimated end-use electricity demand in the SES to offset storage losses. For state-level calculation, average solar available time data for each state is used [69], and similarly, power generation during the time when solar energy is not available will be stored and a storage efficiency is considered. However, since the storage efficiency largely decides the total power requirement, we also investigate cases where storage efficiency is assumed to be 55% and 80%, respectively.

3.3 Land Requirement Analysis

3.3.1 Power recovered from current PV parks

Although the maximum solar cell efficiency reported to date can be up to 47% [70], the actual PV power output per unit land area is generally lower than estimated. Apart from the gap between research and industrial application, this is because of many constraints under which a PV park is constructed and operated. For example, certain distance should be kept between rows of solar panels to avoid shadow cast on one module by another and to enable easy access for maintenance vehicles. Thus, we use actual power density output data of PV parks in our calculation.

Figure 3.2 is adapted from reference [53], indicating PV parks' average power per unit land area versus the local insolation (i.e. average incident solar flux per unit of horizontal land area). From Figure 3.2 we can see that for locations in the US with solar insolation above 160 W/m^2, the generated power from PV parks averaged over the entire year including day and night ranges from 4.3 to 11.4 W/m^2. The national average in the US of the PV parks' power output per unit land area is $\sim$7 W/m^2. At the same time, we can see that the power outputs per unit land area for UK and Germany are between 4 to 5.3 W/m^2; the land challenge for these densely populated European countries could be more severe than the US.

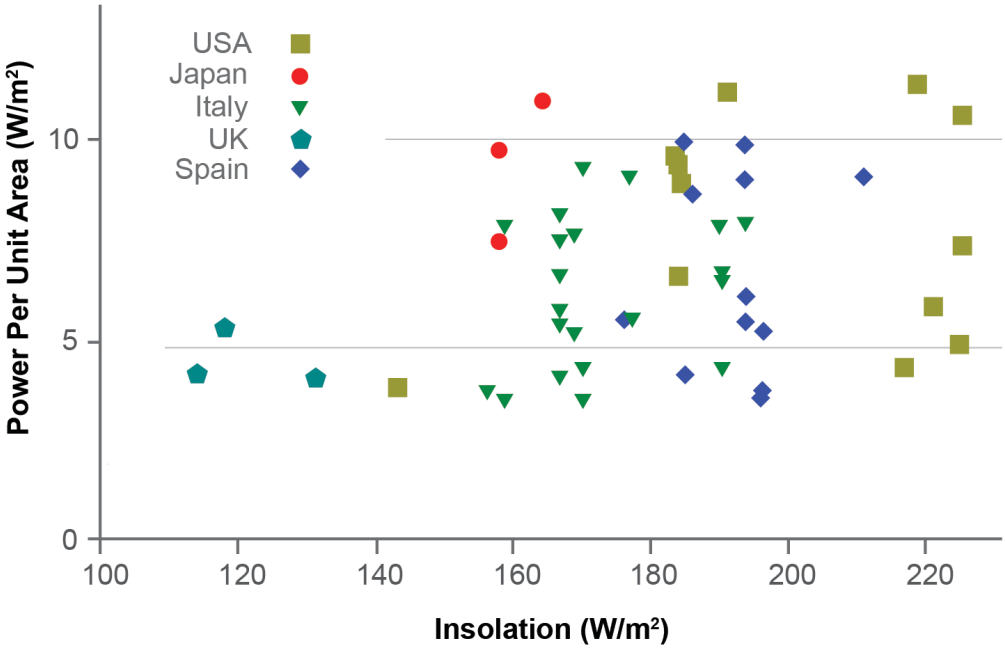

Fig. 3.2. Solar parks' average power per unit land area versus the local insolation

3.3.2 Major land uses in the US

Major land uses in the US discussed in this study are based on the information from USDA Economic Research Service [25]. Major land uses in the US includes six land use types: cropland, grassland pasture and range, forest-use land, special use area, urban use area and other or miscellaneous land. The accurate definition of each type can be found in reference [25] or [71].

Among all land types, cropland and grassland pasture and range are collectively referred as agricultural land in this study. For cropland, crop growth on the ground is important for its food output. Similarly, for grassland pasture and range, plant growth on the ground is important for livestock growth and thus important for its food production. At the same time, if we consider PV panel installation, farming equipment movement on cropland should not be blocked; similarly, livestock activities on pastures and range should not be hindered. Due to these similarities, cropland

and grassland pasture and range are combined as agricultural land in this study. Agricultural land accounts for 53.9% of the total land area of the contiguous US.

If preservation of wildlife habitats and agricultural output remain priorities, most open land area (forests, national and state parks, agricultural land, etc.) is not available for existing PV panel installation. Forest-use land accounts for 30.4% of the total land area. Special use area, which accounts for 8.9% of total land area, includes highways, roads, railroad rights-of-way airports, Federal and State parks, wilderness areas, wildlife refuges, national defense and industrial areas, farmsteads and farm roads. Urban use area accounts for 3.2% of the total land area. Miscellaneous land accounts for 3.6% of total land area and includes industrial and commercial sites in rural areas, cemeteries, golf courses, mining areas, quarry sites, marshes, swamps, sand dunes, bare rocks, deserts, tundra, rural residential, and other unclassified land. [25] [71] Only part of the miscellaneous land and urban land are available for PV installation. However, note that not all of the miscellaneous land, such as marshes, swamps and bare rocks, can be used for large scale PV installation. In the cases discussed in the main text, the usable area from miscellaneous land is assumed to be 50%. However, we have also investigated more cases with miscellaneous land usage of 25% and 75%.

3.4 Case Study for the Contiguous US

3.4.1 The contiguous US as a whole

The 100% solar powered economy is studied here only as a bookend case due to the widespread accessibility of solar energy and its relatively high power output per unit land area compared to wind energy [72] [24]. Although we focused on the solar end, this does not imply that wind or other renewable resources will not be used in practice. Instead, when feasible, wind and solar energy should be used to supplement each other.

By the method discussed in section 3.2.1, the total power required for the contiguous US in the SES is estimated to be 1164 GW. Considering the intermittency and energy storage loss, an estimated total of 1665 GW of generation is required. we assume that 50% of miscellaneous land is usable for PV parks. Meanwhile, some urban areas could be dedicated to rooftop or building-integrated PV systems. Studies have suggested that 1–12% of urban areas could be used for PV panels [73] [74] [75].

For the entire contiguous US, based on the total estimated SES power demand of 1665 GW and the average power output of $\sim$7 W/m^2 from PV parks, besides 50% of the miscellaneous land area, $\sim$41% of the urban area would be needed for PV parks. Even if the output of PV parks can reach 11 W/m^2, which is highly optimistic, the corresponding percentage of the total urban area needed is estimated to be 5.6%, in addition to 50% of the miscellaneous land. For the entire contiguous US, this high urban land requirement reveals that the solar economy could be land constrained.

3.4.2 Land analysis at state level

To determine the feasibility of a local solar economy at the state level in the contiguous United States, we calculated the power density requirement for each state using the estimated solar power demand and the potentially usable land for each state. From Figure 3.3(a), we see that if 50% of the miscellaneous land and 5% of the urban land were available for PV systems, the power density requirement of 24 states would be greater than 11 W/m^2, while for nine states it would be between 7 and 11 W/m^2. If 15% of the urban land could be used, which is a very optimistic assumption, 20 states would still require a power density exceeding 11 W/m^2, while ten states would require 7-11 W/m^2 (Figure 3.3(b)). In either case, many of these states are relatively densely populated, such as New York, New Jersey, Maryland, Delaware, Florida and Illinois. Others, such as Indiana and Wyoming, will require high power densities, since most of their land is devoted to agriculture (cropland or pasture). For these states, additional land area besides the miscellaneous and urban land will be needed for PV installation.

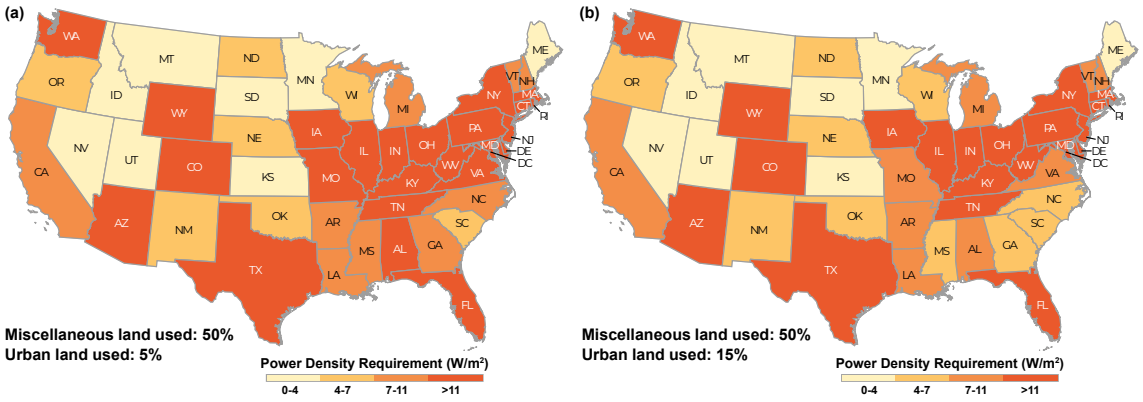

Fig. 3.3. Power density requirement of each state when 50% of its miscellaneous land and 5% (a) and 15% of urban land (b) is used for PV installation

We also investigated cases with different percentages of miscellaneous land usage, PV power density output and energy storage efficiencies, and the results remain similar (that is, a large number of states require additional land besides miscellaneous and urban areas). The results with more cases are summarized in Table 3.1.

3.4.3 Case studies for other selected countries

Apart from the US, we are also interested in the land requirements for a solar economy in other countries of the world. Two densely populated developed countries, the UK and Germany, and a fast-developing country with large population, China, are selected as examples to illustrate the land issue worldwide. Due to the limitation of data, we only present the results for the country-level study; however, for large countries such as China, local analysis is expected to show more severe land challenges.

The method for predicting power demand discussed in section 3.2 is applied to these selected countries. Data of primary energy consumption are acquired from International Energy Agency (IEA) [23]. Note that because of the location of the

Table 3.1.
Results summary for multiple land requirement analysis cases

Miscellaneous land use (%)	Urban land use (%)	Storage efficiency (%)	PV park output (W/m^2)	Number of states with insufficient urban + miscellaneous land
25	5	55	7	44
25	5	65	9	39
25	5	80	11	33
50	5	55	7	36
50	5	65	9	27
50	5	80	11	21
75	5	55	7	27
75	5	65	9	21
75	5	80	11	16
25	15	55	7	44
25	15	65	9	36
25	15	80	11	26
50	15	55	7	33
50	15	65	9	25
50	15	80	11	17
75	15	55	7	26
75	15	65	9	19
75	15	80	11	13

UK and Germany, the power output per unit land area from PV parks for these two countries is assumed to be 5 W/m^2, while for China it is assumed to be 7 W/m^2 [53].

The results for the United Kingdom and Germany show that 10.2 and 12.1% of the total land will be needed for PV parks, respectively. However, according to the World

Bank, 83.8% of the land in the United Kingdom and 80.7% of the land in Germany is devoted to agricultural or forest uses [76] [77]. Remaining land uses include urban uses of which only a small portion can be used for PV installation and other special land uses not suitable for PV parks. Thus using the remaining land area for power generation is extremely challenging.

For China, 2.9% of the land will be needed based on current energy consumption and this number might increase to 3.5% based on energy consumption projection in China [78] [23]. China has 78.4% of agricultural and forest land [76] [77]. Though the remaining land seems sufficient for PV installation, glacier, mountainous area, shifting sand dessert are all included in the remaining land area, which can hardly be used for PV. In addition, no more than 15% of urban land can be used [73] [74] [75]. Furthermore, population, as well as energy consumption, is highly unevenly distributed in different parts of China. Approximately 55% of the country's land area is in western part of China, where most of the currently unused land is distributed, whereas, it is eastern part that accommodates over 90% of the country's population. If all fossil fuels are replaced by PV, long distance transmission will be required which is not preferred. Land constraints in China can be largely expected for a solar economy. Thus we could anticipate that the land challenge is a global issue towards a solar economy.

3.5 Conclusion

In this chapter, a systematic method for land requirement analysis in a solar economy is presented. By this method, the energy demand in a solar economy scenario is first estimated by considering each energy conversion step from primary energy to end uses in both fossil fuel scenario and solar economy scenario. In addition, intermittency of solar availability and energy storage efficiency are also taken into consideration. For land analysis, data of power output per unit land area are acquired from actual

PV parks. Meanwhile, land uses are classified in order to get the reasonable land area data for currently available land.

The land requirement analysis for the contiguous US shows that there will be 24 states that requires more than 11 W/m^2 power output from solar PV parks, which exceeds the upper limit of current PV parks, if 50% of the miscellaneous land and 5% of the urban land are used. More case studies indicate similar challenge. It will be difficult for currently available land to meet the energy needs using current solar park designs for the entire contiguous US and for nearly half of the individual states, which include well over half of the total US population.

Similar land requirement analysis for densely populated developed countries such as the UK and Germany also shows the difficulty for currently available lands to support a 100% solar economy. Therefore, barring radical improvements in agricultural output that could greatly reduce the land devoted to agriculture, the competition for land between energy and food seems inevitable, posing a major challenge to a future solar economy. Land use intensification is imperative to enable a solar powered future.

4. SUSTAINABLE CO-PRODUCTION OF FOOD AND SOLAR POWER TO RELAX LAND USE CONSTRAINTS

4.1 Introduction

As the global population approaches 10 billion by the mid-century [79], supplying all the needs of the human race from the Earth's limited land area will be the essential challenge of sustainability. In a highly populated "full Earth" [80], all available renewable energy resources will be used synergistically, while solar and wind energy will be dominant [17]. However, their power density, or rate of supplied energy per unit land area, is much more dilute than that of fossil fuels [6]. Hence, large tracts of land are required to harness solar or wind energy [53] [54]. Since transmitting energy over long distances will be expensive, risky and prone to significant transmission losses, local sustainability is greatly preferred [55]. While the availability of wind energy is highly geographically limited, solar resources are accessible in most of the populated regions around the world, usually with a higher power density than wind [24] [72]. Therefore, in Chapter 3, we evaluate the land feasibility of a 100% solar economy in the contiguous United States as an example, and find that it will be difficult for currently available land to meet the energy needs using current solar park designs for the entire contiguous United States and for nearly half of the individual states, which include well over half of the total US population. Barring radical improvements in agricultural output that could greatly reduce the land devoted to agriculture, the competition for land between energy and food seems inevitable, posing a major challenge to a future solar economy [4].

To address this issue, we propose the concept of the "aglectric" farm, where agricultural land (including cropland, grassland pasture and range in this study; Section 3.3.2) produces electricity without diminishing existing agricultural output. Both

wind turbines and photovoltaic (PV) panels can be used to generate electricity on agricultural land. While wind aglectric farming is already put into practice, the use of the current PV panels is known to have a negative impact on crop growth [81] [82] [83], mainly due to shadows. Previous researchers have proposed or tested several PV and food co-production ideas, but these systems either sacrifice agricultural production or are limited to several types of shadow-tolerant crops [84] [85] [86] [87]. For example, Fraunhofer ISE installed elevated south-facing bifacial solar panels and found yield losses of 18–19% for crops such as wheat, potatoes and celeriac growing underneath the PV array [88]. Since maintaining agricultural output (especially of major crops such as wheat, rice, soybean, and so on) is of high priority, existing PV modules and their installation practice will not enable the envisioned PV aglectric farm due to shadows. Meanwhile, wind plants require larger land area than PV parks [24] [72]. Exploring the feasibility of PV aglectric farms is essential towards a post-carbon era. Therefore, we propose several innovative PV systems using existing and new materials, innovative installation paradigms and module designs. Through extensive modelling of PV shadows throughout a day, we show that some of our designed PV systems could mitigate the loss of solar radiation while still maintaining substantial power output. Thus, it should be possible to design and install these PV systems on agricultural land to have significant power output without potentially diminishing agricultural production. We also show that PV aglectric farms alone will have the potential of realizing a 100% solar economy without land constraint. Together with regular PV parks and wind aglectric farms, PV aglectric farms will serve as an important option for a renewable future.

4.2 PV Systems for PV Aglectric Farms

The purpose of PV aglectric farming is engineered shadow management such that sufficient light is transmitted for equivalent crop yield while directing the remaining light for PV conversion. Shadows can be manipulated and managed through two

distinct strategies: (1) current PV materials such as polysilicon, cadmium telluride and so on, plus new panel installation methods and module designs; and (2) new PV materials and module designs for optimum PV aglectric farm performance. To allow the space for crop growth, farming equipment movement on croplands and livestock activities on pastures, these PV systems will generally have to be installed at an elevated height (4 m or higher) and possibly with increased row spaces compared with ground-mounted panels in regular PV parks. The installation might also help with reducing the shadow intensity on the ground.

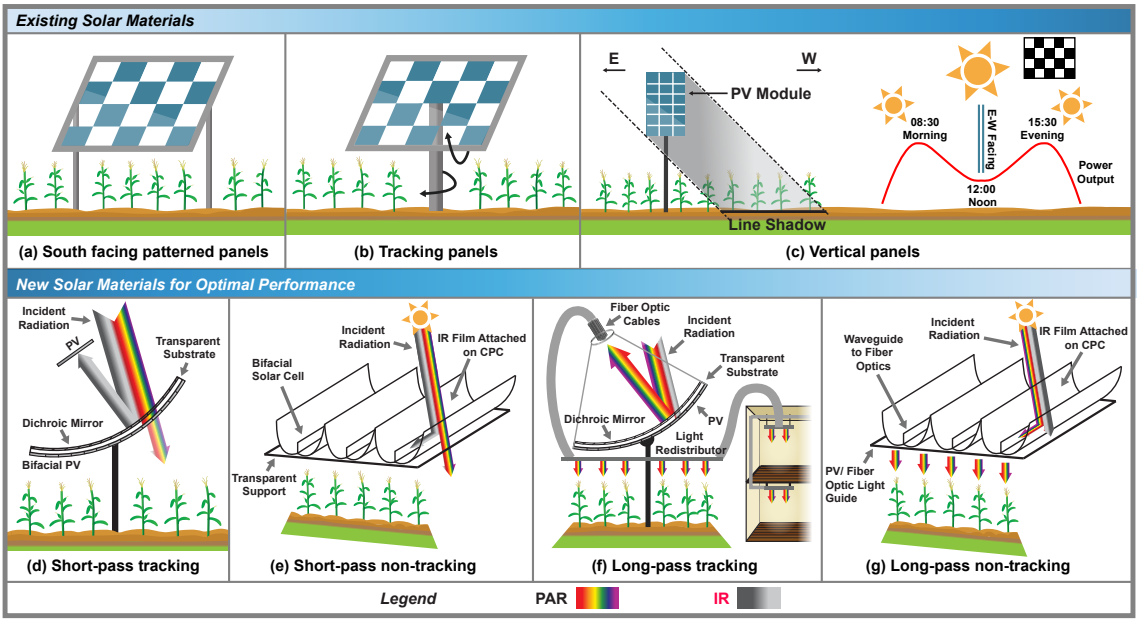

Fig. 4.1. PV systems for co-production of food and energy with farmland. Fixed south-facing patterned panels (a), tracking patterned panels (b) and bificial vertical panels (c) can be used with existing PV materials, while short-pass tracking (d), short-pass non-tracking (e), long-pass tracking (f) and long-pass non-tracking (g) would have optimum performance with band-gap materials tailored to the incident spectrum.

4.2.1 PV systems with current PV materials and technologies

First, we considered innovative module installation and designs for commercially available materials/PV modules. In Figure 4.1(a), we propose a PV module design with transparent areas between solar cells for possible fixed installation. The pattern can be easily accomplished with traditional "tiled" single-junction silicon panels. A light diffuser in the empty tiles helps distribute light beneath the panels. While various patterns could be used, a chequered pattern ensures that all crops affected by the panels' shadow receive essentially the same average illumination, and no individual plant is in intense shade for long. The percentage of filled (solar cells) versus unfilled (transparent) area could also be adjusted. In Figure 4.1(b), the use of a patterned PV module is applied to an east–west single-axis tracking configuration to further reduce the impact of shading. It can also be modified to become a dual-axis tracking configuration. Figure 4.1(c) utilizes vertical bifacial solar panels to capture sunlight [89]. North–south facing panels mainly capture diffuse light; however, they have the distinct advantage of allowing all direct radiation to be transmitted to the plants except for a thin line-shadow that moves throughout the day. These modules could be installed on axes that rotate slightly throughout the year, to keep the panels aligned with the Sun's path to minimize shading. A major benefit of this system is that during non-growing seasons, the panels could transition to a standard south-facing bifacial panel for increased power production during the winter months. Bifacial panels can increase power output by capturing albedo light from the rear side [90] [91]. Alternatively, when the bifacial panels are installed to face east–west, as shown to the right of Figure 4.1(c), a peak in electricity generation is realized in the morning and evening, capturing only diffuse light at noon. When facing east–west, these panels could also be patterned as shown in Figure 4.1(a) to further diffuse the shadow intensity.

4.2.2 New PV materials and module designs

Gençer et al [4] identified several solar spectrum-splitting systems to direct photosynthetically active region (PAR) photons to food production and long-wavelength photons to solar cells for electricity generation. These structures rely on concentrating troughs that are coated with well-studied dichroic materials or commercially available polymeric dichroic mirrors, to split the spectrum into the PAR and the infrared region [92] [93] [94] [95]. In the system in Figure 4.1(d), a parabolic trough with a short-pass dichroic film allows the PAR to transmit to the crops below, while concentrating the infrared light on a solar cell [4]. The system in Figure 4.1(e) uses a compound parabolic concentrator (CPC) with a short-pass dichroic film that allows the PAR through to the crops while directing a significant fraction of the incident direct infrared region to vertical bifacial cells at the centre of the CPC [92]. The CPC could have a transparent cover to keep dirt out, as well as a built-in, gravity-fed rain redistribution system. In the system shown in Figure 4.1(f), the PAR is reflected by a long-pass dichroic mirror attached to a fibre optic bundle, which allows for redistribution of light to the plants underneath, and potentially to vertical farms during winter months. Alternatively, during winter months when no food crops are grown, PV cells could replace the fibre optic bundles so that the light is still utilized. Figure 4.1(g) presents a system where a long-pass CPC is used to redirect the PAR to a central waveguide to redistribute light underneath, while the infrared spectrum transmits to the PV support underneath. Although they are not shown in Figure 4.1, heliostats with a short-pass dichroic mirror can also be used, and the reflected long-wavelength portion could be focused on appropriate solar cells or a thermal system for concentrating solar thermal power generation.

4.2.3 Impact of depriving plant of infrared radiation

The PAR of the solar spectrum is typically understood to be light in approximately the 350-750 nm range [96]. However, light outside this range also can have important

implications for crop growth. In our proposed PV systems in Figure 4.1(d)-(g) in section 4.2.2, infrared radiation (IR) has been deprived from plant underneath. IR has been shown to affect the growth of certain species of plants [97]. However, it is also clear that many plants can be grown with high success under illumination that is quite different than the natural solar spectrum. Recent vertical and urban farming techniques have shown excellent crop production in blue and red LED lighting [98], which suggests that it may be possible to deprive plant of significant portions of the solar spectrum with minimal impact to yields.

In addition, the PV systems in Figure 4.1(d)-(g) in the main text do not deprive all the IR from plant. These configurations only split the solar spectrum within the direct sunlight. Plant can still receive the IR in the diffuse radiation. On the other hand, the spacing between the PV installation also allows IR to reach the plant underneath.

4.3 Feasibility of PV Systems Based on Shadow Modelling

To understand the effects that solar panel array geometries have on nearby crop growth, and to check the feasibility of our selected PV systems (configurations in 4.1(a), (b)), we developed a simulation that predicts the loss in incident solar energy on the underlying crops due to shading by the panels. We define the variable "shadow depth" as the loss of incident solar energy compared with an open field; for example, if the solar irradiation at a location on a PV aglectric farm is 90% of that on an open field, the shadow depth is 10%. All configurations are elevated to 5 m to allow for navigation of agricultural equipment and to suppress the blocking of diffuse light. Both high row-spacing configurations (7.62 m) and lower row-spacing configurations (3.81 m) are simulated—the latter being representative of some existing regular PV parks [72].

Established crop growth models indicate that photosynthesis scales with the solar intensity I according to $aI/(1+bI)$, all other factors being equal. As a result, growth

is linearly proportional to intensity in low-light conditions but saturates under intense light. The intensity at which crossover between these two regimes occurs varies with the crop [99]. For instance, the photosynthetic rates of cotton and rice typically saturate at approximately 650 W/m^2 of solar irradiance, which is well below the average midday irradiance during the growing season for high-irradiance agricultural regions such as Texas and California [100] [101]. Based on this model, we predict that for many commercially relevant crops, regions of high shadow depth will have low crop yield, but low levels of homogeneous shadowing may have a negligible effect on certain crop yields. This is also consistent with experience, in that annual variations of solar energy delivered over the growing season generally do not cause crop failures.

Table 4.1 lists the average shadow depth, its standard deviation and the percentage of land with less than 25% of shadow depth for five different PV configurations we have simulated (simulation method in Appendix B). The standard deviation indicates the spatial homogeneity of the shadow on the ground. Figure 4.2 shows the spatially mapped shadow depth for selected cases in Table 4.1. The results in Table 4.1 and Figure 4.2 are based on the solar radiation in the South Plains region of Texas—a region with intermediate levels of diffuse light. Simulation results for other locations with low and high levels of diffuse light are listed in Appendix A. In Table 4.1, cases A and C represent current fixed south-facing and east–west tracking configurations in regular PV parks with low row spacing, respectively. Cases B and E utilize the proposed design in Figure 4.1(a), (b), respectively. An additional case D represents a continuous tracking panel with high row spacing.

The simulation result for case A shows that the average shadow depth is 35.2% and homogeneity is low (15% s.d.), and that only 41% of the land will be under <25% shadow depth (Table 4.1), which indicates that more than half of the land will be under intense shadow if a regular south-facing PV installation scheme is applied. In addition, "trenches" of high shadow depth (>40%) exist during the entire growing season in >20% of the plot area (case A; Figure 4.2). We expect that such deeply shadowed regions will experience minimal growth of many commercially relevant crops

Table 4.1.
Shadow depth and usable land for various PV aglectric configurations

	Configuration	Panel design	Row spacing (m)	Average shadow depth (%)	Shadow depth s.d. (%)	Land with less than 25% shadow depth (%)
A	South facing	Continuous	3.81	35.2	15.2	41.0
B	South facing	Checkered	3.81	17.6	7.6	74.7
C	East-west tracking	Continuous	3.81	31.5	0.6	0
D	East-west tracking	Continuous	7.62	21.4	0.6	100
E	East-west tracking	Checkered	7.62	11.5	1.1	100

Note: Cases A and C represent existing PV park configurations (fixed south facing and east–west tracking, respectively). Cases B and E utilize the proposed design in Figure 4.1(a), (b), respectively.

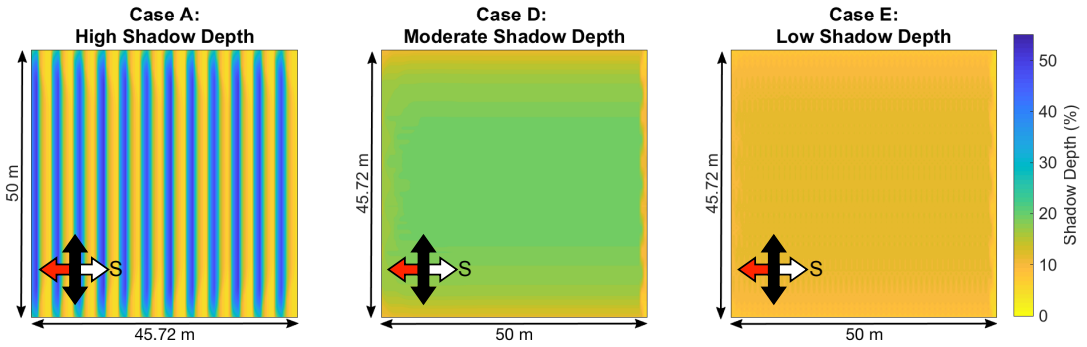

Fig. 4.2. Spatially mapped shadow depth for cases A, D and E from Table 4.1. Case A, representing an elevated south-facing fixed latitude-tilt PV park, shows regions of high shadow depth. Case D shows the advantage of using an east–west tracking system. Case E shows the advantages gained from implementing a chequered pattern on the panels.

(such as soybeans). The trenches of high shadow could be one potential explanation for the observed decline in crop yield reported by Fraunhofer ISE [88]. Case C, which represents continuous tracking panels with low row spacing, shows worse results, where no land will have shadow depth lower than 25% (Table 4.1). Cases A and C both illustrate that regular PV parks should not be directly applied for PV aglectric farms.

In case B, which is representative of the configuration in Figure 4.1(a), the land area with <25% shadow depth has increased to 74.7% and the average shadow depth has reduced to 17.6%, with a reduced standard deviation of 7.6% compared with case A. This shows the effect of the reducing shadow intensity and increasing homogeneity of the chequered design. Here, we do not consider the deployment of light diffusers in the empty tiles as stated in section 4.2.1; the checkered pattern with light diffusers will further improve the shadow distribution on the ground. From cases D and E, we can see that both continuous and checkered east–west tracking configurations with high row spacing (7.62 m) ensure that all land experiences a shadow depth <25%.

The average shadow depth is low and shadow homogeneity is high in both cases. Furthermore, Figure 4.2 cases D and E show that no "trenches" of high shadow depth exist. Therefore, the potential feasibility of our newly designed systems in Figure 4.1(a)(b) is proven.

4.4 Power Output of PV Aglectric Farms

First, we estimated the power density output from PV aglectric farms (Table 4.1), and from there we obtained the power output estimation for the systems in Figure 4.1(a)(b). For all of the cases in Table 4.1, the power output was calculated together with the shadow simulation. The simulation methods and parameters are explained in Appendix B. The simulation results are listed in Table 4.2. In Table 4.2, the power output numbers in the column "Simulated power output" are based on the solar irradiation data for the South Plains region of Texas on 1 June 2018, which are not the required yearly averages. However, we assume that the simulated power output ratio between various cases in Table 4.1 remains valid after averaging. From the cases for other locations (Indiana and California) shown in Appendix A Table A.1 and Table A.3, we can see that the simulated power output ratio between various cases in Table 4.1 remain valid for different locations. This is reasonable because the different power output for different cases at one location is only caused by the spatial arrangement of panels. A correction was made for these simulated results, and the correct power output numbers are listed in the column "Corrected power output". Case A is the most representative case of regular PV parks, and has a power output of 7-11 W/m^2. Therefore, the simulated power output of 11.8 W/m^2 should be corrected to 7-11 W/m^2 (where 7 and 11 W/m^2 are the lower and upper estimates, respectively). The simulated power output in case B through case E can be corrected by the same lower and upper estimate factors: 0.59 (7/11.8) and 0.93 (11/11.8), respectively.

Table 4.2.
Simulated and corrected power output for cases in Table 4.1

	Configuration	Panel design	Row spacing (m)	Simulated power output (W/m^2)	Corrected power output (W/m^2)
A	South facing	Continuous	3.81	11.8	7.00 - 11.00
B	South facing	Checkered	3.81	5.9	3.50 - 5.50
C	EW tracking	Continuous	3.81	15.1	8.96 - 14.08
D	EW tracking	Continuous	7.62	7.6	4.51 - 7.08
E	EW tracking	Checkered	7.62	3.8	2.25 - 3.54

Since cases B and E in Table 4.1 (and Appendix A Table A.1 through Table A.3) represent the PV configurations in Figure 4.1(a)(b), we obtain estimations of power output for Figure 4.1(a),(b) of 3.5–5.5 and 2.3–3.5 W/m^2, respectively.

For the PV system shown in Figure 4.1(c) that uses vertical bifacial panels facing east–west, the output is estimated using the model of Sun et al. and the Purdue University Bifacial Module Calculator [89] [90]. Using this model for several representative meteorological conditions yields estimates in the range of 4.1–6.0 W/m^2. The north–south-facing, non-checkered vertical bifacial configuration of Figure 4.1(c) uses the diffusive part of the solar insolation only. We assume the panels are orientated at all times such that they receive no direct insolation. In this scenario, we can use the model of Khan et al. [91] to estimate the power output, except that direct insolation is only absorbed indirectly via albedo light. Depending on meteorological conditions, we estimate a power output of 4.9–6.7 W/m^2. Further details on the power modelling for bifacial PV systems can be found in Appendix C.

Now, we consider the PV systems from Figure 4.1(d)(e) that require new PV materials for optimum performance. For example, Gençer et al. [4] calculated maximum recoverable power from a single-junction solar cell to be 161 W/m^2 (note that this

number is based on cell area instead of land area) for a direct solar insolation of 1000 W/m^2 in the short-pass tracking configuration shown in Figure 4.1(d), with the PAR portion terminating at a wavelength of 750 nm and a concentration factor of 20. The corresponding maximum recoverable power from a conventional single-junction solar cell with the entire incident solar spectrum is ∼310 W/m^2. If we assume a PV installation of Figure 4.1(d) on a PV aglectric farm with an actual to maximum theoretical power output ratio of 0.52 (160/310), we would expect a power output of ∼3.6–5.7 W/m^2 (based on 7–11 W/m^2). The power output estimation for the PV system in Figure 4.1(e) follows the same method.

Results for estimated power density output from PV aglectric farms with the configurations shown in Figure 4.1(a)-(e) are summarized in Table 4.3. Note that for the systems in Figure 4.1(a)(b), which use currently available PV materials with a new panel design or installation method, the power output based on the active PV cell area is similar to that from the conventional PV panels, and the reduced power output based on unit land area, as shown in Table 4.3, is not due to the lower efficiencies of the PV cell itself. Instead, the reduction in power output density should be attributed to the "sparse" installation (checkered design, higher row spacing, and so on).

4.5 Land Requirement for PV Aglectric Farms

Based on the power output numbers in Table 4.3, agricultural land requirement for PV aglectric farms can be calculated for the states where miscellaneous and urban land are insufficient (Table 3.1). In one case, the power output from regular PV parks is assumed to be 7 W/m^2 and the power output from PV aglectric farms is 3.7 W/m^2, which is the average of the lower estimated values shown in Table 4.3. In a more optimistic case, the power output from regular PV parks is assumed to be 11 W/m^2 and the power output from PV aglectric farms is 5.5 W/m^2. For both cases, 50% of the miscellaneous land and 15% of the urban land would be used for regular PV parks,

Table 4.3.
Summary of PV system characteristics and estimated PV aglectric farm power output

System (from Fig. 4.1)	Spectrum regions transmitted to plants in shaded region				Shade duration	Power estimate (W/m^2)	Non-growing season configuration
	Diffuse PAR	Direct PAR	Diffuse IR	Direct IR			
a	Yes	Yes	Yes	Yes	Constant	3.5 - 5.5	None
b	Yes	Yes	Yes	Yes	Mobile	2.3 - 3.5	None
c (NS facing)	Yes	Yes	Yes	Yes	Negligible shade	4.9 - 6.7	Traditional bifacial
c (EW facing)	Yes	Yes	Yes	Yes	Mobile	4.1 - 6.0	Traditional bifacial
d	Yes	Yes	No	No	Mobile	3.6 - 5.7	None
e	Yes	Yes	No	No	Constant	3.6 - 5.7	None
f	No	Yes	No	No	Mobile	-	Concentrating PV system
g	No	Yes	No	No	Constant	-	Concentrating PV system

and the remaining power requirement would be fulfilled by PV aglectric farms. Figure 4.3(a) and (b), respectively, shows the percentage of agricultural land required to be converted to PV aglectric farms under these two cases. We observe that the majority

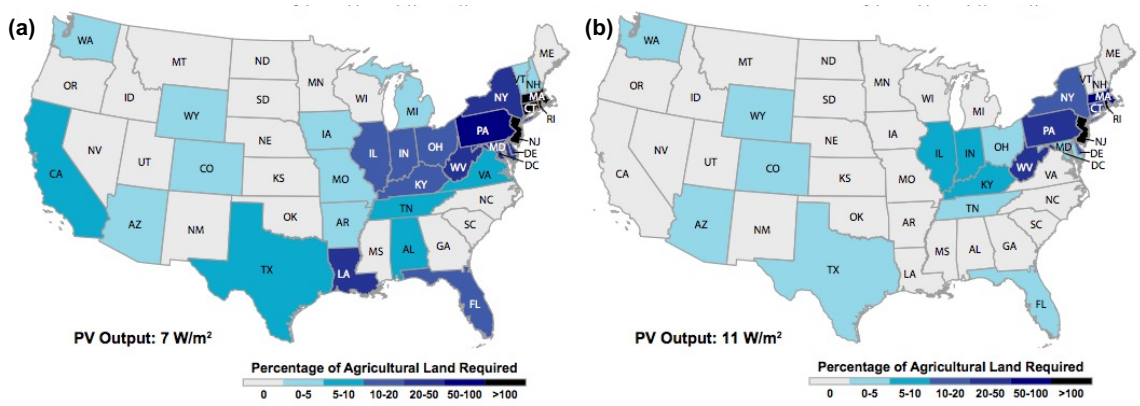

Fig. 4.3. Percentages of agricultural land required to meet states' energy needs. Cases shown are for a PV power output of 7 W/m^2 on regular PV parks (the current average PV park output) and 3.7 W/m^2 over agricultural land (a), and for a PV power output of 11 W/m^2 on regular PV parks (the upper end of current PV park output) and 5.5 W/m^2 over agricultural land (b).

of states require only a small percentage of the agricultural land to satisfy their power needs. This implies that the lower power density of PV aglectric farms compared with regular PV parks is acceptable for most states, since most states have sufficiently large agricultural land areas. Furthermore, since a relatively low power output from PV aglectric farms is tolerable, row spacing between PV panels can be further enlarged to reduce the shadow intensity on the ground. However, there are states that face the challenge of land constraints in both cases, such as Massachusetts, New Jersey and Rhode Island. These states are all densely populated, highly urbanized states with a small percentage of agricultural land. For these states, PV aglectric farming alone cannot enable a 100% localized renewable economy. Importing electricity from adjacent states (or regions) and using other renewable energy such as wind could help resolve this challenge.

While we focus on a bookend case for the contiguous United States, our methods and results also show how PV aglectric farms could be useful across most countries and regions experiencing land constraints in sustainable food and energy production. Furthermore, the concept of aglectric farming can also be applied to multiple renewable energy resources, such as wind energy. Given that PV aglectric farming alone has the potential of enabling a 100% solar economy for most states in the contiguous United States, synergistic power production from multiple renewable energy resources on agricultural land will have a huge impact in realizing a future renewable energy roadmap.

4.6 Aglectric Farms with Wind Energy

In previous sections, we proposed a solution to relax the land constraint of solar economy by incorporating PV systems into agricultural land without hurting the food production. However, as wind energy will definitely provide a complimentary solution to the renewable future and aglectric farms with wind energy have already been put into practice, one might question the necessity of developing aglectric farms with PV systems. In this section, we briefly discuss the need of developing aglectric farms with PV systems.

4.6.1 Power output from aglectric farms installed with wind turbines

For the purpose of this paper, we take the wind plant land requirement data in Ref. [24]. More than 90% of current wind plants are constructed on land which can be categorized as agricultural land as defined in this work. Therefore, the power output density of current wind plants can be representative of power output density of wind aglectric farms. Current wind plants have capacity density (capacity per unit area) of 1 W/m^2 to 11.2 W/m^2, with an average of $\sim$3 W/m^2. Note that $\sim$3 W/m^2 refers to the capacity of a wind plant instead of actual generation. Considering the intermittency of the availability of wind energy, the actual power generation per unit

area is much smaller. The capacity factor for wind plants in the US varies from ∼0.32 to ∼0.37 in recent years [102]. Therefore, the actual power output density from wind plants is ∼1 W/m^2. Comparing the power output densities from current wind plants, current PV parks and the projected power output from PV aglectric farms, we can see that the power output from both PV parks and PV aglectric farms are higher than that from wind aglectric farms.

4.6.2 Availability of wind energy

Areas with annual average wind speeds around 6.5 meters per second and greater at an 80-m height are generally considered to have a wind resource suitable for wind development [103]. From Figure 4.4, we can see that suitable wind development sites are mostly located in the Midwest and Southwest region of the US. And currently

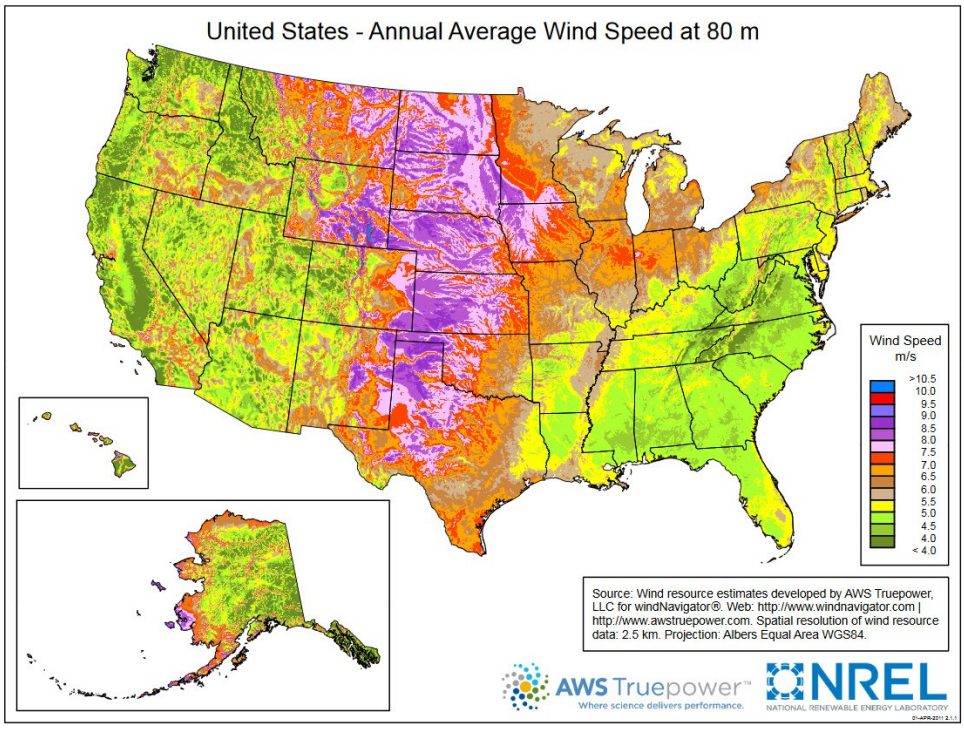

Fig. 4.4. U.S. Average Annual Wind Speed at 80 Meters, from Ref. [103]

wind plants are all built in the area with relatively high wind speeds. Wind plants in area without rich wind resource, such as California (average capacity factor is $\sim$0.27), usually operate at lower capacity factors than wind plants in area with more accessibility to wind resource, such as Texas (average capacity factor is $\sim$0.36) [104]. Places such as the Southeast region of the US are not suitable to develop large-scale wind energy. Since wind energy is not available everywhere, investigating the solar economy as a bookend case is justified.

4.6.3 Necessity of developing PV aglectric farms

Since current wind plants have lower power output density than current solar parks, either wind or solar energy alone cannot meet the energy requirement for most of the US states without using agricultural land. Therefore, agricultural land must be included for power generation in a renewable future.

(1) There are states where wind energy is not available for utility scale power generation. PV aglectric farms are necessary for these states. Most of these states are located in the southeastern part of the US, such as Florida, Georgia, Mississippi, Alabama, Louisiana, Arkansas, North Carolina, South Carolina, Tennessee, Virginia, West Virginia, Kentucky, etc. From Figure 3.3 (a) and (b) in Chapter 3, we can see that the power requirement density for these states is generally high and a lot of these states demand aglectric farms. Therefore, PV aglectric farms generating power from solar energy are necessary for these states.

(2) In some states, wind energy is available but not rich. Wind aglectric farms alone cannot meet all the power demand. Such examples include states in the northeastern region of the US, and Indiana and Ohio might also belong to this category. PV aglectric farms are necessary in these regions. For example, in states such as Massachusetts and New Jersey, solar energy cannot meet the power demand even with PV aglectric farms. Since the wind aglectric farms have lower power output, wind aglectric farms alone cannot help, either. In this case, PV panels and wind tur-

bines can be installed on agricultural land together to enhance power production. For states of Indiana and Ohio, if only wind aglectric farm is used to meet all the power demand, the power output density requirement is $\sim$1 W/m^2. Considering that wind energy is only available in northern Indiana or western Ohio, it is difficult for wind plants alone to meet this demand. And if we use miscellaneous and urban land for PV parks and agricultural land for wind plants, similar as the case shown in Figure 4.3, wind aglectric farms require $\sim$60% of the agricultural land in these two states. It will still struggle considering the availability of wind resource. Therefore, PV aglectric farms will still be necessary. Furthermore, for both Indiana and Ohio, PV aglectric farms alone can meet the energy demand. With wind energy available as a partial solution, PV and wind aglectric farms can be complementary to each other.

(3) In the other regions of the US, wind resources are relatively rich in potential and can provide a solution for a renewable future. In most of these states, land is also not constraint for solar energy. In these states, it is more flexible to choose wind or solar energy and these two types of renewable energy are likely to be complementary to each other to build an optimized mix with regard to grid operation, storage, environmental impact, etc.

In summary, with wind energy a partial solution to a renewable future, investigating PV aglectric farms is still necessary considering the availability of wind resources and the power output density of wind plants. With PV aglectric farms, more options for the mixed renewables are available. It can also be synergistic with other renewable resources.

4.7 Exploring Synergy between Wind and PV Aglectric Farms

As discussed in the section above, since wind aglectric farms are already being used in certain parts of the United States, it is worthwhile to explore the synergy between PV and wind aglectric farms. The actual power output density from wind aglectric farms of $\sim$1 W/m^2 is lower than our estimated power density of 2.3–6.7 W/m^2 from

the PV aglectric farms. Also, the availability of wind resource is geographically restricted. We can make the following two observations.

First, considering the case in the previous section where the power density from PV aglectric farms is 3.7 W/m^2, for the states where PV aglectric farms require less than ∼27% of agricultural land, wind aglectric farms with a power density of 1 W/m^2 can also meet the power demand. In such a scenario, wind aglectric farms could cover up to 100% of the available agricultural land area and could be used interchangeably with PV aglectric farms. For regions that are relatively rich in wind resource, there is a choice between wind and PV aglectric farms to solve the land constraint. Examples include the states of Wyoming, Colorado and Texas, where wind and solar could be used in any proportion. However, for states where wind resources are limited, even when PV aglectric farms require less than ∼27% of the agricultural land area, it will be essential to deploy PV panels on agricultural land. Such examples include Kentucky, Tennessee, Alabama, Florida and Virginia.

Second, for states where >27% of the agricultural land area is need for PV aglectric farms, wind aglectric farms alone will be unable to meet the entire demand of energy. A synergy between the two aglectric farms that cannot be ignored stems from the fact that wind energy can also be available during periods when solar energy is not. Furthermore, it may be possible to install both wind turbines and PV panels simultaneously on an aglectric farm. This will impact not only the power output from an aglectric farm but its availability pattern during an average 24-h day. The availability pattern will influence energy storage and associated implications. Further study should account for these factors.

4.8 Aglectric Vision

In this work, we show that PV aglectric farming is a viable solution to relax the land constraint for a renewable future. PV aglectric farms, wind aglectric farms and regular PV parks will be used according to the local renewable resource and land

availability. Besides removing the land constraint, additional benefits of aglectric farms (PV, wind, and even other renewables) are anticipated. For most non-tropical countries, agricultural land is used only for the growing season, but aglectric farms will allow agricultural land to be productive all year (by adding electricity production beyond the growing season), potentially stimulating the economy of rural farming communities by possibly increasing incomes for aglectric farm adopters.

Aglectric farming could also enable a new food, energy and water nexus in which the electricity generated on farms is utilized locally for water management, fertilizer production/recovery and bio-based chemical production. The envisioned aglectric farms will enable a "micro-grid" system interacting with a much larger-scale economic system, including the adjoining urban centres, and finally at the state and national levels. This will enable a renewable economy for a future "full Earth" scenario.

5. EFFICIENT HYDROGEN PRODUCTION FROM SOLAR THERMAL ENERGY VIA HIGH TEMPERATURE WATER ELECTROLYSIS

5.1 Introduction

For a sustainable economy that will be powered mainly by renewable energy, especially solar energy due to its abundance and vast availability, hydrogen can serve as a key building block connecting energy resources and end use demands (Figure 1.1) [7]. First, hydrogen can serve as a secondary energy carrier in a renewable economy [105] [106]. For the transportation sector, hydrogen fuel cell vehicle remains an active research area in auto industry and is one of the solutions towards carbon-free driving [107]. For the residential and commercial sectors, hydrogen can be used for heating in buildings [108]. In addition, since burning hydrogen does not generate CO_2 emission, it is an ideal fuel for a renewable future. Second, hydrogen is an important chemical feedstock in industry. For example, hydrogen is the feedstock for ammonia production, which will ultimately be used for fertilizer. If biomass is used as carbon source for chemical production, hydrogen is needed for bio-refinery [12] [18]. At the same time, due to the intermittent availability of renewable energy resources, hydrogen could play an important role is energy storage [5]. Therefore, as a solid building block towards our envisioned sustainable economy, it is essential to come up with efficient and sustainable methods for production of hydrogen.

Currently, most hydrogen production is from fossil fuels. About 96% of the hydrogen is produced from coal, oil and natural gas [109]. The production of hydrogen from fossil fuels include steam reforming, partial oxidation, pyrolysis, and so on [110]. However, due to the use of fossil fuels, these production methods will contribute to GHG emission, which is not preferred in a sustainable future. If no hydrocarbons

from fossil fuels are available as sources for hydrogen, the most straightforward hydrogen source in nature is water. Therefore, water splitting powered by renewable energy, especially solar energy, becomes the topic of this chapter.

Solar energy can harnessed as light, heat or electricity. From solar resources collected as light, hydrogen can be produced via photoelectrolysis or photobiolysis; for solar energy harnessed as electricity, hydrogen can be produced via water electrolysis; for solar energy harnessed as heat, hydrogren can be produced by thermolysis or thermochemical cycles [111]. Among all of these solar hydrogen production technilogies, solar themal hydrogen production is promising for its potential for large-scale applications and high energy conversion efficiency [112]. This chapter will focus on the high temperature water electrolysis powered by electricity generated from solar thermal energy.

At the beginning of 19^{th} century, the high temperature electrolyte ZrO_2 with 15% Y_2O_3 was developed by Nernst, which then became the basis for solid oxide electrolysis cell (SOEC). In 1969, Spacil and Tedmon raised the concept of high temperature electrolysis (HTE) of water and provided detailed thermodynamic analysis, cell characteristics, as well as material properties and fabrication [113] [114]. In 1980s, the HOT ELLY project in Germany prompted the development of steam electrolysis by SOEC in multiple scales [115] [116] [117] [118]: single cells have been operated during long-term tests with 100% Faraday efficiency; concepts for integrated modular electrolysis units have been developed and successfully tested [115]; process integration with high temperature reactor has been designed and corresponding efficiencies have been calculated [116]; a 3.5 MW pilot plant for vapor HTE has been designed [118] and further economic analysis and applications have been given [115] [116] [117] [118]. The technology has triggerd intense research on HTE for hydrogen production since then.

5.2 High Temperature Electrolysis and Solid Oxide Electrolysis Cell

5.2.1 SOEC basics

A solid oxide electrolysis cell is constituted of a cathode, an anode and an electrolyte in between, as shown in Figure 5.1. In an SOEC, water, as the reactant, is supplied to the cathode side of the cell in the form of steam. When electricity is supplied to the cathode, H_2O is reduced to hydrogen and oxygen ions O^{2-}. Oxygen ions are transported to the anode side through the solid electrolyte. Oxygen ions are oxided at the anode side to form oxygen. Therefore, H_2 and O_2 are produced from the cathode and anode side, respectively. Electrochemical reactions in an SOEC is summarized in Table 5.1.

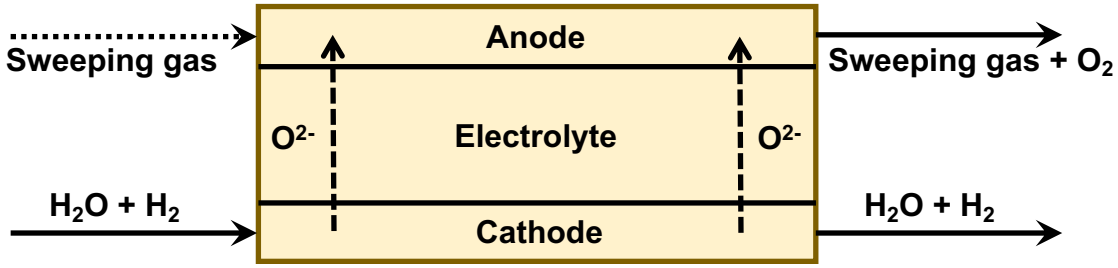

Fig. 5.1. Schematic of an SOEC for water splitting

Apart from steam, a small amount of hydrogen produced from the cathode is recycle to re-enter the cathode, as shown in Figure 5.1. Hydrogen here is used to stabilize the cathode and to prevent the oxidation of cathode material. For the anode, a sweeping gas is usually injected to sweep out the produced oxygen. For the purpose of producing hydrogen, air is usually used as the sweeping gas.

Table 5.1.
Electrochemical reactions within an SOEC for water splitting

Cathode reaction	$H_2O + 2e^- \rightarrow H_2 + O^{2-}$
Anode reaction	$O^{2-} \rightarrow \frac{1}{2}O_2 + 2e^-$
Overall reaction	$H_2O \rightarrow H_2 + \frac{1}{2}O_2$

5.2.2 Thermodynamics of high temperature water electrolysis

The total energy demand for an electrolysis process is equal to the change of enthalpy (ΔH), which can be divided into two parts, electrical energy (ΔG) and thermal energy ($T\Delta S$):

$$\Delta H = \Delta G + T\Delta S \tag{5.1}$$

where ΔH represents the change of enthalpy and indicates the total energy demnad; ΔG represents the change of the Gibbs free energy and indicates the electrial energy demand; T represents the temperature, ΔS represents the change of entropy, and $T\Delta S$ indicates the required heat supply.

When electrical current passes though electrodes, overpotentials will be generated and to compensate for the overpotentials, voltage higher than the electromotive force needs to be supplied. Joule heat will be generated from electrodes due to the overpotentials. The thermal energy required can be all or partially supplied by the Joule heat. When the Joule heat produced just equals to the required thermal energy, the SOEC is operated under thermoneutral mode, where the applied potential, called thermoneutral potential, can be calculated as

$$E_f = \frac{\Delta H}{nF} \tag{5.2}$$

where n is the number of electrons evolved in the reaction and F is the Faraday constant. At typical operation temperature of 900-1000 °C, the thermoneutral potential is around 1.29 V. Under thermoneutral operation, the produced gases leave the cell at the temperature of the incoming steam. If we operate below the thermoneutral

voltage, which is called endothermic mode, total electrical energy provided is less than the total energy demand. Under this mode, extra heat will be provided to maintain the temperature of the cell. Overall electrical efficiency here is higher than that for a thermoneutral mode. On the contrary, if the applied potential is higher than the thermoneutral potential, the SOEC is under exothermic mode and electrical efficiency is reduced because of the increased electrical energy input.

5.2.3 Benefits of high temperature electrolysis

One of the benefits of high temperature electrolysis, compared with low temperature ones, is that overpotentials at electrodes will be reduced at higher temperature. Therefore, the extra electricity input to compensate for the overpotentials can be reduced.

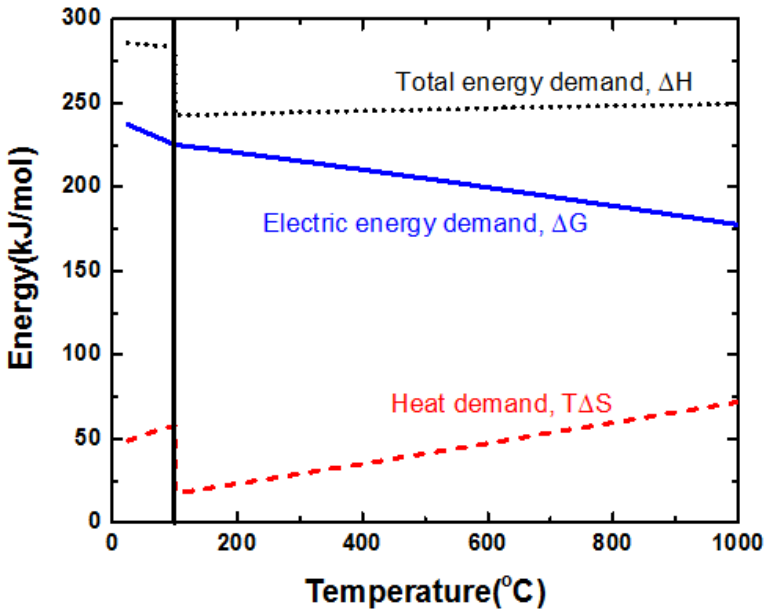

Fig. 5.2. ΔH, ΔG and $T\Delta S$ of water splitting reaction versus temperature

From Figure 5.2, we can see that the required electricity (ΔG) decreases with increased temperature. Therefore, operating electrolysis at higher temperature requires less electricity. As electricity is a secondary energy which is usually more expensive than heat, lower electricity demand is preferred. Since the system is operated at high temperature, heat can be acquired from power generation system, which enables process integration. Solar thermal energy is collected at high temperature, and it provides the opportunity for integration of high temperature electrolysis and solar thermal power generation.

5.3 Literature Review of Process Design, Modeling and Integration for Hydrogen Production Processes by High Temperature Electrolysis

In the HOT ELLY project, the first process design for high temperature electrolysis module and its combination with other heat source were come up with by Doenitz et al. The concepts included heat recovery from the produced gases and integration with nuclear power cycle by maintaining both electrical and thermal energy from the cycle [116]. Different process designs for both standalone high temperature electrolysis and synergy with other energy sources are developed rapidly recently. Sigurvinsson et al analyzed the process and economics of coupling HTE with geothermal energy [119]. Toklu et al reported the optimum operating conditions when HTE is combined with industrial waste heat from flue gas [120]. Manage et al provided detailed simulation for a system coupling HTE and coal-fired power plant, from the cell level to the system level [121]. Several research groups have worked on integration of HTE and nuclear power plant, which utilizes the power to supply the electrolyser and the high temperature reactor to supply heat. Typically the overall efficiency of hydrogen production is over 50% in the published papers [122] [123] [124].

Detailed modeling for SOEC is reported in multiple literatures. Im-orb et al proposed a detailed flowsheet-based modeling method and provided energy and exergy analysis based on the simulation. Modeling results show that at 1273 K and with

oxygen as sweeping gas, the highest energy and exergy efficiency can be achieved are 78.45% and 92.20%, respectively [125]. Menon et al proposed a numerical model considering the complex physico-chemical phenomena within an SOEC [126]. Ni et al developed a thermodynamic–electrochemical model to simulate the hydrogen production by an SOEC plant. Factors such as overpotential, waste heat recovery, etc. are taken into account [127] [128]. Liu et al performed a detailed thermodynamic analysis for the efficiency of hydrogen production by SOEC and identified the impact of electrical, electrolysis and thermal efficiencies on the overall SOEC efficieny [129]. Laurencin et al studied the impact of various operating conditions on the SOEC performance for hydrogen production, using a 2D multi-physic model [130].

Process design for hydrogen production via SOEC powered by solar thermal energy, and its integration with solar thermal power production are also studied by various researchers. Zhang et al reported configuration design and performance optimum analysis of a solar-driven HTE system for hydrogen production, which employs a solar concentrating beam splitting device. The device contains a PV receiver which converts a part of the incident solar energy to electricity and a solar collector converting the rest of solar energy into heat. The electricity and heat distribution can be adjusted according to SOEC's requirement [131]. Sanz-Bermejo et al analyzed several different configurations where SOEC is coupled with direct steam generation solar power plant. The best design among the proposed ones has been pointed out with least penalties to the solar power plant and highest overall hydrogen production efficiency, with an improvement of 5.8% [132]. Tolga Balta et al investigated a combined system consisting of a solar tower, Brayton cycle, Rankine cycle, organic Rankine cycle and HTE for hydrogen production. For the hydrogen production sections in the proposed process, the energy and exergy efficiencies are 87% and 88%, respectively [133]. AlZahrani and Dincer studied the integration of a solar tower powered powered plant, a thermal energy storage system and an SOEC for hydrogen production, and a 12% solar-to-hydrogen efficiency is achieved through simulation [134]. Seitz et al did a techno-economic analysis on an SOEC system with thermal energy

storage and with steam supplied by solar thermal energy [135]. Ozturk and Dincer performed a thermodynamic analysis for a multi-generation system which includes four sub-systems: Rankine cycle, absorption cooling and heating, organic Rankine cycle, and hydrogen production. The solar powered system has a exergy efficiency of 57.35%, which is higher than each of the standalone system [136].

In this chapter, we introduce a process design strategy for hydrogen production powered by solar thermal electricity. Modeling methods will be discussed in the next section; sun-to-H_2 efficiency and exergy efficiency will be analysed for different operating mode, operating conditions and different process configurations.

5.4 Modeling Approach

5.4.1 Overall process modeling approach

All the modeling is implemented in an integrated Aspen Plus and Matlab process design framework (Figure 5.3) proposed by Gençer et al [20]. Here the modeling and calculation results from both Aspen Plus and Matlab can be communicated via a Matlab core script. The use can provide initial conditions and parameters via Matlab and the running of all the modeling can be controled within the Matlab core script. The details of the two-way communication between Aspen Plus can be found in reference [20].

Figure 5.4 shows flowchart for the general modeling method. In our modeling approach, five separate modeling and calculation steps are employed: H_2 production process model, SOEC model, solar water power cycle, heat integration and efficiency calculation. The H_2 production process model simulates the complete process for hydrogen production, includeing the pre-treatment of the steam and sweeping gas, post-treatment of gases coming out of the SOEC and the recycle loop. Here the SOEC is treated as a black-box. The SOEC model implements the detailed simulation within the SOEC module, taking into account the eletrochemical phenomena such as overpotentials. The solar water power cycle is based on a Rankine cycle, where water

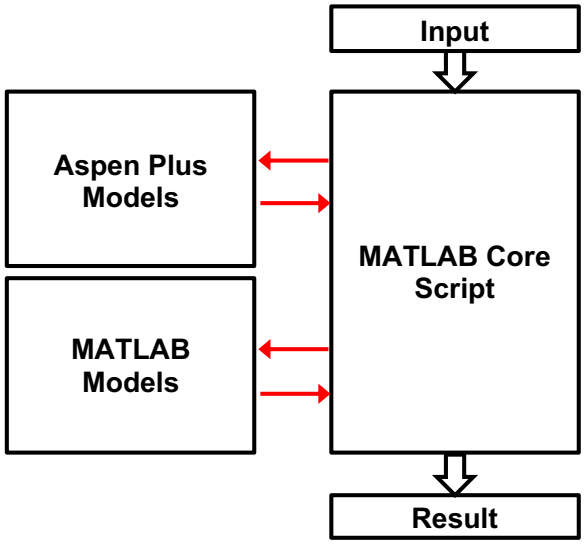

Fig. 5.3. Schematic for the integrated Aspen Plus and Matlab process design framework. All the models implemented in Aspen Plus and Matlab are communicated via a Matlab core script.

is heated to solar heat collection temperature for power generation, with reheating between stages [137]. Heat integration is implemented in Matlab using the data collected from the three models above, and a pinch analysis approach is employed. At the end, efficiencies are calculated using the modeling data.

At the beginning, initial parameters and modeling targets are put into the system, such as the solar heat collection temperature, SOEC operating conditions and operation mode, and desired H_2 production rate. These parameters or design objects are defined by the user. After initial processing, each of the five models are run sequentially. Required input information are acquired from the Matlab core script, which are user defined and/or imported from the simulation of the previous model. The results can then be exported from the system for user analysis. Details about each model's information communication are described in Appendix E.

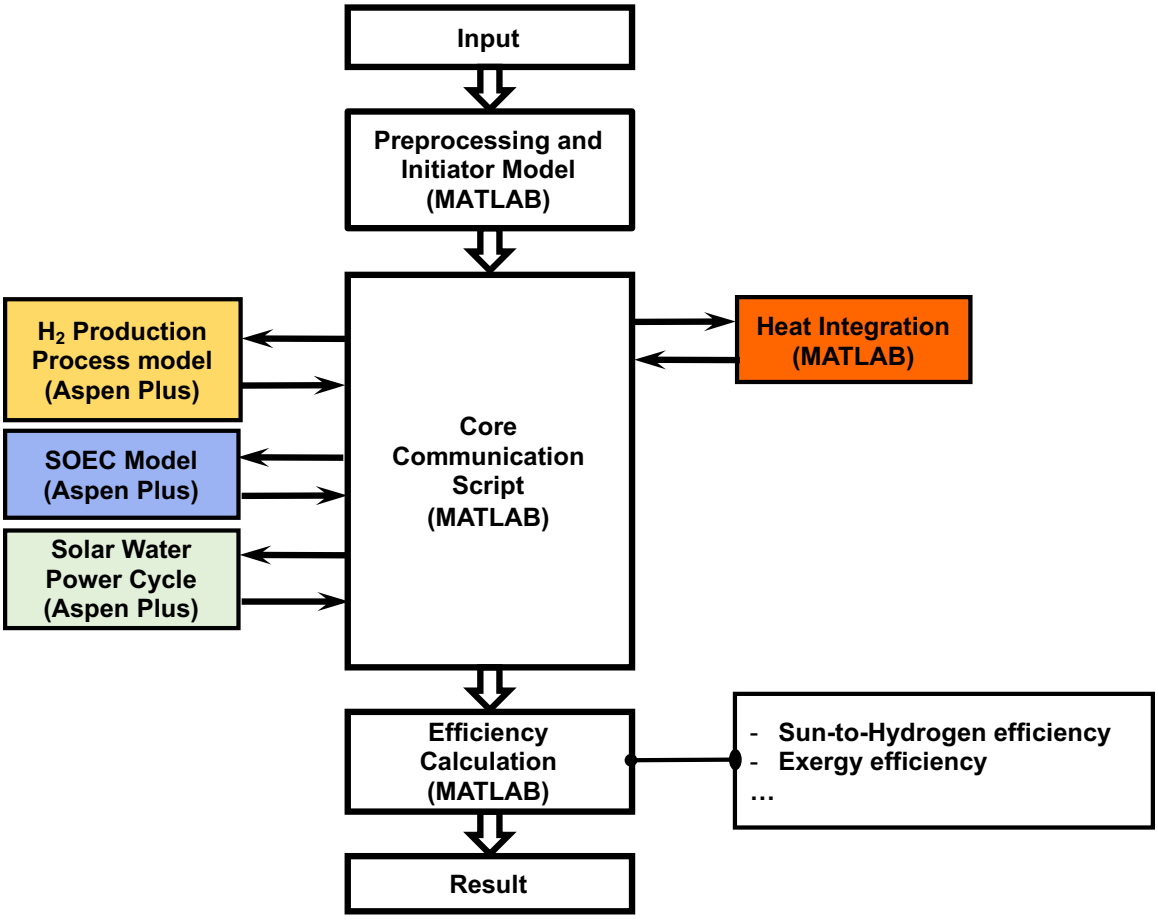

Fig. 5.4. General modeling method framework for the hydrogen production via high temperature electrolysis powered by solar thermal electricity

5.4.2 Modeling for the SOEC module

Modeling for the SOEC module is built in the Aspen Plus. As shown in Figure 5.5, the cathode of SOEC is modeled by a reactor (RStoic block in Aspen Plus) followed by a seperator (Sep in Aspen Plus). The conversion of H_2O to H_2 is specified in the reactor model, and produced O_2 is sent to the anode after separation. The anode is modeled by a stream mixer (Mixer in Aspen Plus). The flowsheet model can handle the basic information of inlet and outlet streams of the SOEC.

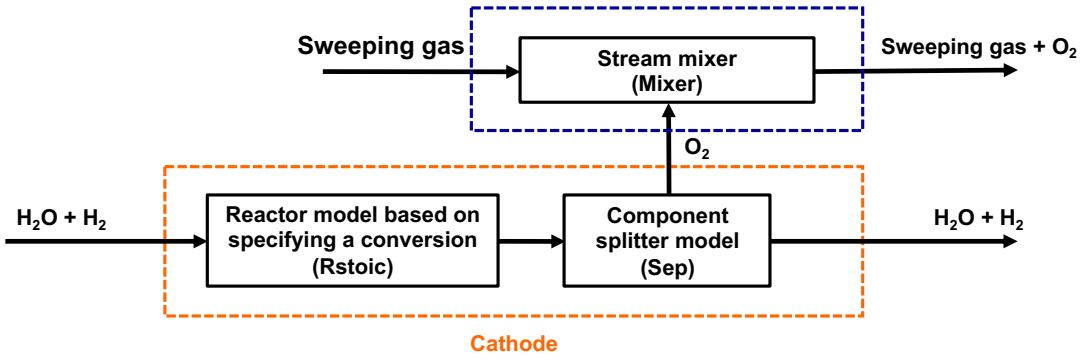

Fig. 5.5. Flowsheet model for the SOEC module in Aspen Plus

A calculator is then built within Aspen Plus to calculate the details within the SOEC. The goal of the detailed calculation is to acquired the electricity and heat demand. ΔH and ΔS of the SOEC can be calculated from the stream information acquired from the flowsheet modeling. And we can use these number to calculate the electricity demand of the cell.

$$\text{Electricity demand} = \Delta G = \Delta H - T\Delta S \tag{5.3}$$

The temperature T can also be acquired from the flowsheet simulation. And for the heat requirement, it is calculated by

$$Q = \Delta H - \Delta G - Q_{\text{overpotential}} \tag{5.4}$$

where $Q_{\text{overpotential}}$ is the Joule heat generated from the electrodes. For the calculation of the Joule heat, following equations are employed:

$$Q_{\text{overpotential}} = I_{\text{total}} V_{\text{overpotential}} \tag{5.5}$$

where I_{total} is the total current passing through the SOEC and $V_{\text{overpotential}}$ is the total overpotential.

$$I_{\text{total}} = 4FN_{\text{O}_2} \tag{5.6}$$

where F is the Farady constant and N_{O_2} is the mole flow of oxygen produced. Eletrical current density j needs to be calculated for the calculation of the overpotentials:

$$j = \frac{I_{\text{total}}}{A_{\text{cell,total}}} \tag{5.7}$$

where $A_{\text{cell,total}}$ is the total cross-area of the cell perpendicular to the current. Overpotentials are classified as activation overpotential, concentration overpotential and ohmic overpotential. Equations for calculation each of them are as following [127] [131]. Values for the parameters used in the following equations are also acquired from [127] and [131].

For activation overpotential,

$$V_{\text{act}} = \frac{2RT}{n_e F}\left[\sinh^{-1}\left(\frac{j}{2j_{0,a}}\right) + \sinh^{-1}\left(\frac{j}{2j_{0,c}}\right)\right] \tag{5.8}$$

where n_e is the number of transferred electrons and $n_e = 2$ in this reaction. $j_{0,a} = \gamma_a \exp\left(-\frac{E_{act,a}}{RT}\right)$ is the exchange current density of the anode, where γ_a is the pre-exponential factor and $E_{act,a}$ is the activation energy of the anode. Similarly, $j_{0,c} = \gamma_c \exp\left(-\frac{E_{act,c}}{RT}\right)$ is the exchange current density of the cathode, where γ_c is the pre-exponential factor and $E_{act,c}$ is the activation energy of the cathode.

For the concentration overpotential,

$$V_{\text{con}} = \frac{RT}{4F}\ln\left[\frac{\sqrt{(P_{O_2})^2 + jRT\mu L_a/2FB_g}}{P_{O_2}}\right] + \frac{RT}{2F}\ln\left(\frac{1 + jRTL_c/2FP_{H_2}D^{\text{eff}}_{H_2O}}{1 - jRTL_c/2FP_{H_2O}D^{\text{eff}}_{H_2O}}\right) \tag{5.9}$$

where μ is the dynamic viscosity of O_2, L_a is the thickness of the anode, L_c is the thicknesses of the cathode, B_g is the permeability, and $D^{\text{eff}}_{H_2O}$ refers to the effective diffusion coefficient of H_2O.

For the ohmic overpotential, which is caused by the resistance of the electrodes and the electrolyte. Here the contact resistance between difference parts of the cell is not considered.

$$V_{\text{ohmic}} = j\left(\frac{L_a}{\sigma_a} + \frac{L_c}{\sigma_c} + \frac{L_e}{\sigma_e}\right) \tag{5.10}$$

where L_c is the thicknesses of the eletrolyte, and σ_a, σ_c and σ_e are the conductivities of the anode, cathode and eletrolyte, respectively.

The total overpotential is calculated by adding up the three overpotentials above:

$$V_{\text{overpotential}} = V_{\text{act}} + V_{\text{con}} + V_{\text{ohmic}} \tag{5.11}$$

and from there we can calculate the eletricity and heat requirement for the SOEC.

5.4.3 Performance metrics

Two efficiencies are used as the metrics to evaluate the process. The first is the sun-to-H_2 efficiency, or STH_2 efficiency for short. It refers to the fraction of incident solar energy recovered in the form of hydrogen. It is calculated by the following equation:

$$\text{STH}_2 \text{ efficiency} = \frac{\text{LHV}_{\text{H}_2}}{Q_{\text{solar}}} \tag{5.12}$$

where LHV_{H_2} refers to the lower heating value of the hydrogen produced and Q_{solar} refers to the total incident solar energy. As we only know the energy input towards the process from the solar energy, the total incident solar energy is calculated by

$$Q_{\text{solar}} = \frac{Q_{\text{in}}}{\Sigma_{\text{opt}} \left(1 - \frac{\sigma T^4}{IC}\right)} \tag{5.13}$$

where Q_{in} is the heat supplied to the process. Σ_{opt} is the optical efficiency, which accounts for the optical losses of the solar concentrators. It is defined as the percentage of incident solar energy that is received by the solar collector. σ is the Stefan-Boltzmann constant, T is the solar heat collecting temperature, I is the intensity of the solar irradiation and C is the solar concentrating ratio [20].

The other performance metric is the exergy efficiency. The inlet exergy (EX_{in}) for the overall solar to hydrogen process is the exergy associated with solar energy; the only outlet exergy (EX_{in}) of our process is the exergy related to hydrogen, and is the sum of the chemical exergy and physical exergy. The overall exergy efficiency (from solar to hydrogen, not only for the process itself) is calculated by:

$$\eta_{\text{EX}} = \frac{EX_{\text{in}}}{EX_{\text{out}}} \tag{5.14}$$

5.5 Process Description, Integration and Modeling Results

5.5.1 Solar water power cycle

The solar water power cycle is a Rankine cycle driven by water heated by solar thermal energy, which is collected by a solar concentrator. The solar water power cycle used for power generation is this study is shown in Figure 5.6. After preheating, the water is heated by a solar heater using solar thermal energy. The the high temperature vapor goes through a high pressure turbine, a medium pressure turbine and a condensing turbine to generate power. According to the research by Gençer et al, inter-stage reheating can increase the sun-to-electricity efficiency of the cycle [137]. In this study, we employ one reheating step for the vapor coming out of the high pressure turbine. It is sent back to the solar heater and heated back to high temperature before entering the medium pressure turbine.

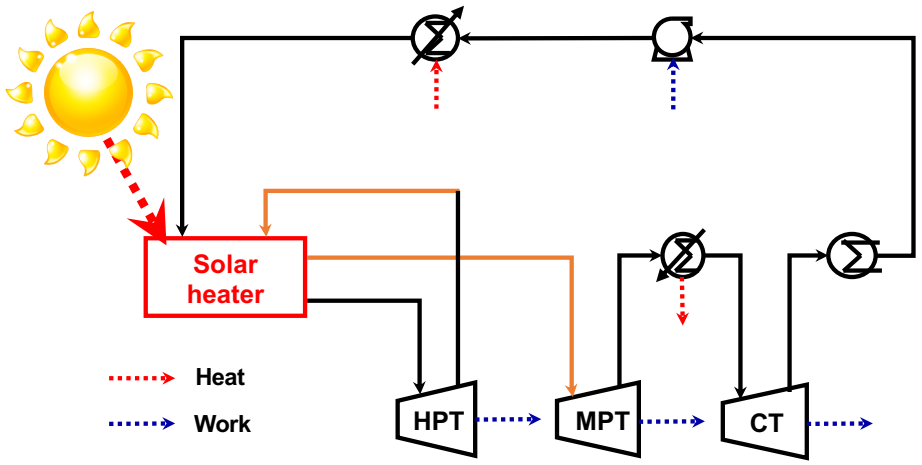

Fig. 5.6. The solar water power cycle with one inter-stage reheating. The vapor coming out of the high pressure turbine (indicated by the orange line) is sent back to the solar heater for reheating before entering the medium pressure turbine [137]. HPT: high pressure turbine; MPT: medium pressure turbine; CT: condensing turbine.

5.5.2 Hydrogen production process

Here we propose several designs for the hydrogen production process. Each process is integrated with the solar water power cycle. The first level of integration is the sharing of equipment, including solar heater, some of the turbines. The second level of the integration is heat and work integration. Heat exchangers are integrated within the two processes, and electricity generated by turbines from both processes can be used for the SOEC and pumps.

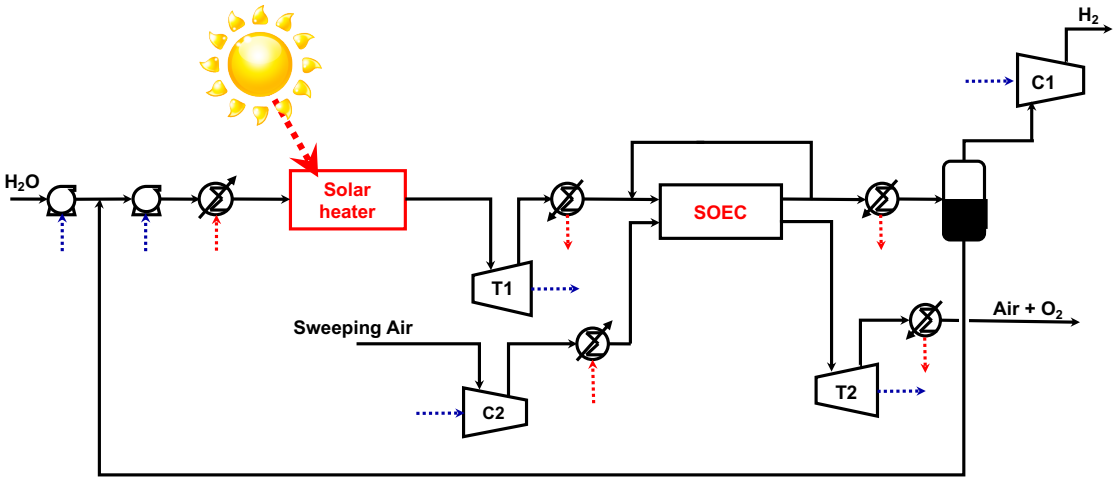

Fig. 5.7. Hydrogen production process via SOEC (thermoneutral mode). Before entering the SOEC, the water is pumped to high pressure and heated by solar thermal energy. T1: high pressure turbine; T2: medium pressure turbine; C1: H_2 compressor; C2: air compressor.

One of the process designs is shown in Figure 5.7. To integrate with the solar water power cycle, the feed water is pumped and preheated before entering the solar heater. The operating conditions of the pump and the pre-heater are the same as that in the solar water power cycle, so that these equipment can be shared. The solar heat collection temperature is usually higher than the SOEC operating temperature and the pressure is also higher. Therefore, a high pressure turbine is employed to recover the exergy of the high-temperature high-pressure water stream. The high pressure

turbine can also be shared with the high pressure turbine in the water power cycle. Then the steam is adjusted to the operating temperature of the SOEC before entering the cell. At the same time, sweeping gas (air in this study) is also compressed and heated to the operating pressure and temperature of the SOEC. The water stream enters the cathode of the SOEC and the sweeping gas enters the anode of the cell. At the exit of the cell, a part of the gas from the cathode is recycled to the combine with the inlet steam. A design specification is set here that the inlet gas of the cathode should contain 10% of H_2 to avoid the oxidation of the electrode. When the SOEC is operated at the thermoneutral mode, the exiting gas of the cathode can be directly recycled; however, when it is operated at the endothermic or exothermic mode, it should be heated or cooled (heat exchanger not shown in Figure 5.7. Then the gas exiting from the cathode is cooled to condense the water while hydrogen is separated and compressed as product. For the sweeping gas, it sweeps out the produced oxygen from the anode. The exiting gas is at high temperature and high pressure and a turbine is employed to recover the exergy.

For such as H_2 production process, when integrated with the solar water power cycle, the heat exchangers of both processes can be integrated. At the same time, power generated by turbines in both processes can be used not only by SOEC, but also by the pumps that required work input. Such integration is feasible because the operating conditions of the SOEC can be coupled with the solar water power cycle. For the integrated process, the system conditions (including operating conditions and specified H_2 production rate) and modeling results for both thermoneutral and endothermic mode are shown in Table 5.2.

From Table 5.2 we can see that when operated at endothermic mode, both the sun-to-hydrogen efficiency and the exergy efficiency are higher than that for the thermoneutral mode. Note that since under endothermic mode the temperature decreases along the SOEC, there could not be an "equal" temperature for comparison. However, from the thermodynamics, if we allow the endothermic operation of the SOEC rather than thermoneutral mode, the total electricity demand for the SOEC would

Table 5.2.
System conditions and simulation results for the integrated H_2 production (Figure 5.7) and solar water power generation process

	Thermoneutral mode	Endothermic mode
System conditions		
Solar heat collection temperature	1600 K	1600 K
SOEC operating temperature	1123.15 K	1273.15 – 1023.15 K
SOEC operating pressure	15.5 bar	15.5 bar
H_2 production rate	1000 kmol/h	1000 kmol/h
STH_2 efficiency	37.13%	39.14%
Exergy efficiency	62.06%	65.43%

be lower because no additional electricity is used to keep the temperature. On the other hand, this part of the heat, to keep the isothermal operation of the cell, comes from electricity that is generated from solar thermal energy. The energy goes through a path of solar-heat-electricity-heat. The efficiency is reduced when more conversion steps are employed. Therefore, when possible, a endothermic mode of the SOEC should be considered.

Figure 5.8 modifies the H_2 production process in Figure 5.7. Instead of entering a condenser for the separation of water and hydrogen, the gas from the cathode, which is still at the pressure of the SOEC, is sent back to the solar heater for re-heating. The reheated gas goes through another medium pressure turbine for power generation before the water-hydrogen separation.

Figure 5.9 shows a design with double SOEC modules. Here the steam and hydrogen mixture from the cathod of the first SOEC is reheated by the solar heater. After passing through a turbine where its exergy is recovered, it enters a second-stage SOEC for further electrolysis. The sweeping gas and oxygen from the fist SOEC is also expanded before entering the second electrolysis cell.

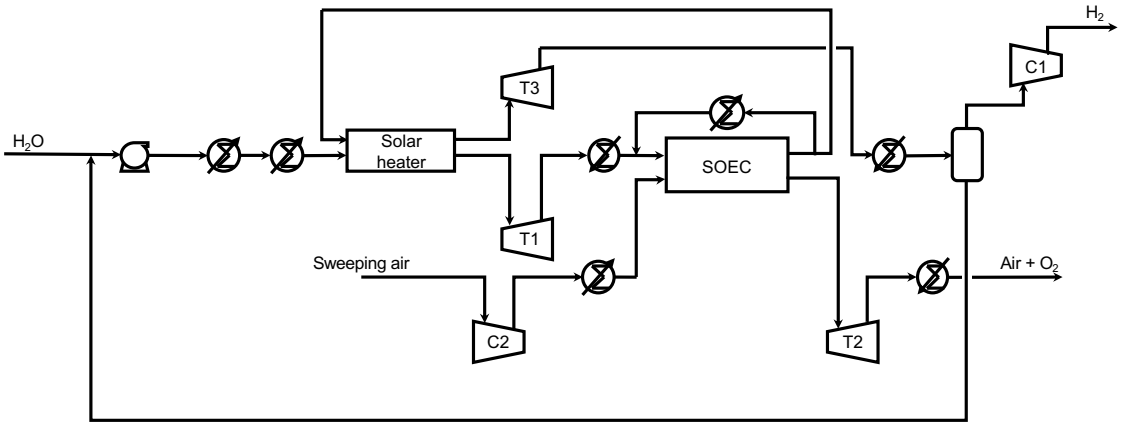

Fig. 5.8. Hydrogen production process via SOEC. The gas coming out of the cathode is reheated for power generation. T1: high pressure turbine; T2 and T3: medium pressure turbines; C1: H_2 compressor; C2: air compressor.

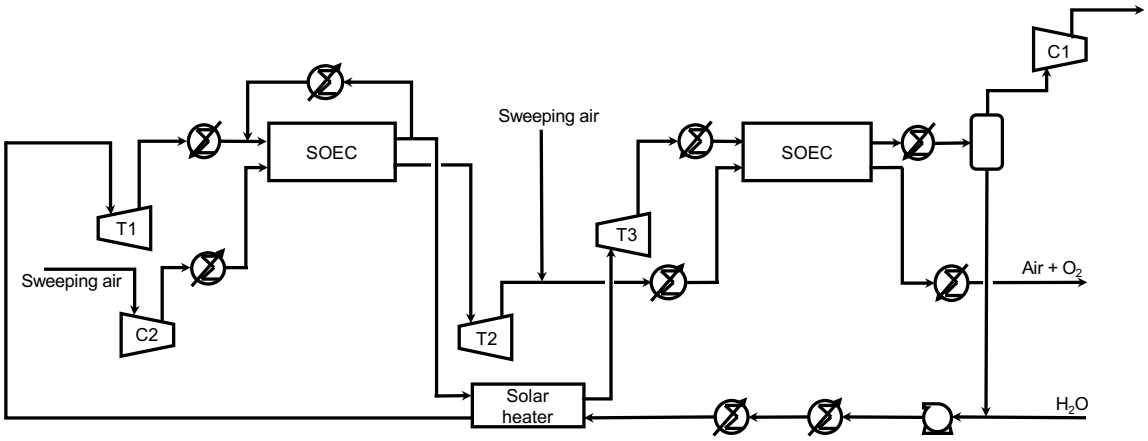

Fig. 5.9. Hydrogen production process via double SOEC modules. The fist SOEC is operated at higher pressure and the second SOEC is operated at low pressure. T1: high pressure turbine; T2 and T3: medium pressure turbines; C1: H_2 compressor; C2: air compressor.

Figure 5.10 shows another hydrogen production process design, where the recycled water is reheated and goes through a medium pressure turbine and a condensing

turbine for power generation before recycled. Here the turbines T1, T3 and T4 in Figure 5.10 can all be shared with the high pressure, medium pressure and condensing turbine in the solar water power cycle, respectively. The design aims at further recovering the exergy and more integration between the hydrogen production process and the solar water power cycle.

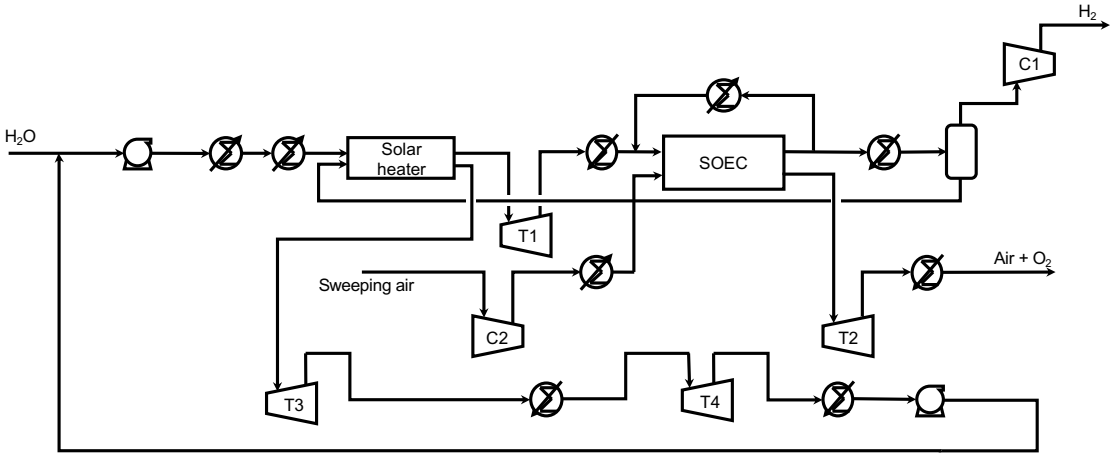

Fig. 5.10. Hydrogen production process via SOEC. The water collected from the water-hydrogen separator is reheated for power production. T1: high pressure turbine; T2 and T3: medium pressure turbines; T4: condensing turbine; C1: H_2 compressor; C2: air compressor.

Processes in Figure 5.8 through 5.10 are modeled in the integrated Aspen/Matlab platform and the results are listed in Table 5.3. Note that the SOEC for all these processes are operated at endothermic mode. The sun-to-hydrogen efficiencies and exergy efficiencies for all the processes in Figure 5.8 through 5.10 are lower than that for the process in Figure 5.7. For the same hydrogen production rate and hydrogen output conditions, the energy contained in the produced hydrogen, as well as the exergy coming of the system, remains the same. The lower efficiencies indicate that for the processes that involve more reheating steps, the input solar energy is higher and thus the inlet exergy of the system is higher. The power produced by the

additional turbines within the hydrogen production processes is generated at lower energy and exergy efficiencies compared with the turbines in the solar water power cycle. Therefore, for the purpose of hydrogen production, it is unnecessary to generate more electricity from the streams within the hydrogen production processes by adding reheating steps. Instead, the solar water power cycle can produce power at higher efficiencies. In addition, the process can be kept simple by employing the design in Figure 5.7.

Table 5.3.
System conditions and simulation results for the integrated H_2 production (Figure 5.8 to 5.10) and solar water power generation processes

	Figure 5.8	Figure 5.9	Figure 5.10
System conditions			
Solar heat collection temperature		1600 K	
SOEC operating temperature		1273.15 – 1023.15 K	
SOEC operating pressure		15.5 bar*	
H_2 production rate		1000 kmol/h	
STH_2 efficiency	32.60%	36.96%	37.85%
Exergy efficiency	54.50%	61.79%	63.28%

*Note: For the process in Figure 5.9, the first SOEC is operated at 15.5 bar and the second SOEC is operated at 1 bar.

5.6 Conclusions

This chapter presents the modeling for an integrated hydrogen production and power generation system. For the hydrogen production, a high temperature water electrolysis implemented in a solid oxide electrolysis cell is employed while the power is produced by the solar water power cycle. The high-temperature and high-pressure operation operation conditions of the electrolysis enable such an integration. On one

hand, some unit operations and equipment can be shared, such as the solar heater and some turbines. On the other hand, the heat exchangers in both sub-systems can be integrated and the power generated from turbines in both processes can supply electricity for the SOEC and the pumps in both processes. The integration includes mass, heat and work interaction and synergy.

The modeling is implemented in an integrated Aspen Plus and Matlab framework. Five models, including hydrogen production process, SOEC module, solar water power cycle, heat integration and efficiency calculation, are interconnected by a Matlab core script. Modeling results show 39.14% solar-to-hydrogen efficiency and 65.43% exergy efficiency when the SOEC is operated at endothermic mode. Such a system has the potential of co-producing hydrogen and electricity, which will be discussed in the next chapter.

6. CO-PRODUCTION OF SOLAR THERMAL POWER AND HYDROGEN

6.1 Introduction

One of the challenges of a renewable economy is the intermittent availability of the renewable energy resources. For example, the average solar energy availability in the US is only 1/5 of the day [13]. Therefore, for a solar energy system, additional energy should be harnessed and storage during the time when solar energy is available. Due to its high heating value and zero GHG emission potential, hydrogen is a clean energy carrier for energy storage in a sustainable future. Gençer et al has proposed the concept of "hydricity" as a paradigm of efficient co-production of hydrogen and electricity [5]. The key idea of a hydricity system includes the following aspects: (1) when the hydrogen and electricity production processes are integrated, the overall efficiencies of the integrated system is higher than each of the standalone system; (2) while electricity produced during the time when solar energy is available is directly supplied to the grid, the hydrogen can be storage for power production when solar energy is not available; (3) the hydrogen power production system can also be integrated with the existing hydrogen and electricity co-production system; (4) the hydricity system has the potential for large-scale power generation and energy storage.

In the study by Gençer et al, the hydricity system based on solar thermal energy is discussed, where solar thermal hydrogen production is by thermolysis of water and thermochemical cycles of Fe_3O_4/FeO. However, more methods of hydrogen production can be incorporated into the hydricity system. From chapter 5 we could see that the hydrogen production process by high temperature electrolysis can also be a fit into the hydricity. In this chapter, we will briefly discuss the integrated system in chapter 5 for

hydricity. Meanwhile, we will introduce the thermochemical production of hydrogen, especially the Zn/ZnO cycle, which is rendered more promising than the Fe_3O_4/FeO cycle in [5]. Then we discuss the feasibility of a hydricity system with hydrogen produced by the Zn/ZnO cycle.

6.2 Hydricity Concept and Processes

6.2.1 Hydricity concept

The concept of hydricity based on solar thermal energy can be described by Figure 6.1. Both the solar thermal electricity production and the solar hydrogen production requires solar thermal energy input, and water is the common feed for both the production processes. Multiple material, heat and electricity flows can be integrated within the two processes. During the time when solar energy is available, electricity is supplied to grid while hydrogen (oxygen) produced is stored. When solar energy is not available, the stored hydrogen can be used for power production by either hydrogen power plant or hydrogen fuel cell. Hydrogen power plant can be integrated with solar water power cycle [20] and hydrogen fuel cell can be integrated with the SOEC discussed in chapter 5. In addition, hydrogen can also be further processes as chemical feedstock or fuel for other uses. The entire integrated system enables a round-the-clock supply of power [5] and much integration largely increases the efficiencies of the process.

6.2.2 Hydricity processes

The hydricity system includes three sub-systems: solar thermal electricity production, solar hydrogen production, and hydrogen electricity production. As we discussed in chapter 5, the power is produced by the solat water power cycle [137]. Hydrogen electricity is produced by either hydrogen power plant [20] or hydrogen fuel cell. Basicly, the hydrogen power plant employs a hydrogen combustion chamber and the

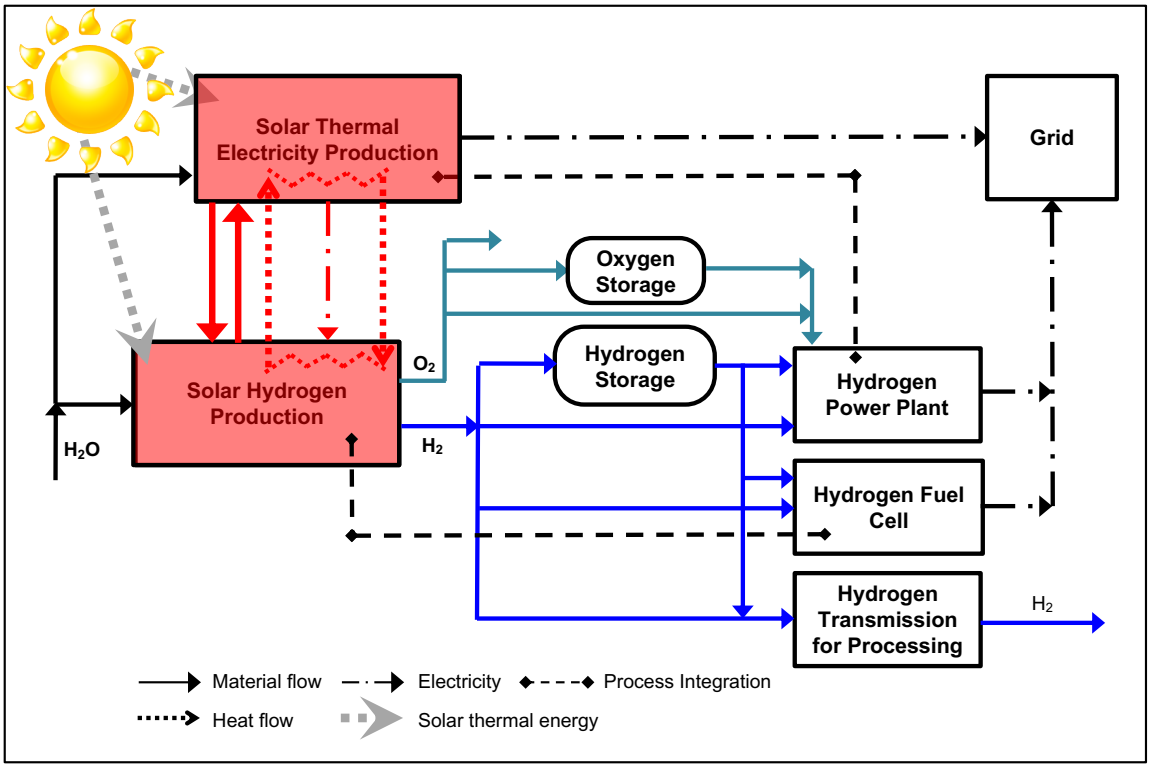

Fig. 6.1. Schematic for the concept of hydricity system based on solar thermal energy [20]

generated steam goes through a serious of turbines, the same as in the solar water power cycle, to produce electricity. The turbines can be shared with those in the solar water power cycle, which enables process integration between the solar thermal electricity production adn hydrogen pwoer plant. In this study, we use hydrogen power plant to produce electricity when solar energy is not available. For the hydrogen production process, apart from the high temperature electrolysis discussed in chapter 5, thermolysis and Fe_3O_4/FeO thermochemical cycle [20], we will discuss the Zn/ZnO thermochemical cycle in the next section.

6.3 Performance Metrics

In this chapter, the only output from the system is electricity, which indicates that hydrogen produced is used for electricity production to maintain a continuous power supply. Two metrics are used to evaluate the process modeling results: overall heat-to-electricity (OQTE) efficiency and overall sun-to-electricity (OSTE) efficiency. The overall heat-to-electricity is defined as the fraction of total heat input to the system recovered as electricity output over the entire power supply period:

$$\text{OQTE efficiency} = \frac{W_{\text{out}}}{Q_{\text{solar,in}}} \tag{6.1}$$

where W_{out} is the net eletricity output over the entire power supply period (when solar energy is available and not available), and $Q_{\text{solar,in}}$ is the heat input towards the system. The overall sun-to-electricity (OSTE) efficiency is defined as the fraction of total incident solar energy to the system recovered as electricity output over the entire power supply period:

$$\text{OSTE efficiency} = \frac{W_{\text{out}}}{E_{\text{solar,in}}} \tag{6.2}$$

where $E_{\text{solar,in}}$ is the total incident solar energy, which takes accounts the optical losses of solar concentrators, etc.

6.4 Hydricity Process with Hydrogen Produced by High Temperature Electrolysis

The integrated system of hydrogen production and power generation in chapter 5 can be directly used for a hydricity process. Instead of the producing the electricity demand for the SOEC, more electricity is produced for the grid. Modeling results show that The OQTE efficiency is 23.7% while the OSTE efficiency is 31.0% for a 24-hour continuous power supply. The exergy efficiency for the coproduction is 59.83%.

6.5 Two-step thermochemical water splitting cycles for hydrogen production

Among all the solar thermochemical hydrogen production routes, two-step solar water splitting cycle is very promising. It avoids the required super high temperature above 2500 K and the necessary high temperature separation technology for direct water thermolysis [111]; zero carbon emission can also be achieved if comparing with solar reforming and other carbon related methods [138]; moreover, compared with multi-step thermochemical cycles, reduction in the excess work required and heat loss associated with intermediate steps raises the efficiency of water splitting [139]. The two-step water splitting cycle can be can be presented by Figure 6.2.

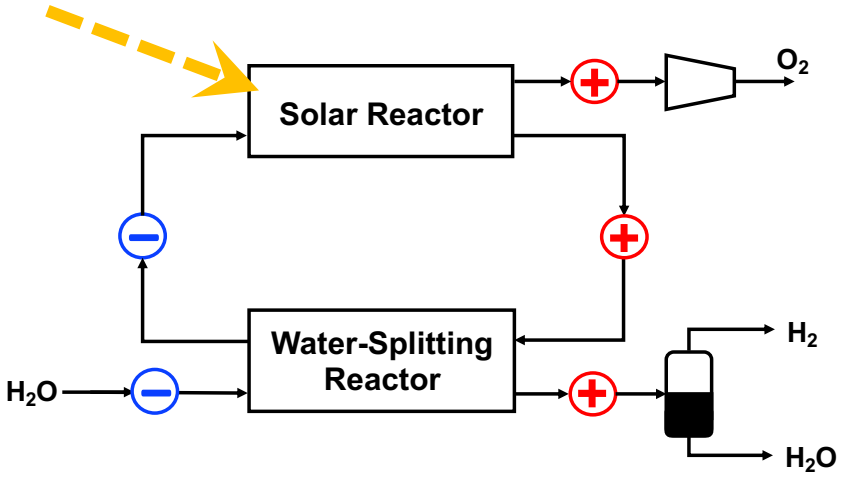

Fig. 6.2. Hydrogen production by a two-step water splitting thermochemical cycle [20]

A general set of equations can be written to represent the two-step water splitting cycle:

$$\mathrm{MO_x} \rightarrow \mathrm{MO_{x-\delta}} + \frac{\delta}{2}\mathrm{O_2} \quad \text{at } T_{\mathrm{red}} \tag{6.3}$$

$$\mathrm{MO_{x-\delta}} + \delta\mathrm{H_2O} \rightarrow \mathrm{MO_x} + \mathrm{H_2} \quad \text{at } T_{\mathrm{ox}} \tag{6.4}$$

where M indicates a metal and $\mathrm{MO_x}$ refers to the corresponding metal oxide. In this two-step cycle, the first endothermic step involves the solar thermal dissociation

of a metal oxide to its reduced metal or the lower-valence metal oxide; oxygen is released at the same time. The solar step typically occurs above 1700 K. The second exothermic non-solar step is the hydrolysis of the metal or the lower-valence metal oxide. The metal is reoxidized to its original metal oxide form and hydrogen is produced simultaneously. This step usually takes place at relatively low temperature which is 500 K lower than the endothermic step. The total reaction is simply the dissociation of water, and metal oxides can be circulated without consumption. In this hydrogen production method, H_2 and O_2 are produced at different steps so separation steps are eliminated.

Various metal oxides, even metal oxide hybrids have been investigated to test their compatibility with two-step water splitting cycle. Important characteristics of active materials include high H_2 production capacity, relatively low reduction temperature and fast kinetics [140]. In addition, the cost, toxicity, corrosiveness, lifetime, compatibility with containment materials are all factors that should be considered [140] [141].

Currently, two-step water splitting cycles are categorized into two types by their reaction mechanism: stoichiometric chemistry mechanism and oxygen vacancy chemistry mechanism. Under stoichiometric chemistries, 0.5 mol O_2 and 1 mol H_2 are generated for each mole of reacting oxide as it undergoes reduction or oxidization, respectively. For oxygen vacancy chemistry, however, O_2 is released by the formation of O vacancies in the metal oxide lattice, which is not consistent with normal stoichiometry. We will not discuss this type of reactions in this study.

For stoichiometric type of water splitting cycles, two categories, volatile and nonvolatile, are involved. In the endothermic decomposition reaction of metal oxide, the produced metal or lower-valence metal oxide can be gaseous, liquid or solid under the reaction temperature. For those where gaseous products are generated, such as $ZnO(s) \rightarrow Zn(g) + \frac{1}{2}O_2(g)$, a volatile stoichiometric category is defined. Since a mixture of metal (oxide) gas and oxygen is produced, a separation step is necessary. Nonvolatile stoichiometric type of water splitting cycles refers to those generate liquid or solid metal (oxide) in the dissociation step.

6.5.1 Volatile stoichiometric chemistries

Materials that belong to the volatile stoichiometric chemistries usually have relatively low boiling points, due to which gaseous products are formed. Low boiling points often indicates low molecular weight and high H2 production capacity in the measure of H_2 per mass of metal oxide. Despite the high H_2 production capacity, challenge emerges from separating the gaseous metal or metal oxide from the liberated oxygen. Usually a quenching step is introduced and further challenge comes from moving the condensed metal from the quenching zone to the hydrolysis reactor. ZnO/Zn cycle, SnO_2/SnO cycle, CdO/Cd cycle, and so on all belong to this category.

ZnO/Zn cycle is one of the most promising cycles among all the materials for two-step water splitting [138] [140]. The dissociation of ZnO without inert gas usually takes place at 1700-2000 °C and the hydrolysis at about 700 °C. Extensive research has been done on the ZnO/Zn cycle [142] [143] [144] [145] [146] [147]. Figure 6.3 shows the ZnO/Zn cycle. Note that a quenching step is required before oxygen can be acquired.

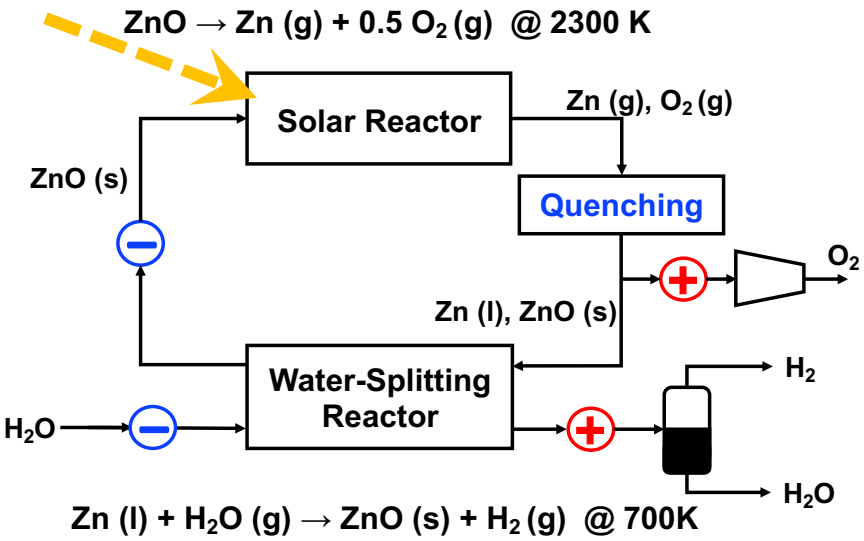

Fig. 6.3. Hydrogen production by Zn/ZnO thermochemical cycle

As previously mentioned, the major challenge of ZnO/Zn application is the separation of Zn(g) and oxygen. Weidenkaff et al found that gaseous zinc and oxygen can coexist in a meta-stable state in the absence of nucleation sites [148]. However, the ideal coexistence cannot happen in reality so that separation step is compulsory to avoid recombination of zinc and oxygen. Quenching is the most common method here and it is sensitive to the dilute ratio of Zn(g) in an inert gas and the temperature of the surface against which the gas products are quenched [149]. A quenching apparatus was designed by Gstoehl et al for optimized rapid cooling with diluting inert gas and Zn recovery from ZnO varies from 40%-94% with different quenching conditions [150]. Alternatively, electrolytic method have been proposed for in situ separation of Zn(g) and O2 at high temperatures [151].

Although ZnO/Zn cycle and other similar volatile stoiciometric cycles are promising from the perspective of hydrogen production capacity and favorable kinetics, there remain problems and challenges in gaseous products separation. The condensation of Zn on in the quenching apparatus, the separation of oxygen and the diluting inert gas and the moving of condensed Zn to the hydrolysis reactor are all factors we should consider before practical application.

6.5.2 Nonvolatile stoichiometric chemistries

The very first two-step water splitting cycle proposed was Fe_3O_4/FeO cycle (ferrite cycle), which belongs to the nonvolatile stoichiometric chemistries. For the ferrite cycle, the endothermic reaction takes place above 1600 K and oxygen partial pressure below 1 atm is required; the exothermic reaction can occur at temperatures up to 1200 K.

Although volatile reduced products are avoided, the Fe_3O_4/FeO cycle suffers from the complexity caused by the low melting of Fe_3O_4 (1870 K) and FeO (1650 K). Phase transition not only affects the efficiency of the entire cycle, but also leads to extensive sintering of the active materials, which causes material deactivation by decreasing the

surface area available for O_2 evolution and increasing the O^{2-} ion diffusion distance required to reach the reaction surface [152]. Low conversion can be caused as a result.

Overall efficiency regarding the ferrite cycles has been performed by several researchers. Nakamura concluded that the heat-to-hydrogen efficiency (HHV based) range from 36%-94%, varying with the extent of hear recuperation. In his study, a full conversion is assumed, with decomposition reaction at 2500 K and hydrolysis at 450 K [139]. Diver et al designed a heat engine that enables the countercurrent heat recovery between solid streams. With 85.6% recuperator efficiency and 35% reaction extent at 2300 K and 600 K for the reduction and oxidation reaction, the calculated efficiency of the ferrite cycle is 29%. Changing the temperature to 1800 K and 1000K, the efficiency could reach 44% [153]. Based on Diver's work, Mallapragada et al calculated the limiting and achievable efficiencies for ferrite cycle based solar hydrogen production. The heat loss related to solar energy collection is considered but full heat recuperation with zero temperature approach is also included. The optimal sun-to-hydrogen efficiency for a solar driven ferrite cycle is 54.4%. The efficiency is achieved when endothermic and exothermic reactions take place at 1600 K and 1000 K, respectively, with low pressure at 0.2 atm. In addition, solar concentration of 8000, and optical efficiency of 80% are assumed [112].

6.6 Modeling Approach

The modeling approach for the hydricity process with hydrogen produced by Zn/ZnO cycle is same to that discussed in chapter 5. As shown in Figure 6.4, the base model, which include the process flowsheet for the entire integrated system, is modeled in Aspen Plus. The hydrogen production model here is performed in Matlab while thermodynamic data are taken from HSC Chemistry database. All models are interacted through the Matlab core script [137].

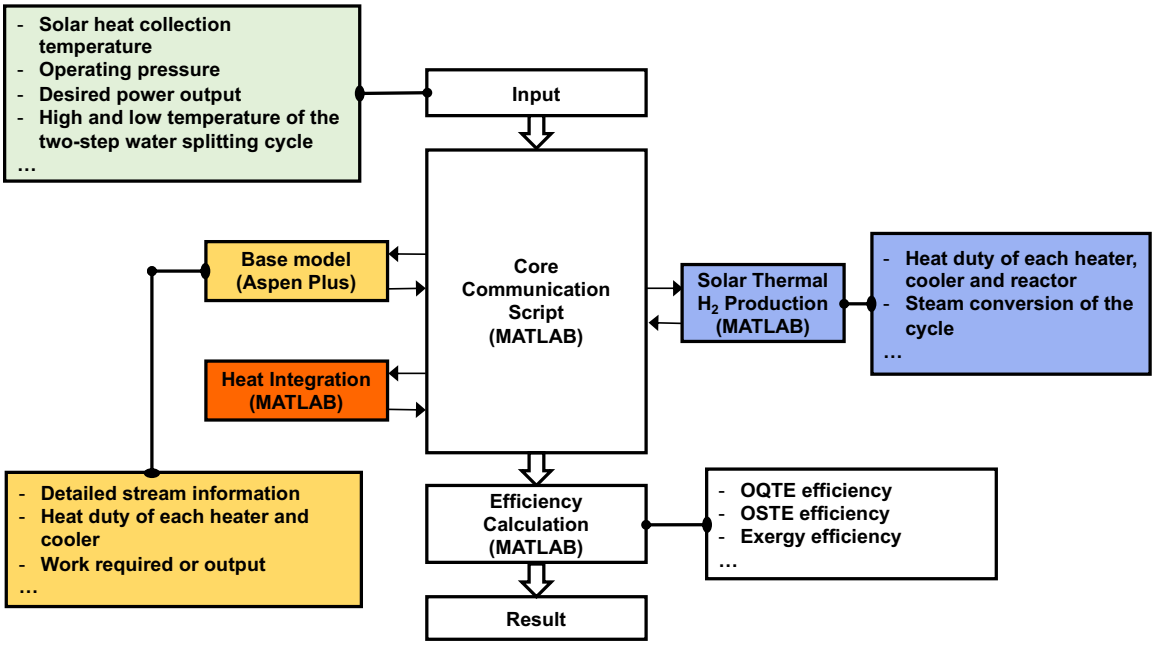

Fig. 6.4. Modeling approach for a hydricity process where H_2 is produced by thermochemical cycle

6.7 Process Description, Modeling results and Discussion

The flowsheet for the hydricity system with ZnO/Zn water splitting cycle is shown in Figure 6.5. The process consists of two main cycles: the power production cycle and the hydrogen production cycle. In the water power cycle, water, as the working fluid, is superheated by solar concentrator at the solar hear collection temperature T_{shc} and then expanded through high pressure turbine (HPT), medium pressure turbine (MPT) and condensing turbine (CT). It also undergoes a reheating stage between the HPT and the MPT through the solar superheating [137]. In the hydrogen production cycle, water is also superheated to the solar hear collection temperature T_{shc} and then goes through a high pressure turbine before entering the two-step water splitting cycle. The solar reactor of the two-step cycle, where the reduction of the metal oxide takes place, is driven by concentrated solar energy. The mixture of hydrogen and water released from the water-splitting reactor goes through an MPT before separation and

compression. The gaseous mixture of zinc and oxygen is quenched and then oxygen is liquefied. The quenching step happens rapidly so it is hard to recover the heat of the quenched stream. Therefore in simulation we consider the condition when the heat is either recovered of not. The parameters for the base case are listed in Table 6.1.

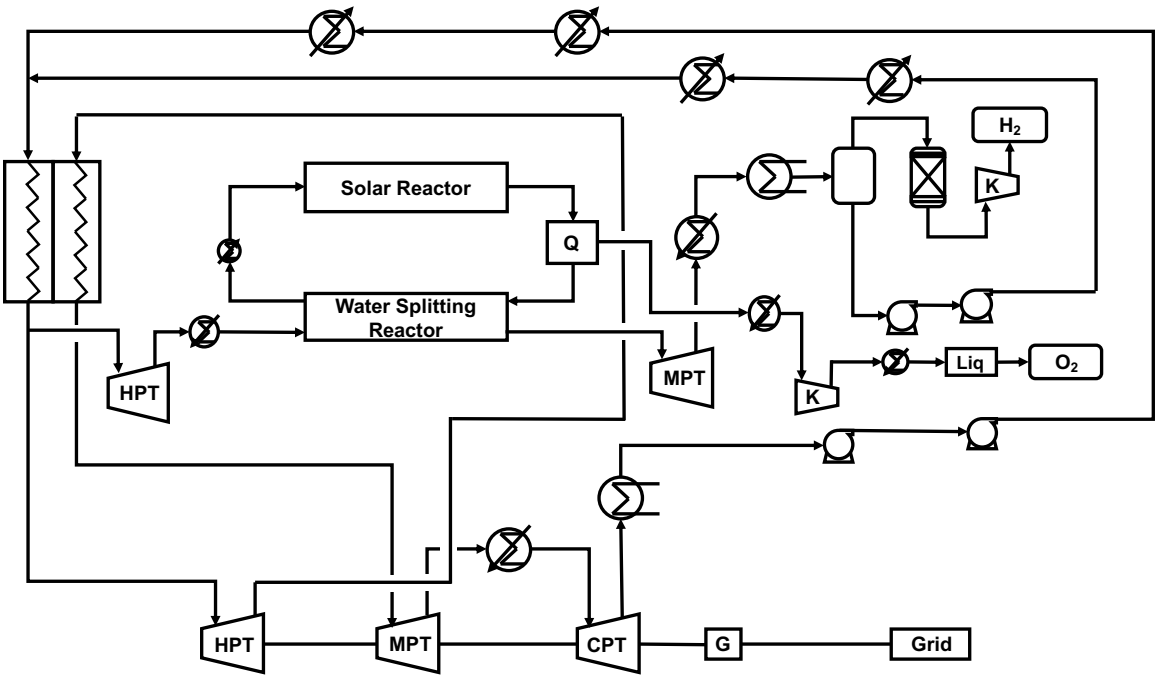

Fig. 6.5. Hydricity system with hydrogen produced by ZnO/Zn water splitting cycle

Combined with a hydrogen water power cycle, which is described in detail in [20], the hydricity system can be operated with continuous electricity output. The overall heat-to-electricity (OQTE) efficiency and overall sun-to-electricity (OSTE) efficiency in a 24-hour period are calculated and results are list in Table . When hydrogen and electricity are co-produced, the exergy efficiency of the base case is 28.46%.

Compared with the results for ferrite cycle in [20], the efficiencies are much lower. This might be attributed to several factors. First, for the cases of no quenching heat recovery, the high temperature heat of the outlet stream of the solar reactor is wasted,

Table 6.1.
Parameters of the base case of hydricity with ZnO/Zn water splitting cycle

Solar collection temperature	1600 K
Temperature of the reduction reaction	2300 K
Temperature of the hydrolysis reaction	700 K
Quenching heat recovery	No
Operating pressure	200 bar
H_2 storage pressure and temperature	35 bar and 298.15 K
O_2 storage pressure and pressure	1.1 bar and 91.1 K
CT outlet condensation	10%
Power output	100 MW
Solar energy availability	4.8 h/24 h

and therefore the entire system efficiencies are low. Second, the temperature of the solar reactor is much higher than the ferrite cycle, which is at 1600 K or 1800K, so the radiation loss is much larger. Third, although the ZnO can be 100% converted in the solar reactor, the recombination of Zn(g) and O_2 is unavoidable in the quenching process; so the recovery percentage of Zn from ZnO is low. In this way the high temperature solar heat supplied to the solar reactor is also wasted. All of these factors contributed to the low efficiency of the hydricity system with ZnO/Zn cycle. Similarly, for other volatile type of water splitting cycles, the similar problems exist. Therefore, despite of their promising potential for application in the solar hydrogen production, volatile type of two-step water splitting cycles are not compatible with our hydricity concept.

6.8 Conclusion

In this chapter, we investigate the two solar hydrogen production methods, high temperature electrolysis and thermochemical water splitting cycle, for their compat-

Table 6.2.
Summary of modeling results for a 100 MW constant power supply from hydricity process with Zn/ZnO cycle

Hydricity operating conditions				H_2 power cycle conditions		Efficiencies	
T_{shc} (K)	T_{red} (K)	T_{ox} (K)	Quenching heat recovery	Highest temperature (K)	H_2TE efficiency (%)	OQTE efficiency (%)	OSTE efficiency (%)
1600	2300	700	No	1600	64.7	16.5	10.9
1600	2300	700	Yes	1600	64.7	20.6	13.7
1800	2300	700	No	1800	67.5	17.2	11.3
1800	2300	700	Yes	1800	67.5	21.2	14.0
1600	2000	700	No	1600	64.7	16.9	12.1
1600	2000	700	Yes	1600	64.7	19.2	13.7
1800	2000	700	No	1800	67.5	17.6	12.6
1800	2000	700	Yes	1800	67.5	19.8	14.1

Note: H_2TE efficiency refers to the hydrogen-to-electricity efficiency of the hydrogen power cycle. The highest temperature refers to the temperature of the hydrogen combustion chamber and the efficiency numbers are from [20].

ibility with the hydricity system. Modeling results for the hydricity system with hydrogen produced by Zn/ZnO cycle show that at the best case, the overall sun-to-electricity efficiency is 14.1% over a 24-hour period. If the heat released from the quenching step cannot be recovered, which is very likely, the best sun-to-electricity efficiency is only 12.1%. Compared with the results with ferrite cycle, such efficiencies are quite low. However, the feasibility of the ferrite cycle is also questionable due to the problem of sintering of the materials. Therefore, although these thermochemical cycles show some promising features for solar hydrogen production, it is not as practical as high temperature electrolysis.

7. CONCLUSIONS AND OUTLOOK

7.1 Overview

This dissertation has discussed several aspects of the roadmap towards a sustainable future. Multiple synergies have been identified at various system levels, including resource level, building block level and process level.

At the resource level, a land requirement analysis is provided to investigate the possible land competition between renewable energy harnessing and food production. Solutions are proposed to relax such land constraints. A synergistic use of solar and wind energy is also discussed.

At the building block level, the co-production of hydrogen and electricity from solar energy is studied. High temperature electrolysis of water is a promising hydrogen production method to be integrated with solar thermal power production.

At the process level, multiple process integration and intensification strategies are proposed. For shale gas processing, which could play an important role for future chemical and fuel production, innovative process design and intensification have simplified the processes, and therefore enable the shale gas to be monetized at remote shale locations. For the aforementioned hydrogen and electricity co-production processes, process integration and intensification help increase the efficiency of the system.

The key findings of this thesis are summarized below, and possible future research directions are also discussed.

7.2 Process Intensification for Shale Gas Processing

In chapter 2, process design and intensification strategies are proposed for shale gas processing at remote locations. Evolved from the conventional shale gas processing design hierarchy, four configurations, along with example process flowsheets for each configuration, are synthesized: the NGL co-processing design, the integrated NGL recovery and activation design, the switched NGL recovery and activation design and the eliminated NGL recovery design. Apart from significant reduction in pieces of equipment involved in the process, the processes with these newly proposed configurations show high yield to desired products and less loss of shale resources. Several cases show the potential of over 90% product yield with minimized number of unit operations and equipment. Such process intensification is important for distributed manufacturing and local end-use demand supply.

7.3 Synergistic Use of Land for Renewable Energy Harvesting and Food Production

Chapter 3 presents a systematic land analysis for a 100% economy and identifies the challenge for the land competition between solar energy harvesting and food production. Chapter 4 proposes the concept of aglectric farming, where electricity is produced on agricultural land without diminishing the agricultural output from the land. Such a concept is a promising solution to relax the land constraint and applies to all the renewable energy resources. Solar and wind energy can be used synergistically for local energy supply while the food production is preserved. Aglectric farm can serve as the basis for multiple onsite production for farmers as electricity is available right there on farm.

7.4 Integration of Solar Powered Hydrogen and Electricity Production

Chapter 5 investigates the hydrogen production process by high temperature water electrolysis, which is powered by electricity generated by solar thermal energy. The sun-to-hydrogen efficiency and the exergy efficiency can achieve 39.14% and 65.43%, respectively. The operating conditions of the high temperature electrolysis provides the opportunity for process integration with solar thermal power production. A co-production mode could enable a continuous power supply by storing the hydrogen produced. While solar thermochemical hydrogen production might seem incompatible with such a integrated system, the high temperature electrolysis method for hydrogen production is more promising.

7.5 Synergy and Process Intensification

7.5.1 Identification of synergy at multiple levels

As we have discussed multiple times throughout this dissertation, synergy at multiple levels should be identified so that the entire energy system can work efficiently. Here as a summary of the thesis, we list below how to observe and identify the potential synergy at multiple levels.

- When different resources, building blocks or processes share the same objectives, a synergy could be identified. For example, solar and wind energy share the objective of supplying energy to end-uses. Therefore, the two resources can be used synergistically. Another possible synergy, which could be a future research direction, is the synergictic use of sustainable biomass and shale gas, which could both serve as carbon sources in a sustainable economy.

- When different resources, building blocks or processes share the same features, a synergy could be identified. For the integration of hydrogen and power production, both processes are driven by solar thermal energy, and both processes require high temperature, high pressure conditions. These common features

enable the process intensification, and are the key to observe synergy. For the integration of solar/wind energy harvesting and food production, the common feature is their large land demand. When the common feature is observed, the synergy could be identified from the perspective of land usage.

- Always look for the potential of a resource, a building block, a process, even a stream or a piece of equipment, and connect it with the need of other systems. For example, in the shale gas process we proposed in chapter 2, when a stream is needed as absorbent and a stream within the process has the potential to be an absorbent, the synergy could be identified.

7.5.2 Aspects of process intensification

Process intensification has extended to a broad area in process systems. Whenever synergy within a process, or multiple processes is identified, process intensification could be implemented. Apart from the traditional knowledge about process intensification which mainly focuses on smaller equipment, the concept of process intensification from this dissertation include following aspects.

- Simplified process with minimized unit operations and pieces of equipment.
- Process at small or modular scale, that is beneficial for local supply and distributed manufacturing.
- Integrated process for better performance, such as higher efficiencies.
- Integrated usage of resources that will save the resources or resolve the resource competition for a sustainable energy system.

7.6 Future Research Directions

This dissertation has only attempted several aspects of the roadmap towards a sustainable future (Figure 1.1. With the keyword synergy, all elements and their

interactions of the roadmap are worth future research. Several of the possible research directions are listed below.

- Systematic analysis for the requirement of shale gas and biomass as carbon sources in the future, and their associated energy demands. In current land analysis, all the chemical and fuel demand are assumed be to fulfilled by sustainable biomass, which could possibly be a challenge in both the capacity demand and land demand. A systematic analysis for the requirement, and furthermore an optimization for the use of both carbon resources would be meaningful for the future chemical production.

- Innovative methane conversion to chemicals. This works only proposes processes for natural gas liquids conversion. The usage of the major component in shale gas, methane, remains research. Although past researchers have done a lot of research on methane conversions, innovations are needed in terms of integration with other shale gas processing and utilization of renewable energy as energy resources to avoid green house gas emission.

- Onsite production of end-use demands on aglectric farms. Aglectric farms could enable a localized sustainable economy. For example, onsite production of hydrogen, clean water and fertilizer from aglectric farms could be interesting topics of future advances.

REFERENCES

REFERENCES

[1] United Nations, Department of Economic and Social Affairs, Population Division, "World population prospects 2019: Highlights," 2019.

[2] Exxon Mobil, "2019 outlook for energy: A perspective to 2040," Irving, Texas, 2019.

[3] British Petroleum, "BP statistical review of world energy report," London, UK, 2019.

[4] E. Gençer, C. Miskin, X. Sun, M. R. Khan, P. Bermel, M. A. Alam, and R. Agrawal, "Directing solar photons to sustainably meet food, energy, and water needs," *Scientific reports*, vol. 7, no. 1, pp. 1–7, 2017.

[5] E. Gençer, D. S. Mallapragada, F. Maréchal, M. Tawarmalani, and R. Agrawal, "Round-the-clock power supply and a sustainable economy via synergistic integration of solar thermal power and hydrogen processes," *Proceedings of the National Academy of Sciences*, vol. 112, no. 52, pp. 15 821–15 826, 2015.

[6] V. Smil, *Power density: a key to understanding energy sources and uses*. MIT Press, 2015.

[7] R. Agrawal, "Chemical engineering for a solar economy (2017 PV Danckwerts lecture)," *Chemical Engineering Science*, vol. 210, p. 115215, 2019.

[8] D. Gielen, F. Boshell, D. Saygin, M. D. Bazilian, N. Wagner, and R. Gorini, "The role of renewable energy in the global energy transformation," *Energy Strategy Reviews*, vol. 24, pp. 38–50, 2019.

[9] J. J. Siirola, "The impact of shale gas in the chemical industry," *AIChE Journal*, vol. 60, no. 3, pp. 810–819, 2014.

[10] P. Jaramillo, W. M. Griffin, and H. S. Matthews, "Comparative life-cycle air emissions of coal, domestic natural gas, LNG, and SNG for electricity generation," *Environmental science & technology*, vol. 41, no. 17, pp. 6290–6296, 2007.

[11] J. N. Armor, "Emerging importance of shale gas to both the energy & chemicals landscape," *Journal of Energy Chemistry*, vol. 22, no. 1, pp. 21–26, 2013.

[12] T. Ridha, "Transformation of biomass and shale gas carbon to fuels and chemicals," Ph.D. dissertation, Purdue University, West Lafayette, Indiana, 2018.

[13] N. S. Lewis and D. G. Nocera, "Powering the planet: Chemical challenges in solar energy utilization," *Proceedings of the National Academy of Sciences*, vol. 103, no. 43, pp. 15 729–15 735, 2006.

[14] S. Mathew, *Wind energy: fundamentals, resource analysis and economics*. Springer, 2006.

[15] R. Agrawal, N. R. Singh, F. H. Ribeiro, and W. N. Delgass, "Sustainable fuel for the transportation sector," *Proceedings of the National Academy of Sciences*, vol. 104, no. 12, pp. 4828–4833, 2007.

[16] U.S. Department of Energy, Office of Oil and Natural Gas, Office of Fossil Energy, "Natural gas flaring and venting: State and federal regulatory overview, trends, and impacts," 2019.

[17] M. Z. Jacobson, M. A. Delucchi, Z. A. Bauer, S. C. Goodman, W. E. Chapman, M. A. Cameron, C. Bozonnat, L. Chobadi, H. A. Clonts, P. Enevoldsen *et al.*, "100% clean and renewable wind, water, and sunlight all-sector energy roadmaps for 139 countries of the world," *Joule*, vol. 1, no. 1, pp. 108–121, 2017.

[18] R. Agrawal and N. R. Singh, "Solar energy to biofuels," *Annual review of chemical and biomolecular engineering*, vol. 1, pp. 343–364, 2010.

[19] Q. Chen, J. B. Dunn, and D. T. Allen, "Greenhouse gas emissions of transportation fuels from shale gas-derived natural gas liquids," *Procedia CIRP*, vol. 80, pp. 346–351, 2019.

[20] E. Gençer and R. Agrawal, "Strategy to synthesize integrated solar energy coproduction processes with optimal process intensification. Case study: Efficient solar thermal hydrogen production," *Computers & Chemical Engineering*, vol. 105, pp. 328–347, 2017.

[21] C. K. Miskin, Y. Li, A. Perna, R. G. Ellis, E. K. Grubbs, P. Bermel, and R. Agrawal, "Sustainable co-production of food and solar power to relax land-use constraints," *Nature Sustainability*, vol. 2, no. 10, pp. 972–980, 2019.

[22] US Energy Information Administration, "State energy data system (SEDS)," https://www.eia.gov/state/?sid=US, 2019.

[23] International Energy Agency, "World energy balances 2019," https://www.iea.org/reports/world-energy-balances-2019, 2020.

[24] P. Denholm, M. Hand, M. Jackson, and S. Ong, "Land use requirements of modern wind power plants in the United States," National Renewable Energy Lab.(NREL), Golden, CO (United States), Tech. Rep., 2009.

[25] C. Nickerson, R. Ebel, A. Borchers, F. Carriazo *et al.*, "Major uses of land in the united states, 2007," 2017.

[26] U.S. Energy Information Administration, "Annual energy outlook 2019, with projections to 2050," January 2019.

[27] US Energy Information Administration, "Monthly natural gas liquids report," Form EIA-816.

[28] S. E. DeRosa and D. T. Allen, "Impact of natural gas and natural gas liquids supplies on the united states chemical manufacturing industry: production cost effects and identification of bottleneck intermediates," *ACS Sustainable Chemistry & Engineering*, vol. 3, no. 3, pp. 451–459, 2015.

[29] U.S. Department of Energy, Office of Oil and Natural Gas, Office of Fossil Energy, "Natural gas flaring and venting: State and federal regulatory overview, trends, and impacts," June 2019.

[30] A. Wilcox, "Flaring issues, solutions & technologies-2019," Houston Advanced Research Center, Tech. Rep., 2019.

[31] C. He and F. You, "Shale gas processing integrated with ethylene production: novel process designs, exergy analysis, and techno-economic analysis," *Industrial & Engineering Chemistry Research*, vol. 53, no. 28, pp. 11 442–11 459, 2014.

[32] J. Gong and F. You, "A new superstructure optimization paradigm for process synthesis with product distribution optimization: Application to an integrated shale gas processing and chemical manufacturing process," *AIChE Journal*, vol. 64, no. 1, pp. 123–143, 2018.

[33] C. He and F. You, "Deciphering the true life cycle environmental impacts and costs of the mega-scale shale gas-to-olefins projects in the united states," *Energy & Environmental Science*, vol. 9, no. 3, pp. 820–840, 2016.

[34] A. Dutta, I. A. Karimi, and S. Farooq, "Technoeconomic perspective on natural gas liquids and methanol as potential feedstocks for producing olefins," *Industrial & Engineering Chemistry Research*, vol. 58, no. 2, pp. 963–972, 2018.

[35] J. Gong, M. Yang, and F. You, "A systematic simulation-based process intensification method for shale gas processing and ngls recovery process systems under uncertain feedstock compositions," *Computers & Chemical Engineering*, vol. 105, pp. 259–275, 2017.

[36] M. Yang and F. You, "Modular methanol manufacturing from shale gas: Techno-economic and environmental analyses of conventional large-scale production versus small-scale distributed, modular processing," *AIChE Journal*, vol. 64, no. 2, pp. 495–510, 2018.

[37] J. Gao and F. You, "Can modular manufacturing be the next game-changer in shale gas supply chain design and operations for economic and environmental sustainability?" *ACS Sustainable Chemistry & Engineering*, vol. 5, no. 11, pp. 10 046–10 071, 2017.

[38] T. E. Rufford, S. Smart, G. C. Watson, B. Graham, J. Boxall, J. D. Da Costa, and E. May, "The removal of co2 and n2 from natural gas: A review of conventional and emerging process technologies," *Journal of Petroleum Science and Engineering*, vol. 94, pp. 123–154, 2012.

[39] M. Netusil and P. Ditl, "Comparison of three methods for natural gas dehydration," *Journal of natural gas chemistry*, vol. 20, no. 5, pp. 471–476, 2011.

[40] M. Getu, S. Mahadzir, N. V. D. Long, and M. Lee, "Techno-economic analysis of potential natural gas liquid (ngl) recovery processes under variations of feed compositions," *Chemical Engineering Research and Design*, vol. 91, no. 7, pp. 1272–1283, 2013.

[41] H. S. Ganesh, D. P. Dean, S. Vernuccio, T. F. Edgar, M. Baldea, L. J. Broadbelt, M. A. Stadtherr, and D. T. Allen, "Product value modeling for an ngl to liquid transportation fuel process," *Industrial & Engineering Chemistry Research*, vol. 59, no. 7, pp. 3109–3119, 2020.

[42] R. Agrawal and Y. Li, "Process for upgrading natural gas liquids from shale gas without front-end demethanizer," Provisional US Patent Application, 62826313, 2020.

[43] T. Ridha, Y. Li, E. Gençer, J. J. Siirola, J. T. Miller, F. H. Ribeiro, and R. Agrawal, "Valorization of shale gas condensate to liquid hydrocarbons through catalytic dehydrogenation and oligomerization," *Processes*, vol. 6, no. 9, p. 139, 2018.

[44] S. Vernuccio, E. E. Bickel, R. Gounder, and L. J. Broadbelt, "Microkinetic model of propylene oligomerization on brønsted acidic zeolites at low conversion," *ACS Catalysis*, vol. 9, no. 10, pp. 8996–9008, 2019.

[45] B. V. Vora, "Development of dehydrogenation catalysts and processes," *Topics in Catalysis*, vol. 55, no. 19-20, pp. 1297–1308, 2012.

[46] T. Ren, M. Patel, and K. Blok, "Olefins from conventional and heavy feedstocks: Energy use in steam cracking and alternative processes," *Energy*, vol. 31, no. 4, pp. 425–451, 2006.

[47] K. Sundaram and G. Froment, "Modeling of thermal cracking kinetics—i: Thermal cracking of ethane, propane and their mixtures," *Chemical Engineering Science*, vol. 32, no. 6, pp. 601–608, 1977.

[48] M. Berreni and M. Wang, "Modelling and dynamic optimization of thermal cracking of propane for ethylene manufacturing," *Computers & chemical engineering*, vol. 35, no. 12, pp. 2876–2885, 2011.

[49] A. Stankiewicz and J. A. Moulijn, *Re-engineering the chemical processing plant: process intensification*. CRC Press, 2003.

[50] J. A. Turner, "A realizable renewable energy future," *Science*, vol. 285, no. 5428, pp. 687–689, 1999.

[51] V. Fthenakis, J. E. Mason, and K. Zweibel, "The technical, geographical, and economic feasibility for solar energy to supply the energy needs of the us," *Energy policy*, vol. 37, no. 2, pp. 387–399, 2009.

[52] M. Z. Jacobson, M. A. Delucchi, G. Bazouin, Z. A. Bauer, C. C. Heavey, E. Fisher, S. B. Morris, D. J. Piekutowski, T. A. Vencill, and T. W. Yeskoo, "100% clean and renewable wind, water, and sunlight (wws) all-sector energy roadmaps for the 50 united states," *Energy & Environmental Science*, vol. 8, no. 7, pp. 2093–2117, 2015.

[53] D. J. MacKay, "Solar energy in the context of energy use, energy transportation and energy storage," *Philosophical Transactions of the Royal Society A: Mathematical, Physical and Engineering Sciences*, vol. 371, no. 1996, p. 20110431, 2013.

[54] I. Capellán-Pérez, C. De Castro, and I. Arto, "Assessing vulnerabilities and limits in the transition to renewable energies: Land requirements under 100% solar energy scenarios," *Renewable and Sustainable Energy Reviews*, vol. 77, pp. 760–782, 2017.

[55] C. Macilwain, "Supergrid," *Nature*, vol. 468, no. 7324, p. 624, 2010.

[56] R. Agrawal and N. R. Singh, "Synergistic routes to liquid fuel for a petroleum-deprived future," *AIChE journal*, vol. 55, no. 7, pp. 1898–1905, 2009.

[57] US Energy Information Administration, "Net generation by state by type of producer by energy source," https://www.eia.gov/electricity/data/state/, 2016.

[58] Lawrence Livermore National Laboratory, "Energy flow charts," https://flowcharts.llnl.gov/commodities/energy, 2016.

[59] US Energy Information Administration, "How much electricity is lost in transmission and distribution in the United States?" https://www.eia.gov/tools/faqs/faq.php?id=105&t=3, 2017.

[60] US Energy Information Administration (EIA), "Annual energy outlook 2016," 2017.

[61] A. Poullikkas, "Sustainable options for electric vehicle technologies," *Renewable and Sustainable Energy Reviews*, vol. 41, pp. 1277–1287, 2015.

[62] F. An and D. Santini, "Assessing tank-to-wheel efficiencies of advanced technology vehicles," *SAE transactions*, pp. 636–654, 2003.

[63] N. R. Singh, W. N. Delgass, F. H. Ribeiro, and R. Agrawal, "Estimation of liquid fuel yields from biomass," *Environmental science & technology*, vol. 44, no. 13, pp. 5298–5305, 2010.

[64] R. A. Efroymson, M. H. Langholtz, K. Johnson, B. Stokes, C. C. Brandt, M. R. Davis, C. Hellwinckel, K. L. Kline, L. M. Eaton, J. Dunn *et al.*, "2016 billion-ton report: advancing domestic resources for a thriving bioeconomy, volume 2: environmental sustainability effects of select scenarios from volume 1," Oak Ridge National Lab.(ORNL), Oak Ridge, TN (United States), Tech. Rep., 2017.

[65] T. Parsell, S. Yohe, J. Degenstein, T. Jarrell, I. Klein, E. Gencer, B. Hewetson, M. Hurt, J. Im Kim, H. Choudhari *et al.*, "A synergistic biorefinery based on catalytic conversion of lignin prior to cellulose starting from lignocellulosic biomass," *Green Chemistry*, vol. 17, no. 3, pp. 1492–1499, 2015.

[66] E. I. Al-Musleh, D. S. Mallapragada, and R. Agrawal, "Continuous power supply from a baseload renewable power plant," *Applied energy*, vol. 122, pp. 83–93, 2014.

[67] H. Chen, T. N. Cong, W. Yang, C. Tan, Y. Li, and Y. Ding, "Progress in electrical energy storage system: A critical review," *Progress in natural science*, vol. 19, no. 3, pp. 291–312, 2009.

[68] M. Morandin, F. Maréchal, M. Mercangöz, and F. Buchter, "Conceptual design of a thermo-electrical energy storage system based on heat integration of thermodynamic cycles–part a: Methodology and base case," *Energy*, vol. 45, no. 1, pp. 375–385, 2012.

[69] Solar Direct, "Solar electric system sizing step 4 - determine the sun hours available per day," http://www.solardirect.com/pv/systems/gts/gts-sizing-sun-hours.html, 2018.

[70] National Renewable Energy Laboratory, "Best research-cell efficiency chart," https://www.nrel.gov/pv/cell-efficiency.html, Golden, CO, 2020.

[71] United States Department of Agriculture Economic Research Service, "Major land uses," https://www.ers.usda.gov/data-products/major-land-uses/glossary/.

[72] S. Ong, C. Campbell, P. Denholm, R. Margolis, and G. Heath, "Land-use requirements for solar power plants in the United States," National Renewable Energy Lab.(NREL), Golden, CO (United States), Tech. Rep., 2013.

[73] J. Ordóñez, E. Jadraque, J. Alegre, and G. Martínez, "Analysis of the photovoltaic solar energy capacity of residential rooftops in Andalusia (Spain)," *Renewable and Sustainable Energy Reviews*, vol. 14, no. 7, pp. 2122–2130, 2010.

[74] T. Hong, M. Lee, C. Koo, J. Kim, and K. Jeong, "Estimation of the available rooftop area for installing the rooftop solar photovoltaic (PV) system by analyzing the building shadow using Hillshade analysis," *Energy Procedia*, vol. 88, pp. 408–413, 2016.

[75] S. Izquierdo, C. Montañés, C. Dopazo, and N. Fueyo, "Roof-top solar energy potential under performance-based building energy codes: The case of Spain," *Solar Energy*, vol. 85, no. 1, pp. 208–213, 2011.

[76] The World Bank, Food and Agriculture Organization, "Agricultural land (% of land area)," https://data.worldbank.org/indicator/AG.LND.AGRI.ZS?view=chart, 2018.

[77] The World Bank. Food and Agriculture Organization, "Agricultural land (% of land area)," https://data.worldbank.org/indicator/AG.LND.FRST.ZS?view=chart, 2018.

[78] British Petroleum, "BP energy outlook, country and regional insights - China," London, UK, 2017.

[79] United Nations, Department of Economic and Social Affairs, "World population prospects: The 2017 revision—key findings and advance tables," Working Paper No. ESA/P/WP/248, 2017.

[80] D. Tilman, "Food & health of a full earth," *Daedalus*, vol. 144, no. 4, pp. 5–7, 2015.

[81] A. Armstrong, N. J. Ostle, and J. Whitaker, "Solar park microclimate and vegetation management effects on grassland carbon cycling," *Environmental Research Letters*, vol. 11, no. 7, p. 074016, 2016.

[82] H. Marrou, L. Guilioni, L. Dufour, C. Dupraz, and J. Wéry, "Microclimate under agrivoltaic systems: Is crop growth rate affected in the partial shade of solar panels?" *Agricultural and Forest Meteorology*, vol. 177, pp. 117–132, 2013.

[83] H. Marrou, L. Dufour, and J. Wery, "How does a shelter of solar panels influence water flows in a soil–crop system?" *European Journal of Agronomy*, vol. 50, pp. 38–51, 2013.

[84] A. Goetzberger and A. Zastrow, "On the coexistence of solar-energy conversion and plant cultivation," *International Journal of Solar Energy*, vol. 1, no. 1, pp. 55–69, 1982.

[85] C. Dupraz, H. Marrou, G. Talbot, L. Dufour, A. Nogier, and Y. Ferard, "Combining solar photovoltaic panels and food crops for optimising land use: towards new agrivoltaic schemes," *Renewable energy*, vol. 36, no. 10, pp. 2725–2732, 2011.

[86] H. Dinesh and J. M. Pearce, "The potential of agrivoltaic systems," *Renewable and Sustainable Energy Reviews*, vol. 54, pp. 299–308, 2016.

[87] B. Valle, T. Simonneau, F. Sourd, P. Pechier, P. Hamard, T. Frisson, M. Ryckewaert, and A. Christophe, "Increasing the total productivity of a land by combining mobile photovoltaic panels and food crops," *Applied energy*, vol. 206, pp. 1495–1507, 2017.

[88] Fraunhofer Institute for Solar Energy Systems, "Harvesting the sun for power and produce—agrophotovoltaics increases the land use efficiency by over 60 percent," https://www.ise.fraunhofer.de/en/press-media/press-releases/2017/harvesting-the-sun-for-power-and-produce-agrophotovoltaics-increases-the-land-use-efficiency-by-over-60-percent.html, 2017.

[89] X. Sun, M. R. Khan, C. Deline, and M. A. Alam, "Optimization and performance of bifacial solar modules: A global perspective," *Applied energy*, vol. 212, pp. 1601–1610, 2018.

[90] B. Zhao, X. Sun, M. R. Khan, and M. A. Alam, "Purdue university bifacial module calculator (PUB)," https://nanohub.org/resources/pub, 2018.

[91] M. R. Khan, A. Hanna, X. Sun, and M. A. Alam, "Vertical bifacial solar farms: Physics, design, and global optimization," *Applied energy*, vol. 206, pp. 240–248, 2017.

[92] T. U. Ulavi, J. H. Davidson, and T. Hebrink, "Analysis of a hybrid PV/T concept based on wavelength selective mirror films," *Journal of solar energy engineering*, vol. 136, no. 3, 2014.

[93] P. Charalambous, G. G. Maidment, S. A. Kalogirou, and K. Yiakoumetti, "Photovoltaic thermal PV/T collectors: A review," *Applied thermal engineering*, vol. 27, no. 2-3, pp. 275–286, 2007.

[94] O. Ilic, P. Bermel, G. Chen, J. D. Joannopoulos, I. Celanovic, and M. Soljačić, "Tailoring high-temperature radiation and the resurrection of the incandescent source," *Nature nanotechnology*, vol. 11, no. 4, p. 320, 2016.

[95] J. Y. Zhengshan, K. C. Fisher, B. M. Wheelwright, R. P. Angel, and Z. C. Holman, "PVMirror: a new concept for tandem solar cells and hybrid solar converters," *IEEE Journal of Photovoltaics*, vol. 5, no. 6, pp. 1791–1799, 2015.

[96] X.-G. Zhu, S. P. Long, and D. R. Ort, "What is the maximum efficiency with which photosynthesis can convert solar energy into biomass?" *Current opinion in biotechnology*, vol. 19, no. 2, pp. 153–159, 2008.

[97] B. DEUTCH and O. RASMUSSEN, "Growth chamber illumination and photomorphogenetic efficacy i. physiological action of infrared radiation beyond 750 nm," *Physiologia Plantarum*, vol. 30, no. 1, pp. 64–71, 1974.

[98] G. D. Massa, H.-H. Kim, R. M. Wheeler, and C. A. Mitchell, "Plant productivity in response to led lighting," *HortScience*, vol. 43, no. 7, pp. 1951–1956, 2008.

[99] K. J. McCree, "The action spectrum, absorptance and quantum yield of photosynthesis in crop plants," *Agricultural Meteorology*, vol. 9, pp. 191–216, 1971.

[100] NASA Langley Research Center, "POWER project data sets," https://power.larc.nasa.gov/, 2018.

[101] S. Jose, "Agroforestry for ecosystem services and environmental benefits: an overview," *Agroforestry systems*, vol. 76, no. 1, pp. 1–10, 2009.

[102] U.S. Energy Information Administration, "Capacity factors for utility scale generators not primarily using fossil fuels, January 2013-February 2019," https://www.eia.gov/electricity/monthly/epm_table_grapher.php?t=epmt_6_07_b, Electric Power Monthly. Table 6.7.B.

[103] Office of Energy Efficiency & Renewable Energy, "U.S. average annual wind speed at 80 meters," https://windexchange.energy.gov/maps-data/319.

[104] Office of Energy Efficiency and Renewable Energy, "U.S. wind energy performance (capacity factors) in 2017," https://windexchange.energy.gov/maps-data/332.

[105] R. Agrawal, M. Offutt, and M. P. Ramage, "Hydrogen economy-an opportunity for chemical engineers?" *AIChE journal*, vol. 51, no. 6, pp. 1582–1589, 2005.

[106] N. R. Council *et al.*, *The hydrogen economy: opportunities, costs, barriers, and R&D needs*. National Academies Press, 2004.

[107] R. von Helmolt and U. Eberle, "Fuel cell vehicles: Status 2007," *Journal of Power Sources*, vol. 165, no. 2, pp. 833–843, 2007.

[108] N. Brandon and Z. Kurban, "Clean energy and the hydrogen economy," *Philosophical Transactions of the Royal Society A: Mathematical, Physical and Engineering Sciences*, vol. 375, no. 2098, p. 20160400, 2017.

[109] International Energy Agency, "Iea energy technology essentials: Hydrogen production & distribution," https://www.iea.org/reports/iea-energy-technology-essentials-hydrogen-production-distribution, Paris, 2007.

[110] J. D. Holladay, J. Hu, D. L. King, and Y. Wang, "An overview of hydrogen production technologies," *Catalysis today*, vol. 139, no. 4, pp. 244–260, 2009.

[111] E. Bozoglan, A. Midilli, and A. Hepbasli, "Sustainable assessment of solar hydrogen production techniques," *Energy*, vol. 46, no. 1, pp. 85–93, 2012.

[112] D. S. Mallapragada and R. Agrawal, "Limiting and achievable efficiencies for solar thermal hydrogen production," *International journal of hydrogen energy*, vol. 39, no. 1, pp. 62–75, 2014.

[113] H. Spacil and C. Tedmon Jr, "Electrochemical dissociation of water vapor in solid oxide electrolyte cells: I. thermodynamics and cell characteristics," *Journal of the Electrochemical Society*, vol. 116, no. 12, p. 1618, 1969.

[114] H. S. Spacil and C. S. Tedmon, "Electrochemical dissociation of water vapor in solid oxide electrolyte cells ii. materials, fabrication, and properties," *Journal of The Electrochemical Society*, vol. 116, no. 12, pp. 1627–1633, 1969.

[115] W. Dönitz and E. Erdle, "High-temperature electrolysis of water vapor—status of development and perspectives for application," *International Journal of Hydrogen Energy*, vol. 10, no. 5, pp. 291–295, 1985.

[116] W. Doenitz, R. Schmidberger, E. Steinheil, and R. Streicher, "Hydrogen production by high temperature electrolysis of water vapour," *International Journal of Hydrogen Energy*, vol. 5, no. 1, pp. 55–63, 1980.

[117] W. Dönitz, "Economics and potential application of electrolytic hydrogen in the next decades," *International journal of hydrogen energy*, vol. 9, no. 10, pp. 817–821, 1984.

[118] K. Quandt and R. Streicher, "Concept and design of a 3.5 mw pilot plant for high temperature electrolysis of water vapor," *International journal of hydrogen energy*, vol. 11, no. 5, pp. 309–315, 1986.

[119] J. Sigurvinsson, C. Mansilla, P. Lovera, and F. Werkoff, "Can high temperature steam electrolysis function with geothermal heat?" *International Journal of Hydrogen Energy*, vol. 32, no. 9, pp. 1174–1182, 2007.

[120] E. Toklu, A. C. Avci, K. Kaygusuz, and M. Gur, "A research on hydrogen production from industrial waste heat by thermal water splitting," *International Journal of Hydrogen Energy*, vol. 41, no. 24, pp. 10 071–10 079, 2016.

[121] M. N. Manage, E. Sorensen, S. Simons, and D. J. Brett, "A modelling approach to assessing the feasibility of the integration of power stations with steam electrolysers," *Chemical Engineering Research and Design*, vol. 92, no. 10, pp. 1988–2005, 2014.

[122] S. Fujiwara, S. Kasai, H. Yamauchi, K. Yamada, S. Makino, K. Matsunaga, M. Yoshino, T. Kameda, T. Ogawa, S. Momma *et al.*, "Hydrogen production by high temperature electrolysis with nuclear reactor," *Progress in Nuclear Energy*, vol. 50, no. 2-6, pp. 422–426, 2008.

[123] M. Jaszczur, M. A. Rosen, T. Śliwa, M. Dudek, and L. Pieńkowski, "Hydrogen production using high temperature nuclear reactors: Efficiency analysis of a combined cycle," *International Journal of Hydrogen Energy*, vol. 41, no. 19, pp. 7861–7871, 2016.

[124] J. O'Brien, M. McKellar, E. Harvego, and C. Stoots, "High-temperature electrolysis for large-scale hydrogen and syngas production from nuclear energy–summary of system simulation and economic analyses," *International journal of hydrogen energy*, vol. 35, no. 10, pp. 4808–4819, 2010.

[125] K. Im-orb, N. Visitdumrongkul, D. Saebea, Y. Patcharavorachot, and A. Arpornwichanop, "Flowsheet-based model and exergy analysis of solid oxide electrolysis cells for clean hydrogen production," *Journal of Cleaner Production*, vol. 170, pp. 1–13, 2018.

[126] V. Menon, V. M. Janardhanan, and O. Deutschmann, "A mathematical model to analyze solid oxide electrolyzer cells (soecs) for hydrogen production," *Chemical Engineering Science*, vol. 110, pp. 83–93, 2014.

[127] M. Ni, M. K. Leung, and D. Y. Leung, "Parametric study of solid oxide steam electrolyzer for hydrogen production," *International Journal of Hydrogen Energy*, vol. 32, no. 13, pp. 2305–2313, 2007.

[128] M. Ni, M. K. H. Leung, and D. Y. C. Leung, "Energy and exergy analysis of hydrogen production by solid oxide steam electrolyzer plant," *International journal of hydrogen energy*, vol. 32, no. 18, pp. 4648–4660, 2007.

[129] L. Mingyi, Y. Bo, X. Jingming, and C. Jing, "Thermodynamic analysis of the efficiency of high-temperature steam electrolysis system for hydrogen production," *Journal of Power Sources*, vol. 177, no. 2, pp. 493–499, 2008.

[130] J. Laurencin, D. Kane, G. Delette, J. Deseure, and F. Lefebvre-Joud, "Modelling of solid oxide steam electrolyser: Impact of the operating conditions on hydrogen production," *Journal of Power Sources*, vol. 196, no. 4, pp. 2080–2093, 2011.

[131] H. Zhang, S. Su, X. Chen, G. Lin, and J. Chen, "Configuration design and performance optimum analysis of a solar-driven high temperature steam electrolysis system for hydrogen production," *International Journal of Hydrogen Energy*, vol. 38, no. 11, pp. 4298–4307, 2013.

[132] J. Sanz-Bermejo, J. Muñoz-Antón, J. Gonzalez-Aguilar, and M. Romero, "Optimal integration of a solid-oxide electrolyser cell into a direct steam generation solar tower plant for zero-emission hydrogen production," *Applied energy*, vol. 131, pp. 238–247, 2014.

[133] M. T. Balta, O. Kizilkan, and F. Yılmaz, "Energy and exergy analyses of integrated hydrogen production system using high temperature steam electrolysis," *international journal of hydrogen energy*, vol. 41, no. 19, pp. 8032–8041, 2016.

[134] A. A. AlZahrani and I. Dincer, "Design and analysis of a solar tower based integrated system using high temperature electrolyzer for hydrogen production," *International Journal of Hydrogen Energy*, vol. 41, no. 19, pp. 8042–8056, 2016.

[135] M. Seitz, H. von Storch, A. Nechache, and D. Bauer, "Techno economic design of a solid oxide electrolysis system with solar thermal steam supply and thermal energy storage for the generation of renewable hydrogen," *International Journal of Hydrogen Energy*, vol. 42, no. 42, pp. 26 192–26 202, 2017.

[136] M. Ozturk and I. Dincer, "Thermodynamic analysis of a solar-based multigeneration system with hydrogen production," *Applied Thermal Engineering*, vol. 51, no. 1-2, pp. 1235–1244, 2013.

[137] E. Gençer and R. Agrawal, "Synthesis of efficient solar thermal power cycles for baseload power supply," *Energy Conversion and Management*, vol. 133, pp. 486–497, 2017.

[138] A. Steinfeld, "Solar thermochemical production of hydrogen—-a review," *Solar energy*, vol. 78, no. 5, pp. 603–615, 2005.

[139] T. Nakamura, "Hydrogen production from water utilizing solar heat at high temperatures," *Solar energy*, vol. 19, no. 5, pp. 467–475, 1977.

[140] C. L. Muhich, B. D. Ehrhart, I. Al-Shankiti, B. J. Ward, C. B. Musgrave, and A. W. Weimer, "A review and perspective of efficient hydrogen generation via solar thermal water splitting," *Wiley Interdisciplinary Reviews: Energy and Environment*, vol. 5, no. 3, pp. 261–287, 2016.

[141] R. Perret, "Solar thermochemical hydrogen production research (stch)," Sandia National Lab.(SNL-CA), Livermore, CA (United States), Tech. Rep., 2011.

[142] F. O. Ernst, A. Steinfeld, and S. E. Pratsinis, "Hydrolysis rate of submicron zn particles for solar h2 synthesis," *international journal of hydrogen energy*, vol. 34, no. 3, pp. 1166–1175, 2009.

[143] C. Perkins, P. R. Lichty, and A. W. Weimer, "Thermal zno dissociation in a rapid aerosol reactor as part of a solar hydrogen production cycle," *International Journal of Hydrogen Energy*, vol. 33, no. 2, pp. 499–510, 2008.

[144] S. Möller and R. Palumbo, "Solar thermal decomposition kinetics of zno in the temperature range 1950–2400k," *Chemical engineering science*, vol. 56, no. 15, pp. 4505–4515, 2001.

[145] C. Perkins, P. Lichty, and A. W. Weimer, "Determination of aerosol kinetics of thermal zno dissociation by thermogravimetry," *Chemical engineering science*, vol. 62, no. 21, pp. 5952–5962, 2007.

[146] A. Weidenkaff, A. Reller, A. Wokaun, and A. Steinfeld, "Thermogravimetric analysis of the zno/zn water splitting cycle," *Thermochimica Acta*, vol. 359, no. 1, pp. 69–75, 2000.

[147] L. O. Schunk and A. Steinfeld, "Kinetics of the thermal dissociation of zno exposed to concentrated solar irradiation using a solar-driven thermogravimeter in the 1800–2100 k range," *AIChE journal*, vol. 55, no. 6, pp. 1497–1504, 2009.

[148] A. Weidenkaff, A. Steinfeld, A. Wokaun, P. Auer, B. Eichler, and A. Reller, "Direct solar thermal dissociation of zinc oxide: condensation and crystallisation of zinc in the presence of oxygen," *Solar Energy*, vol. 65, no. 1, pp. 59–69, 1999.

[149] P. G. Loutzenhiser, A. Meier, and A. Steinfeld, "Review of the two-step h2o/co2-splitting solar thermochemical cycle based on zn/zno redox reactions," *Materials*, vol. 3, no. 11, pp. 4922–4938, 2010.

[150] D. Gstoehl, A. Brambilla, L. Schunk, and A. Steinfeld, "A quenching apparatus for the gaseous products of the solar thermal dissociation of zno," *Journal of materials science*, vol. 43, no. 14, pp. 4729–4736, 2008.

[151] E. A. Fletcher, "Solarthermal and solar quasi-electrolytic processing and separations: Zinc from zinc oxide as an example," *Industrial & engineering chemistry research*, vol. 38, no. 6, pp. 2275–2282, 1999.

[152] P. Lichty, X. Liang, C. Muhich, B. Evanko, C. Bingham, and A. W. Weimer, "Atomic layer deposited thin film metal oxides for fuel production in a solar cavity reactor," *International journal of hydrogen energy*, vol. 37, no. 22, pp. 16 888–16 894, 2012.

[153] R. B. Diver, J. E. Miller, M. D. Allendorf, N. P. Siegel, and R. E. Hogan, "Solar thermochemical water-splitting ferrite-cycle heat engines," *Journal of Solar Energy Engineering*, vol. 130, no. 4, 2008.

[154] J. S. Stein, W. F. Holmgren, J. Forbess, and C. W. Hansen, "Pvlib: Open source photovoltaic performance modeling functions for matlab and python," in *2016 ieee 43rd photovoltaic specialists conference (pvsc)*. IEEE, 2016, pp. 3425–3430.

[155] World Bank Group, "Global solar atlas," http://globalsolaratlas.info/, 2019.

APPENDICES

A. SHADOW DEPTH AND POWER OUTPUT FOR VARIOUS LOCATIONS

To demonstrate that our shadow modeling is valid for different locations around the US, we choose locations with low (Fresno, CA), intermediate (South Plains region of Texas), and high (West Lafayette, IN) fraction of diffuse light as examples to represent most major agricultural regions of the U.S. The shadow simulation results as well as power output from corresponding aglectric farms are listed in the Table .

From Table 1 we can see that the shadow modeling for different locations follows the same trend. The average shadow depth for a same configuration at different locations is at same level, but in higher diffuse radiation region, the shadow is more evenly distributed (lower standard deviation of the shadow depth).

Table A.1.
Shadow depth and power output for Fresno, CA

	Configuration	Panel design	Row spacing (m)	Average shadow depth (%)	Shadow depth s.d. (%)	Power output (W/m^2)
A	South facing	Continuous	3.81	34.6	20.8	16.6
B	South facing	Checkered	3.81	17.3	10.4	8.3
C	EW tracking	Continuous	3.81	27.2	0.8	22.2
D	EW tracking	Continuous	7.62	21.5	0.8	11.1
E	EW tracking	Checkered	7.62	11.9	1.5	5.5

Table A.2.
Shadow depth and power output for South Plains region, Texas

	Configuration	Panel design	Row spacing (m)	Average shadow depth (%)	Shadow depth s.d. (%)	Power output (W/m^2)
A	South facing	Continuous	3.81	35.2	15.2	11.8
B	South facing	Checkered	3.81	17.6	7.6	5.9
C	EW tracking	Continuous	3.81	31.5	0.6	15.1
D	EW tracking	Continuous	7.62	21.4	0.6	7.6
E	EW tracking	Checkered	7.62	11.5	1.1	3.8

Table A.3.
Shadow depth and power output for West Lafayette, IN

	Configuration	Panel design	Row spacing (m)	Average shadow depth (%)	Shadow depth s.d. (%)	Power output (W/m^2)
A	South facing	Continuous	3.81	35.0	10.1	8.1
B	South facing	Checkered	3.81	17.5	5.0	4.0
C	EW tracking	Continuous	3.81	34.6	0.3	10
D	EW tracking	Continuous	7.62	21.2	0.3	5.0
E	EW tracking	Checkered	7.62	11.1	0.7	2.5

B. SHADOW SIMULATION

The shadow depth was calculated for simple panel configurations and is displayed in a top-down view for 50 m × 45.72 m farm plots to show edge effects (Figure 4.2). To eliminate the effect of plot size on shadow depth averages and standard deviation, calculations were performed using infinite periodicity (Table 4.1). For the checkered pattern, we employed with transparent spacers, each with dimensions of 0.25 m × 0.25 m (Table 4.1). The Haurwitz clear sky irradiance model and the Orgill and Hollands model for determining diffuse horizontal irradiance have been implemented for three agriculturally productive locations in Indiana (40.4° N, 86.9° W), Texas (33.5° N, 101.8° W) and California (36.6° N, 119.9° W) via PVLIB—a Sandia-originated MATLAB open-source library for photovoltaics modelling [154]. Considering the high elevation of the panels necessary for navigation by farm equipment, it is assumed that diffuse light is uniformly distributed on the ground. The amount of diffuse light was determined by subtracting the diffuse fraction incident on PV panels, as calculated by the Perez model, from the total diffuse light for each time step. Tracking PV systems were modelled with the same dimensionality as the south-facing fixed systems (1.5-m-wide modules, infinitely long), and with a ±90° range of motion. Shadow position was calculated using the ray-tracing methodology, which models the Sun as a plane source with a variable position depending on the time of day, generated from PVLIB for the locations listed above on 1 June 2018. The ground was divided into finite spatial elements of identical size for incident energy integration, which was calculated with a time resolution of 1 min. The shadow depth was defined as the percentage reduction in incident energy at a given location over 1 d compared with the open field case. The averaged shadow depth in Table 4.1 refers to the average shadow depth of all spatial finite elements, calculated as a summation of the shadow depth values for all elements and divided by the number of elements. The shadow depth standard

deviation in Table 4.1 is the standard deviation of the values of shadow depth across all spatial finite elements. This translates to the spatial homogeneity of the shadow.

C. POWER OUTPUT OF VERTICAL BIFACIAL PV AGLECTRIC FARMS

C.1 East-west Facing Vertical Bifacial PV Aglectric Farms

The power output of East-West (E-W) facing vertical bifacial PV aglectric farms was estimated using the Purdue University Bifacial Module Calculator (PUB) using the parameters shown in Figure C.1 [89] [90]. The power output was modeled for four locations as listed in Table C.1. These locations were chosen as they cover a broad range of irradiance conditions that could be encountered globally. Note that the power estimates obtained using this model are based on the panel area. In estimating the output on a land area basis, the output was divided by the row spacing of 3.81 m and further multiplied by 50% to account for the checkered pattern assumed. The irradiance data was obtained from the Global Solar Atlas database [155].

Table C.1.
Irradiance data for four locations representative of a variety of meteorological conditions [155]

Location	Latitude	Longitude	Direct normal irradiation kWh/m^2· yr	Diffuse horizontal irradiation kWh/m^2· yr
Seattle, WA	47.6038	−122.3301	1283 (low)	529 (moderate)
West Lafayette, IN	40.4259	−86.9081	1501 (moderate)	611 (moderate)
Miami, FL	25.7743	−80.1937	1900 (high)	702 (high)
Daggett, CA	34.8634	−116.888	2888 (very high)	441 (low)

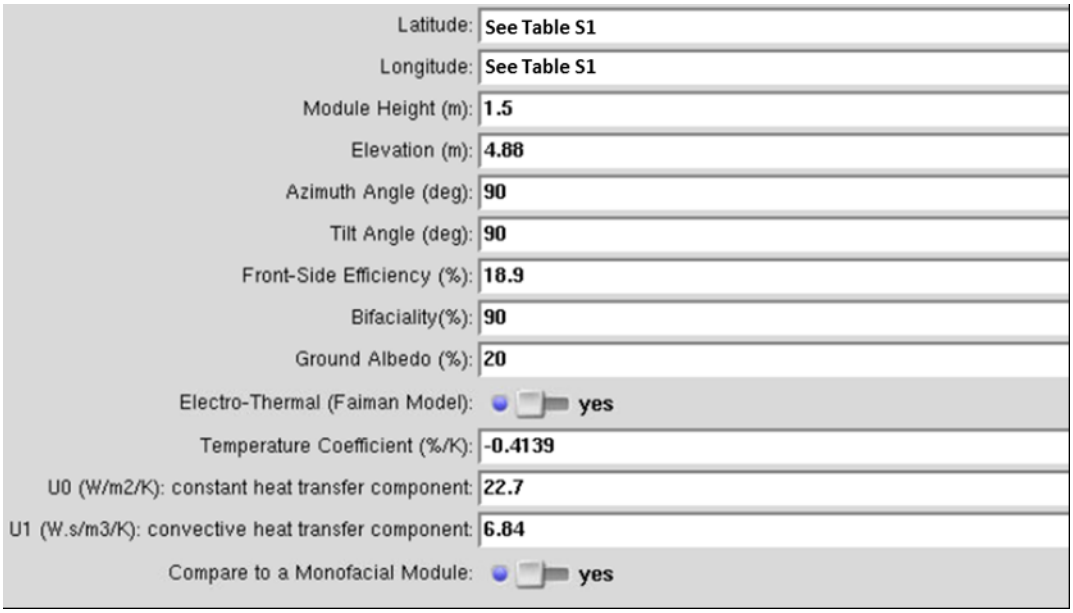

Fig. C.1. Input parameters for modeling of power output of E-W facing vertical bifacial PV aglectric farms using the Purdue University Bifacial Module Calculator (PUB) [90]

C.2 North-South Facing Vertical Bifacial PV Aglectric Farms

The power output of the North-South facing vertical bifacial PV aglectric farms was estimated using the model of Khan et al [91]. In using this model, we assume that the panels are always oriented such that they receive no direct insolation. Hence, we need only consider absorption of diffuse and albedo light. Consistent with the nomenclature in Khan et al., equation 21 for the power output of North-South facing vertical bifacial panels on a farm area basis becomes:

$$I^{(bifacial)}_{PV(dir),0} = I^{(bifacial)}_{PV(diff),0} + I^{(bifacial)}_{PV(Alb),0} \tag{C.1}$$

Note that the calculation of $I^{(bifacial)}_{PV(diff),0}$ is as defined in their model. However, due to the North-South facing orientation $I^{(bifacial)}_{PV(Alb),0}$ is somewhat different. $I^{(bifacial)}_{PV(Alb),0}$ consists of both albedo due to direct normal irradiance and diffuse horizontal irradiance:

$$I^{(bifacial)}_{PV(Alb),0} = I^{(bifacial)}_{PV(Alb:dir),0} + I^{(bifacial)}_{PV(Alb:diff),0} \tag{C.2}$$

The diffuse component remains unchanged. However, the direct component calculation is simplified in that the direct light is not being absorbed or shaded by the panels throughout the day so the amount reaching the ground is always 100% of the direct insolation. The view factor, $F_{dz-Ugnd}$, is also unchanged throughout the day and is the same as for the diffuse component:

$$F_{dz-Ugnd} = \frac{1}{2}(1 - \sin\psi_g(z)) \tag{C.3}$$

Using these modifications to the model, we calculate the power output for the four locations in Table C.1 and use the parameters listed in Table C.2 to perform the calculations. The calculations based on a row period of 3.81 m are presented in section 4.4 to be consistent with the other PV systems in Table 4.3. However, consistent with the height to period (spacing) ratio used in Khan et al., we also modeled a row spacing of 2.5 m. As N-S facing vertical panels are immune to direct shading of one another, they could be made closer still. A more detailed cost analysis would be needed to determine the optimal row spacing.

Table C.2.
Parameters used in modeling the power output of N-S facing vertical bifacial farms

Panel height (h)	1.5 m
Row period (p)	3.81 m, 2.5 m
Diffuse efficiency (η_{diff})	15.67%
Albedo	0.2

The modeled power output for both E-W and N-S facing vertical bifacial PV aglectric farms is summarized in Table C.2. It is worth noting that in the N-S facing configuration, locations such as Miami with high diffuse insolation outperform locations such as Daggett, CA that have very high direct insolation, but limited diffuse insolation. Since regions with the high farmland intensity often have higher diffuse insolation, this is a favorable result for the feasibility of PV aglectric farming.

Table C.3.
Modeled power output for vertical bifacial PV aglectric farms

Location	Latitude	Longitude	E-W facing W/m^2	N-S facing W/m^2 Period (m) = 3.81 (2.5)
Seattle, WA	47.6038	−122.3301	4.1	4.9 (6.6))
West Lafayette, IN	40.4259	−86.9081	4.3	5.7 (7.6)
Miami, FL	25.7743	−80.1937	5.3	6.7 (9.0)
Daggett, CA	34.8634	−116.888	6.0	6.2 (8.3))

D. SHALE GAS PROCESSES MODELING DATA

The major stream composition is list in the following tables for the process simulation results. Feed refers to the raw shale gas feed; for NCP-1, IRA-1, SRA-2 processes, methane-rich stream refers to the overhead stream coming out of the demethanizer; for ENR designs, methane-rich stream refers to the gas phase stream coming out of the first-stage separation in the liquid product recovery unit (condenser for ENR-1 and absorption column for ENR-2/ENR-3); recycle stream refers to the recycle stream which mixed with the original inlet stream at the mixing point.

Table D.1.
Stream information for process NCP-1 simulated by Model I

	Feed	Methane-rich	Dehydro-in	Dehydro-out	Recycle	Product
Flowrate (kmol/h)	498.0	322.3	682.2	814.6	511.5	64.8
Mole frac (%)						
H_2	0	0	14.33	28.25	19.11	0
CH_4	57.55	85.27	20.80	17.42	25.43	0.01
C_2H_6	19.89	6.27	28.86	15.84	23.07	0.48
C_3H_8	11.30	0.40	12.14	3.63	5.44	1.35
C_4H_{10}	3.77	0.02	7.92	5.24	6.90	9.67
C_{5+} alkanes	1.27	0	1.56	1.31	0.84	9.58
C_2H_4	0	0	0.39	8.65	0.52	0
C_3H_6	0	0	7.11	12.49	9.48	1.77
C_{4+} olefins	0	0	6.91	7.18	9.21	77.13
N_2	5.20	8.03	0	0	0	0
CO_2	0.57	0	0	0	0	0
H_2S	0.29	0	0	0	0	0
H_2O	0.15	0	0	0	0	0

Table D.2.
Stream information for process NCP-1 simulated by Model II

	Feed	Methane-rich	Dehydro-in	Dehydro-out	Recycle	Product
Flowrate (kmol/h)	498.0	322.3	955.7	1157.9	785.0	59.8
Mole frac (%)						
H_2	0	0	15.36	24.74	18.70	0
CH_4	57.55	85.27	21.88	18.06	25.13	0.02
C_2H_6	19.89	6.27	37.08	25.27	35.10	1.03
C_3H_8	11.30	0.40	8.92	2.76	3.85	1.32
C_4H_{10}	3.77	0.02	2.11	0.15	0.18	0.42
C_{5+} alkanes	1.27	0	0.68	0.02	0.02	0.18
C_2H_4	0.00	0.00	0.38	15.76	0.47	0.01
C_3H_6	0.00	0.00	6.85	10.86	8.33	2.10
C_{4+} olefins	0.00	6.75	2.37	8.22	94.93	
N_2	5.20	8.03	0	0	0	0
CO_2	0.57	0	0	0	0	0
H_2S	0.29	0	0	0	0	0
H_2O	0.15	0	0	0	0	0

Table D.3.
Stream information for process IRA-1 simulated by Model I

	Feed	Methane-rich	Dehydro-in	Dehydro-out	Recycle	Product
Flowrate (kmol/h)	498.0	477.3	470.3	629.6	453.3	81.4
Mole frac (%)						
H_2	0	33.38	0.02	25.32	35.15	0
CH_4	57.55	60.05	6.87	5.13	7.11	0.01
C_2H_6	19.89	1.10	47.38	20.61	28.35	0.94
C_3H_8	11.30	0	16.42	3.55	4.60	1.66
C_4H_{10}	3.77	0	8.66	4.67	4.82	9.14
C_{5+} alkanes	1.27	0	1.78	1.33	0.45	7.80
C_2H_4	0	0.04	0.54	15.18	0.60	0.01
C_3H_6	0	0.01	10.38	16.47	10.72	2.87
C_{4+} olefins	0	0	7.95	7.74	8.21	77.58
N_2	5.20	5.42	0	0	0	0
CO_2	0.57	0	0	0	0	0
H_2S	0.29	0	0	0	0	0
H_2O	0.15	0	0	0	0	0

Table D.4.
Stream information for process IRA-1 simulated by Model II

	Feed	Methane-rich	Dehydro-in	Dehydro-out	Recycle	Product
Flowrate (kmol/h)	498.0	490.7	573.7	798.7	571.4	75.8
Mole frac (%)						
H_2	0	34.73	0.00	21.34	29.82	0
CH_4	57.55	58.42	6.07	4.36	6.09	0
C_2H_6	19.89	1.53	56.03	28.90	40.23	1.28
C_3H_8	11.30	0	13.58	2.84	3.79	1.36
C_4H_{10}	3.77	0	3.51	0.22	0.24	0.57
C_{5+} alkanes	1.27	0	1.12	0.03	0.01	0.18
C_2H_4	0	0.04	0.52	24.38	0.55	0.01
C_3H_6	0	0.01	10.20	15.13	10.25	2.73
C_{4+} olefins	0	0	8.97	2.80	9.01	93.87
N_2	5.20	5.28	0	0	0	0
CO_2	0.57	0	0	0	0	0
H_2S	0.29	0	0	0	0	0
H_2O	0.15	0	0	0	0	0

Table D.5.
Stream information for process SRA-2 simulated by Model I

	Feed	Methane-rich	Dehydro-in	Dehydro-out	Recycle	Product
Flowrate (kmol/h)	498.0	478.9	787.1	951.2	294.1	82.0
Mole frac (%)						
H_2	0	34.27	0	17.25	0	0
CH_4	57.55	59.84	39.75	32.89	8.92	0.05
C_2H_6	19.89	0.43	24.46	10.09	31.77	0.54
C_3H_8	11.30	0	9.38	1.94	5.97	1.04
C_4H_{10}	3.77	0	6.03	3.71	9.74	8.13
C_{5+} alkanes	1.27	0	1.23	1.02	1.14	7.74
C_2H_4	0	0.05	0.45	10.52	1.19	0.01
C_3H_6	0	0.01	8.35	12.73	22.34	2.91
C_{4+} olefins	0	0	7.07	7.12	18.92	79.58
N_2	5.20	5.40	3.29	2.72	0	0
CO_2	0.57	0	0	0	0	0
H_2S	0.29	0	0	0	0	0
H_2O	0.15	0	0	0	0	0

Table D.6.
Stream information for process SRA-2 simulated by Model II

	Feed	Methane-rich	Dehydro-in	Dehydro-out	Recycle	Product
Flowrate (kmol/h)	498.0	491.5	878.3	1118.9	385.3	77.0
Mole frac (%)						
H_2	0	35.51	0	15.60	0	0
CH_4	57.55	58.31	35.89	28.17	7.42	0.04
C_2H_6	19.89	0.85	32.67	17.23	48.77	0.92
C_3H_8	11.30	0	8.50	1.70	4.76	0.94
C_4H_{10}	3.77	0	2.25	0.11	0.25	0.31
C_{5+} alkanes	1.27	0	0.73	0.01	0.02	0.10
C_2H_4	0	0.06	0.46	19.87	1.04	0.01
C_3H_6	0	0.01	8.66	12.40	19.74	2.92
C_{4+} olefins	0	0	7.90	2.59	18.01	94.75
N_2	5.20	5.27	2.95	2.31	0	0
CO_2	0.57	0	0	0	0	0
H_2S	0.29	0	0	0	0	0
H_2O	0.15	0	0	0	0	0

Table D.7.
Stream information for process ENR-1 simulated by Model I

	Feed	Methane-rich	Dehydro-in	Dehydro-out	Recycle	Product
Flowrate (kmol/h)	498.0	549.3	494.9	605.0	1.9	15.2
Mole frac (%)						
H_2	0	20.04	0	18.20	0.72	0
CH_4	57.55	52.18	57.97	47.42	12.83	0.08
C_2H_6	19.89	9.03	20.07	8.25	13.22	0.54
C_3H_8	11.30	1.39	11.39	1.30	5.21	0.77
C_4H_{10}	3.77	1.13	3.82	1.12	6.69	2.82
C_{5+} alkanes	1.27	0.69	1.31	1.07	6.00	16.77
C_2H_4	0	0.35	0	8.16	0.35	0.01
C_3H_6	0	5.39	0.07	8.08	18.31	2.29
C_{4+} olefins	0	5.09	0.14	2.12	36.33	76.71
N_2	5.20	4.71	5.23	4.28	0.34	0
CO_2	0.57	0	0	0	0	0
H_2S	0.29	0	0	0	0	0
H_2O	0.15	0	0	0	0	0

Table D.8.
Stream information for process ENR-1 simulated by Model II

	Feed	Methane-rich	Dehydro-in	Dehydro-out	Recycle	Product
Flowrate (kmol/h)	498.0	557.4	494.4	623.6	1.4	12.0
Mole frac (%)						
H_2	0	18.74	0	16.76	0.71	0
CH_4	57.55	51.42	58.01	45.99	13.39	0.09
C_2H_6	19.89	12.11	20.09	10.88	18.60	0.75
C_3H_8	11.30	1.44	11.40	1.32	5.57	0.82
C_4H_{10}	3.77	0.04	3.80	0.04	0.26	0.13
C_{5+} alkanes	1.27	0.01	1.28	0.01	0.04	0.07
C_2H_4	0	0.35	0	11.69	0.38	0.01
C_3H_6	0	5.61	0.06	8.92	19.66	2.44
C_{4+} olefins	0	5.64	0.12	0.25	41.04	95.70
N_2	5.20	4.64	5.24	4.15	0.36	0
CO_2	0.57	0	0	0	0	0
H_2S	0.29	0	0	0	0	0
H_2O	0.15	0	0	0	0	0

Table D.9.
Stream information for process ENR-2 simulated by Model I

	Feed	Methane-rich	Dehydro-in	Dehydro-out	Recycle	Product
Flowrate (kmol/h)	498.0	484.5	781.4	948.8	288.4	62.0
Mole frac (%)						
H_2	0	34.54	0.90	18.38	2.44	0
CH_4	57.55	59.13	50.91	41.93	38.54	0.25
C_2H_6	19.89	0.26	16.63	3.42	10.72	0.43
C_3H_8	11.30	0.03	7.73	0.46	1.44	0.21
C_4H_{10}	3.77	0.26	8.36	5.43	16.12	6.05
C_{5+} alkanes	1.27	0.06	2.54	2.09	4.69	9.78
C_2H_4	0	0.02	0.12	10.38	0.33	0.01
C_3H_6	0	0.15	3.03	8.40	8.21	1.02
C_{4+} olefins	0	0.22	6.17	6.53	16.71	82.24
N_2	5.20	5.34	3.61	2.97	0.81	0
CO_2	0.57	0	0	0	0	0
H_2S	0.29	0	0	0	0	0
H_2O	0.15	0	0	0	0	0

Table D.10.
Stream information for process ENR-2 simulated by Model II

	Feed	Methane-rich	Dehydro-in	Dehydro-out	Recycle	Product
Flowrate (kmol/h)	498.0	494.4	731.6	953.7	238.6	58.4
Mole frac (%)						
H_2	0	35.73	0.88	19.20	2.70	0
CH_4	57.55	57.95	52.11	39.97	39.63	0.26
C_2H_6	19.89	0.59	21.50	6.47	24.40	0.97
C_3H_8	11.30	0.03	8.33	0.52	1.95	0.28
C_4H_{10}	3.77	0	2.59	0.02	0.06	0.03
C_{5+} alkanes	1.27	0	0.87	0	0	0.01
C_2H_4	0	0.02	0.12	18.81	0.38	0.01
C_3H_6	0	0.18	3.21	9.08	9.83	1.20
C_{4+} olefins	0	0.26	6.57	2.99	20.16	97.24
N_2	5.20	5.24	3.82	2.93	0.87	0
CO_2	0.57	0	0	0	0	0
H_2S	0.29	0	0	0	0	0
H_2O	0.15	0	0	0	0	0

Table D.11.
Stream information for process ENR-3 simulated by Model I

	Feed	Methane-rich	Dehydro-in	Dehydro-out	Recycle	Product
Flowrate (kmol/h)	498.0	483.1	1034.3	1197.2	541.3	60.3
Mole frac (%)						
H_2	0	33.71	0.77	14.27	1.48	0
CH_4	57.55	59.32	39.10	33.78	21.75	0.14
C_2H_6	19.89	0.85	25.57	14.23	30.56	1.23
C_3H_8	11.30	0.09	7.86	2.16	4.63	0.68
C_4H_{10}	3.77	0.30	11.06	8.45	17.66	6.89
C_{5+} alkanes	1.27	0.06	3.11	2.69	4.78	10.03
C_2H_4	0	0.02	0.12	7.97	0.23	0.01
C_3H_6	0	0.11	3.01	7.23	5.76	0.72
C_{4+} olefins	0	0.17	6.63	6.83	12.67	80.30
N_2	5.20	5.36	2.75	2.38	0.47	0
CO_2	0.57	0	0	0	0	0
H_2S	0.29	0	0	0	0	0
H_2O	0.15	0	0	0	0	0

Table D.12.
Stream information for process ENR-3 simulated by Model II

	Feed	Methane-rich	Dehydro-in	Dehydro-out	Recycle	Product
Flowrate (kmol/h)	498.0	493.0	1010.5	1220.8	517.5	54.2
Mole frac (%)						
H_2	0	33.41	0.68	14.06	1.33	0
CH_4	57.55	58.13	37.24	30.83	17.33	0.11
C_2H_6	19.89	2.71	37.68	24.26	54.42	2.16
C_3H_8	11.30	0.10	8.23	2.28	5.20	0.75
C_4H_{10}	3.77	0.01	2.22	0.32	0.70	0.33
C_{5+} alkanes	1.27	0	0.67	0.04	0.07	0.12
C_2H_4	0	0.06	0.11	13.81	0.21	0.01
C_3H_6	0	0.12	3.16	7.74	6.17	0.75
C_{4+} olefins	0	0.20	7.25	4.38	14.16	95.75
N_2	5.20	5.25	2.77	2.30	0.41	0
CO_2	0.57	0	0	0	0	0
H_2S	0.29	0	0	0	0	0
H_2O	0.15	0	0	0	0	0

E. MODELING APPROACH DETAILS FOR THE HYDROGEN PRODUCTION PROCESS VIA HIGH TEMPERATURE ELECTROLYSIS

Here we show the detailed information for the hydrogen production modeling in the integrated Aspen Plus/Matlab framework.

In Figure E.1, details about the H_2 production process model are shown. Input information, including solar collection temperature, SOEC operating temperature and pressure, SOEC operating mode and desired H_2 production rate, is provided to the Matlab core script by the user. The Matlab core script supplies the information

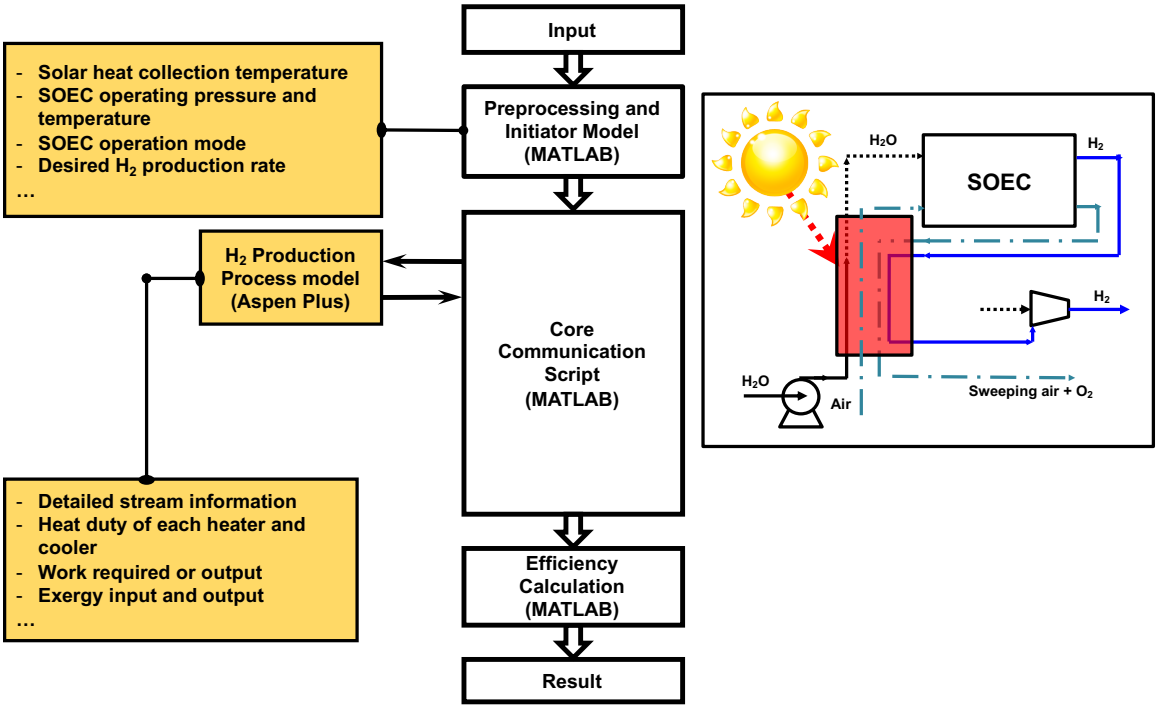

Fig. E.1. Details of the H_2 production process model, including all the input and output information

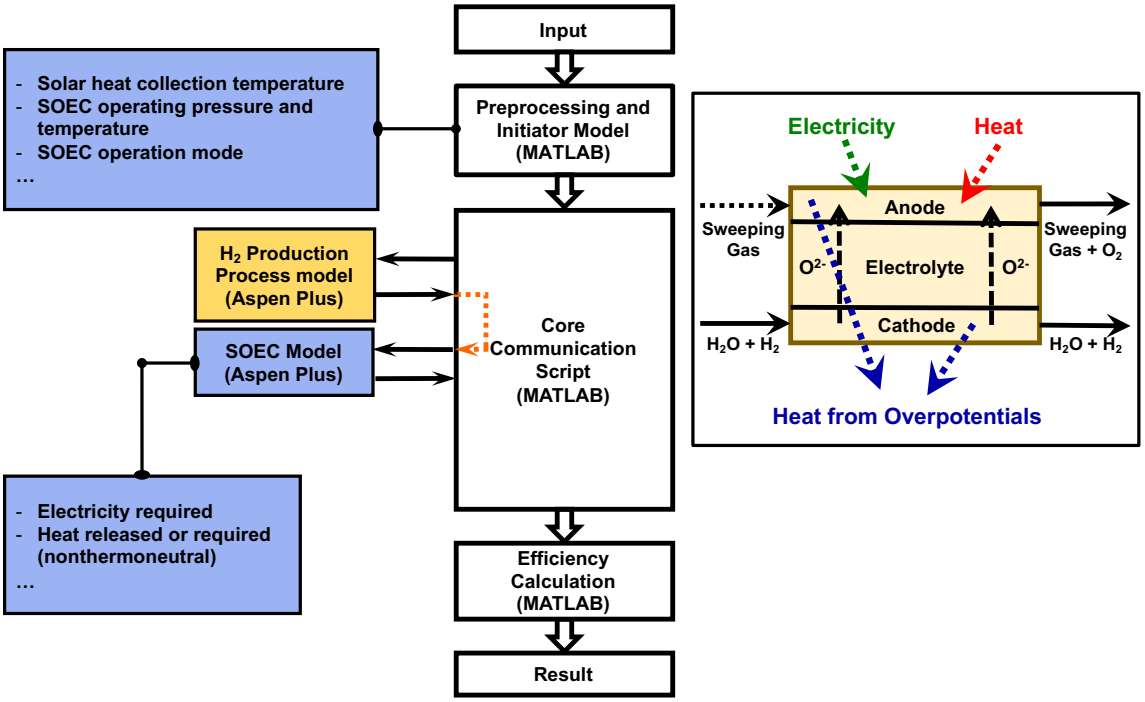

Fig. E.2. Details of the model for the SOEC module, including all the input and output information

to the H_2 production process built in Aspen Plus. The modeling results from Aspen Plus are extracted and exported to the Matlab core script.

In Figure E.2, details about the SOEC module are shown. Here, part of the input information, including solar collection temperature, SOEC operating temperature and pressure, SOEC operating mode is acquired from used input. Remaining input information for the SOEC model is acquired from the output of the H_2 production process model, such as the stream information of the gases entering the SOEC. After detailed SOEC modeling within a calculator block within Aspen Plus, the results are exported to the Matlab core script. The major information from the SOEC model is the electricity and heat requirement for the module.

In Figure E.3, details about the solar water power cycle are shown. Part of the input information for the cycle are from the Matlab core script defined by the

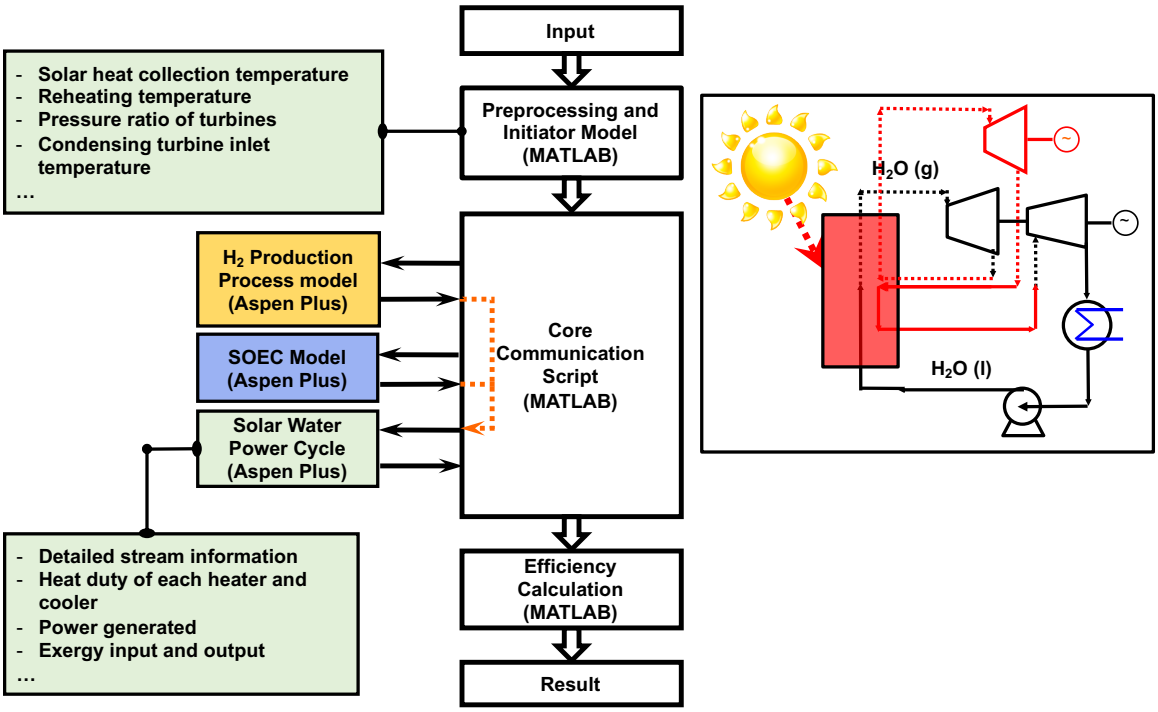

Fig. E.3. Details of the model for the solar water power cycle, including all the input and output information

user, such as the solar heat collecting temperature, the reheating temperature for the reheating stage within the cycle, the pressure ratio of the turbines, the inlet temperature of the condensing turbine, etc. The most important input information is from the modeling result of the SOEC model, the electricity requirement. The solar water power cycle should provide the electricity demand from the SOEC. The information is transferred via Matlab core script. The modeling results for the solar water power cycle are exported to the Matlab core script.

At the end, using the information collected from all three models discribed above, heat integration can be performed and various efficiencies can be calculated.

VITA

VITA

Yiru Li was born in Xi'an, China. Impacted by her grandparents who are both professors in civil engineering and her parents who both work for chemical engineering company, she was determined to be an engineer at very young age. After graduating from Xi'an Tieyi High School in 2011, she attended Tsinghua University in Beijing, China for her bachelor degree in Chemical Enigneering. In the summer of 2014, she participated summer research at University of Califonia, Davis. She was supervised by Prof. Fei Wei for her undergraduate thesis in catalytic conversion of methanol to aromatics.

After graduated from Tsinghua University in 2015, Yiru decided to join Purdue University to pursue her doctoral degree in chemical engineering. During her PhD study, she is supervised by Prof. Rakesh Agrawal, focusing on energy systems modeling towards a sustainable future. Her research topics include process design and intensification for shale gas conversion, systematic analysis of land constraint in a solar economy, and process design and integration for co-production of hydrogen and electricity from solar thermal energy.

Yiru has published several peer-reviewed articles or conference proceedings, including an article in Nature Sustainability. She presented her research at several conferences, including AIChE Annual Meetings, Symposium on Process System Engineering, Forum of Computer Aided Process Design and Natural Gas Conversion Symposium.

In August 2020, Yiru will join SINOPEC Engineering Incorporation in Beijing, China as a process research engineer after she graduates from Purdue University.

Yiru plays multiple musical instruments such as the piano, the flute and the classical guitar, and she enjoys playing volleyball and watching musicals after work.